Characterization of Oxide Thin Films and Interfaces

Using Transmission Electron Microscopy

by

Ajit Dhamdhere

A Dissertation Presented in Partial Fulfillment
of the Requirements for the Degree
Doctor of Philosophy

Approved November 2015 by the
Graduate Supervisory Committee:

David J. Smith, Chair
Martha R. McCartney
Ralph Chamberlin
Fernando Ponce

ARIZONA STATE UNIVERSITY

December 2015

ABSTRACT

Multifunctional oxide thin-films grown on silicon and several oxide substrates have been characterized using High Resolution (Scanning) Transmission Electron Microscopy (HRTEM), Energy-Dispersive X-ray Spectroscopy (EDX), and Electron Energy-Loss Spectroscopy (EELS). Oxide thin films grown on $SrTiO_3$/Si pseudo-substrate showed the presence of amorphised $SrTiO_3$ (STO) at the STO/Si interface. Oxide/oxide interfaces were observed to be atomically clean with very few defects.

Al-doped $SrTiO_3$ thin films grown on Si were of high crystalline quality. The Ti/O ratio estimated from EELS line scans revealed that substitution of Ti by Al created associated O vacancies. The strength of the crystal field in STO was measured using EELS, and decreased by ~1.0 eV as Ti^{4+} was substituted by Al^{3+}. The damping of O-K EELS peaks confirmed the rise in oxygen vacancies. For Co-substituted STO films grown on Si, the EDS and EELS spectra across samples showed Co doping was quite random. The substitution of Ti^{4+} with Co^{3+} or Co^{2+} created associated oxygen vacancies for charge balance. Presence of oxygen vacancies was also confirmed by shift of Ti-L EELS peaks towards lower energy by ~0.4 eV. The crystal-field strength decreased by ~0.6 eV as Ti^{4+} was partially substituted by Co^{3+} or Co^{2+}.

Spinel Co_3O_4 thin films grown on $MgAl_2O_4$ (110) were observed to have excellent crystalline quality. The structure of the $Co_3O_4/MgAl_2O_4$ interface was determined using HRTEM and image simulations. It was found that $MgAl_2O_4$ substrate is terminated with Al and oxygen. Stacking faults and associated strain fields in spinel Co_3O_4 were found along [111], [001], and [113] using Geometrical Phase Analysis.

NbO_2 films on STO (111) were observed to be tetragonal with lattice parameter of 13.8 Å and NbO films on LSAT (111) were observed to be cubic with lattice parameter of 4.26 Å. HRTEM showed formation of high quality NbO_x films and excellent coherent interface. HRTEM of $SrAl_4$ on LAO (001) confirmed an island growth mode. The $SrAl_4$ islands were highly crystalline with excellent epitaxial registry with LAO. By comparing HRTEM images with image simulations, the interface structure was determined to consist of Sr-terminated $SrAl_4$ (001) on AlO_2-terminated LAO (001).

This dissertation is dedicated to the memory of my beloved parents.

ACKNOWLEDGMENTS

I would like to express my profound gratitude to my advisor, Regents’ Professor David J. Smith, for his guidance, encouragement and constant support. Regent's Prof. Smith introduced me to the fascinating world of Electron Microscopy and also provided me a valuable second opportunity for education and research, for which I am indebted to him. His technical and editorial expertise and advice was essential for the completion of this dissertation research. I am also highly grateful to Professor Martha R. McCartney for her scientific and technical expert advice, support, and dynamic discussions. I would like to express my appreciation for Professor Ralph Chamberlin and Professor Fernando Ponce for serving on my dissertation committee.

I am grateful for the opportunity to use facilities in the John M. Cowley Center for High Resolution Electron Microscopy. I would like to thank staff, Dr. Toshihiro Aoki, Karl Weiss, Jason Ng and Sisouk Phrasavath for their valuable technical support and discussions during my research. My sincere thanks to the staff of Physics Department, especially Araceli Vizcarra, for her valuable academic advice and support. I appreciate Professor Alexander Demkov and his colleagues of the University of Texas, Austin for collaboration and for providing the samples used for investigation in this dissertation.

Many thanks to all the MDG members for great camaraderie over the years. In particular, I thank Dr. J. J. Kim and Dr. Lin Zhou for TEM sample prep hands-on help and useful technical discussions. Finally, I would like to express my heartfelt appreciation to my wife, Meghana for her love and solid support. Her constant encouragement and selfless courage helped me overcome personal losses these last few years and complete this Ph.D. dissertation.

TABLE OF CONTENTS

Page

LIST OF FIGURES....................viii

CHAPTER

1 INTRODUCTION TO FUNCTIONAL OXIDE THIN FILMS....................1

1.1 Oxides and Oxide Thin Films....................1

1.2 Thin Film Deposition....................8

1.2.1 Molecular Beam Epitaxy....................8

1.2.2 Atomic Layer Deposition....................12

1.2.3 Orientation Control and Substrates....................14

1.3 Integration of Oxides....................15

1.4 Epitaxial Strain Engineering and Modulation Doping....................17

1.5 Oxide Superlattices....................19

1.6 Overview of Dissertation....................23

References....................25

2 EXPERIMENTAL TECHNIQUES....................29

2.1 Transmission Electron Microscopy....................29

2.2 High Resolution Transmission Electron Microscopy....................31

2.3 HRTEM Image Simulation....................36

2.4 Geometric Phase Analysis....................41

2.5 Scanning Transmission Electron Microscopy....................44

2.6 TEM Sample Preparation....................48

CHAPTER Page

2.6.1 Conventional Mechanical Method of Sample Preparation..............49

2.6.2 Focused Ion Beam Sample preparation..50

References..51

3 EPITAXIAL THIN FILMS OF DOPED-$SrTiO_3$ ON Si.....................................53

3.1 Introduction...53

3.2 Al-Doped $SrTiO_3$ for Oxide Electronics..56

3.2.1 Experimental Work...57

3.2.2 Determining Electronic Structure.. 64

3.3 Ferromagnetic Cobalt-substituted $SrTiO_3$ Thin-film................................75

3.3.1 Experimental Work...78

3.3.2 Determining Electronic Structure...84

3.4 Conclusions...89

References..91

4 Co_3O_4/$MgAl_2O_4$ (110) SPINEL HETEROSTRUCTURES.................................93

4.1 Introduction...93

4.2 Experimental Work..96

4.3 Determining Interface Structure...99

4.4 Defects in Co_3O_4/$MgAl_2O_4$..104

4.5 Conclusions...114

References..115

CHAPTER Page

5 HETEROEPITAXY ON OXIDE SUBSTRATES....117

5.1 Niobium Oxide Thin-Films on STO (111) and LSAT (111)....117

5.1.1 Introduction....117

5.1.2 Experimental Work....120

5.1.3 Determining Crystal Structure of NbO_2/STO (111)....121

5.1.4 Determining Crystal Structure of NbO/LSAT (111)....126

5.2 Intermetallic Zintl Aluminide Thin-Films on LAO (100)....131

5.2.1 Introduction....131

5.2.2 Experimental Work....133

5.2.3 Interface Structure Determination....136

5.3 Conclusions....140

References....142

6 CONCLUSIONS AND FUTURE WORK....144

6.1 Summary....144

6.2 Remarks on future work....149

COMPREHENSIVE LIST OF REFERENCES....152

LIST OF FIGURES

Figure Page

1.1 The Perovskite Prototype Structure..6

1.2 Ruddlesden–Popper Phases, $A_{n+1}B_nO_{3n+1}$, where A and B are Cations, and O an Oxygen Anion. The n = 1, 2 and 3 Members of the Series are Shown...........7

1.3 Typical MBE System..9

1.4 Schematic of ALD..13

1.5 HRTEM Images of GaAs/AlAs and $BaTiO_3/SrTiO_3$ Heterostructures.................20

1.6 Ө-2Ө XRD Scans of $(BaTiO_3)n/(SrTiO_3)m$ Superlattices for (a) m=4 and n=1-6, 8 and (b) m=13 and n=1-3. Substrate Peaks are Marked by Star...............21

2.1 Comparison of PCTF Curves for a 400 keV HREM, Axial Illumination, C_S= 1.0 mm. (a) Coherent Illumination, No Damping Functions; (b) Effect of Damping Functions for a Focal Spread of 8 nm and an Incident Illumination Semi-angle of 0.5 mrad. Arrow Indicates the Interpretable Resolution Limit......34

2.2 Al_2O_3/Nb Interface. HRTEM Images at Defocus Value Δf = 40 nm and (b) Δf = 50 nm. The Insets Represent Simulated Images for the Interface Model...40

2.3 Left Top is HRTEM of Interface Region between $Si_{0.7}Ge_{0.3}$ and Si Substrate in [1-1 0] Orientation. Right Top Show GPA Analysis with Fourier Transform of the HRTEM Image and Spots Analyzed 111 and 11-1 Circled and Geometric Phase of (111) Lattice Fringes and Geometric Phase of (11-1) Lattice Fringes. Bottom Image Shows Deformation Map of Interface Region:

Figure Page

with Deformation Perpendicular to Interface Plane, e_{yy}, with Respect to Si Lattice the Line Profile Averaged Along 20 nm of Interface. The Average Deformation in SiGe Layer is Calculated to be $1.7 \pm 0.1\%$ 43

2.4 Schematic Construction of a STEM..45

3.1 HRTEM Image Showing Cross-section of Al-doped STO Thin Film Grown on Silicon. Insets are Diffractograms from Film and Substrate.................................58

3.2 HRTEM Image Showing Cross-section of Al-doped STO Thin Film Grown on Silicon. Insets are Diffractograms from Film and Substrate.................................59

3.3 Cross-sectional HAADF Image of Al-doped STO Grown on Silicon, Enlarged View and Atomic Model of STO in (001) Projection............................60

3.4 Cross-sectional HAADF Image of Al-doped STO Grown on Silicon, Enlarged View and Atomic Model of STO in (001) Projection...60

3.5 Elemental Distribution Across Al-doped STO Sample..62

3.6 Al Distribution Across the Al-doped STO Sample Taken from Figure 3.5..........62

3.7 Ti and O Distribution in Al-doped STO Thin Film...63

3.8 Relative Composition Ratio of Ti/O..63

3.9 EELS and EDS Line-scan Geometry...65

3.10 EELS Spectra of Al-doped STO. The Ti-L and O-K Fine Edge Structure Change Moving Across the Sample Starting with Series 6 at the Si-STO Interface..66

Figure Page

3.11 Ti-L and O-K Fine Edge Structure Evolve on Moving from Amorphous SiOx + SrOx +TiOx Phases at the Interface (series 11) into Al-doped STO (Series 15)......66

3.12 Ti-L and O-K Fine Edge Structure in 10% Al-doped STO (From Series 16 to Series 20)......66

3.13 Ti-L and O-K Fine Edge Structure in 20% Al-doped STO (Series 21 through Series 25)......67

3.14 Ti-L and O-K Fine Edge Structure Evolve From 20% Al-doped STO Moving into 10% Al-doped STO +SrO (Series 26-30). The O-K Fine Edge Structure Starts Damping Out as % of O Vacancies Rises......67

3.15 Ti-L and O-K Fine Edge Structure Evolving into10% Al-doped STO +SrO (Series 31-35). Large Number of Oxygen Vacancies is Apparent as the O-K Fine Structure Damps-out Completely and Ti-L Fine Structure Disappears......67

3.16 EELS for Oxygen-deficient $SrTiO_{3-d}$, for d ~ 0, 0.13 and 0.25. a, the O-K Edge Fine Structure is Sensitive to O–O Ordering, and Damps-out with Increasing Vacancy Concentration b, the Ti-L Edge Shifts from 4þ to 3þ Valence with Increasing Oxygen Vacancies......69

3.17 Experimental Fine-edge Structure Details of Ti-L and O-K in STO......70

3.18 Ti-L Near-edge Spectra for Series 10 - Series 36......72

3.19 Ti-L ELNES from ~10 % Al-doped STO area (Series 13-Series 18) Compared with Spectra from ~20 % Al-doped STO Region (Series 22 - Series 27)......73

Figure Page

3.20 O-K Near-edge Spectra for Series 10 - Series 36...74

3.21 O-K ELNES from ~10 % Al-doped STO Region (Series 13-Series 18) Compared with Spectra from ~20 % Al-doped STO Region (Series 22 - Series 27)..75

3.22 HRTEM Image of Cross-section of 30% Co-doped STO Thin Film on Si (001). Amorphized STO, SiOx and SrOx Phases at Interface. Insets are Diffractograms from Film and Substrate...79

3.23 HRTEM Image of Cross-section of 25% Co-doped STO Thin Film on Si (001). Amorphous SiOx and SrOx at Interface. Insets are Diffractograms from Film and Substrate..80

3.24 Cross-sectional HAADF Image of 25% Co-doped STO Grown on Silicon, Magnified View and Atomic Model of STO in (001) Projection.........................80

3.25 Elemental Distribution across 25% Co-doped STO Sample................................82

3.26 EDS Line-scan Geometry Corresponding to Figure 3.25.....................................82

3.27 Ti and O Areal Distribution in 25% Co-doped STO Lattice................................83

3.28 Relative Composition of Ti and O Distribution in 25% Co-doped STO...............84

3.29 EELS Line-scan Geometry..84

3.30 ELNES of Ti-L Fine Edge Averaged Over 40 Spectra Recorded Along Line-scan of Length ~4 nm (Blue). A Trend Line is Added (Black)....................86

3.31 ELNES of O-K Fine Edge Averaged Over 40 Spectra Recorded Along Line-scan of Length ~4 nm (Blue). A Trend Line is Added (Black)....................86

Figure Page

4.1 $MgAl_2O_4$ Structure Consisting of Distorted Face-centered-cubic Array of Oxygen Anions (Red Spheres), With Mg^{2+} Cations Occupying 1/8 of the Tetrahedral Interstices (Yellow Tetrahedron) and the Al^{3+} Cations Occupying Half of the Octahedral Interstices (Blue Octahedra)...........................94

4.2 At Room Temperature, Co_3O_4 Assumes the Normal Spinel Structure. Based on the Crystal Field Splitting, the Co^{2+} ions (Tetrahedral, Light Blue) Carry Magnetic Moment, while the Co^{3+} (Octahedral, Dark Blue) Ions are Nonmagnetic...95

4.3 HRTEM micrographs. (a) Region of original cross-section micrograph of Co_3O_4/$MgAl_2O_4$ (110) heterostructure viewed in [011] projections. (b), (c) are enlarged interface images...98

4.4 (a) Model A with Mg (orange), Al (light blue) and O (red) in the Top Layer of $MgAl_2O_4$ Shown by the Arrow. (b) Calculated Projected Potential Based on Model Shown in (a)..100

4.5 (a) Model B with Al (light blue) and O (red) in the Top Layer of $MgAl_2O_4$ Shown by the Arrow. (b) Calculated Projected Potential Based on Model B.....100

4.6 Experimental and Simulated Images for Interface Model A. Line Profiles Across Interface of Experimental and Simulated Images. The Arrows in 4.6aa and 4.6bb Represents Intensity Profile along the Profile Line 102

4.7 Experimental and Simulated Images for Interface Model B. Line Profiles Across Interface of Experimental and Simulated Images. The Arrows in 4.7aa and 4.7bb Represents Intensity Profile along the Profile Line..................102

Figure Page

4.8 Contrast Transfer Function of JEOL-4000EX at Optimal Defocus of 49.7 nm. For {110} Projected Spinel, <111>, <022>, <113> and <004> Reflections are Allowed by CTF. <002> Reflection is Absent as Predicted by Neutron Diffraction....................106

4.9 Contrast Transfer Function of JEOL-4000EX at Optimal Defocus of 49.7 nm. For {001} Projected Spinel, <022> and <004> Reflections are Allowed by CTF....................106

4.10 (b) Cross-section Image in <110> Projection Used for Defect Analysis with GPA and Fourier Filtering. (a) and (c) Diffractogram and Simulated Diffraction Pattern....................106

4.11 (b) Strain Map in X-Y Direction Using GPA. (a) and (c) Corresponding Fourier-filtered Image Using {111} Bragg Spots. Arrows Indicate Interface.....106

4.12 (a) and (b) Strain Map in X Direction (plane of the film) Using GPA and Corresponding Fourier-filtered Image Using (002) Bragg. (c) and (d) Strain Map inY Direction (Growth Direction) Using GPA and Corresponding Fourier-Filtered Image Using (022) Bragg Spot. Arrows Indicate Interface....................107

4.13 (b) Strain Map in 113 Direction Using GPA. (a) and (c) Corresponding Fourier-filtered Image Using {113} Bragg Spots. Arrows Indicate Interface.....107

4.14 (b) is the Cross-section in (001) Projection Used for Defect Analysis Using GPA and Fourier Filtering. (a) and (c) are Diffractogram and Simulated Diffraction Pattern....................108

Figure Page

4.15 (a) and (b) Strain Map in x Direction (Plane of Film) Using GPA and Corresponding Fourier-filtered Image Using {022} Bragg Spot. (c) and (d) Strain Map in the Y Direction (Growth Direction) Using GPA and Corresponding Fourier- filter Image Using {022} Bragg Spot. Arrows Indicate Interface....108

4.16 (b) Strain Map in X-Y Direction Using GPA. (a) and (b) Corresponding Fourier-filtered Image Using {004} Bragg Spots. Arrows Indicate Interface.....109

4.17 Magnetization of a Co_3O_4 (110) Film Measured as a Function of Temperature Under Zero-field-cooled Conditions (Blue Circles) with Constant In-plane Magnetic Field of 1 T. Field-cooled Data Show Similar Characteristics. The Onset of Antiferromagnetism is Labeled at 49 K. Inset Image Shows Antiferromagnetic Ordering in the Spinel Structure. The Overall Negative Magnetization is Because of the Diamagnetic Contribution from the Substrate....111

5.1 (a) NbO_2 Tetragonal Rutile Structure at High Temperatures and (b) BCT Tetragonal Distorted Rutile Structure with Neighboring Nb Atoms Forming Dimers Along the C-axis. Both Crystal Structures are in [001] Projection.........119

5.2 (a) is a HRTEM Micrograph of NbO_2/STO (b) is a Cross-section of Sample (c) is a Diffractogram of HRTEM Image in (b); (d) is a Simulated Diffraction Pattern of Substrate STO in <110>, (e) is Diffractogram in (d) with STO Mask Applied....122

Figure Page

5.3 Diffractogram from Film after Subtracting Diffraction Pattern of Substrate Matches Exactly with Simulated Diffraction Pattern of BCT NbO_2 [001].........123

5.4 Experimental Image of NbO_2-STO Interface Placed Next to Simulated Images of NbO_2 [001] and STO <110> Projected Crystals Models. Atom Columns are shown in Simulated Image..125

5.5 NbO_2 [001]-STO <110> Interface Proposed Model...125

5.6 (a) is a HRTEM Micrograph of NbO_x/LSAT System (b) is a Cross-section of Sample (c) is a Diffractogram of HRTEM Image in (b), (d) is a Simulated Diffraction Pattern of Substrate LSAT in <110>, (e) is Diffractogram in (d) with STO Mask Applied...127

5.7 Diffractogram from Film after Subtracting Diffraction Pattern of LSAT Substrate Matches Exactly with Simulated Diffraction Pattern of Cubic NbO <110> 128

5.8 Experimental Image of NbO-LSAT Interface (a) Placed Next to Simulated Images (b) of NbO <110> and LSAT <110> Projected Crystals Models...........129

5.9 Based on Image Simulations the Interface Model for NbO/LSAT System we Propose is Shown...130

5.10 Show Adjacent Grains with Different Orientations as Shown in Diffractograms from Two Regions of NbO Thin Film.......................................131

5.11 A Unit Cell of $SrAl_4$ with Sr (Green) and Al (Blue)...132

Figure Page

5.12 Cross-sectional HRTEM Micrograph of $SrAl_4$/LAO. Diffractograms Revealed Projections of Thin Film and Substrate. 3-D Island Growth is Clearly Visible....................134

5.13 Cross-sectional HRTEM Micrograph of $SrAl_4$/LAO. Diffractograms Revealed Projections of Thin Film and Substrate....................135

5.14 Interface Model 1 of Sr Terminated $SrAl_4$ (001) on AlO_2 Terminated LAO (001) & Model 2 of Al Terminated SrAl4 (001) on AlO_2 Terminated LAO (001)....................137

5.15 Simulated Images of Interface Model 1 and Interface Model 2 with Atom Columns Compared with a Cross-section of Experimental Image. The Color Code for Atom Columns: Red: O, Dark Blue: Sr, Yellow: Al Green: La...........139

5.16 Experimental HRTEM Cross-section Embedded With Interface Model 1.........141

CHAPTER 1

INTRODUCTION TO FUNCTIONAL OXIDE THIN-FILMS

1.1 Oxides and Oxide Thin-Films

Oxides exhibit a broad range of electronic, optical, and magnetic properties such as insulating, semiconducting, metallic, superconducting, ferroelectric, pyroelectric, piezoelectric, ferromagnetic, and multiferroic [1-10]. The extensive variety of these physical properties of oxides holds terrific promise for future electronics applications [1-3]. Similar to contemporary semiconductor device structures, many devices utilizing oxides will likely use multilayer of thin films with dimensions on the nanometer scale, sufficiently small to observe quantum effects. The physics of oxides confined to quantum-size dimensions is not well established. Precisely controlled preparation of high crystalline thin films with sharp interfaces is essential for an understanding of the effects of quantum confinement on the physical properties of these structures [3-5].

Further interesting are the new functionalities that might emerge at oxide interfaces. For example, the interfaces between suitable antiferromagnetic oxide materials have been observed to be ferromagnetic [11-15]. Similarly, charge transfer at the interface between proper nonmagnetic insulators can give rise to a superconducting electron gas at the interface [16-18]. The activation of improper phase transitions has been observed in thin films of oxides. These examples display the new enhanced functionalities that can be achieved by the nanoengineering of oxide heterostructures with atomic layer precision [11-18]. In addition, thin films provide suitable design for electric-

field-tunable electronic, magnetic, and structural phase transitions and phenomena. Oxide thin films are also highly suitable for integrated electronics [5].

The fantastic properties displayed by the functional metal oxides are mainly due to two reasons: high electronic polarizability, originating in the mixed ionic-covalent nature of the metal-oxygen bonds, and strong electron correlations, which originate from the localized and interacting transition-metal *d* and *f* electrons. As a result of this combination, the average energy of various interactions such as Coulomb repulsion and Hund's exchange are of similar magnitude [2]. While in conventional semiconductors or metals, one of these energy scales usually dominates, determines the ground state and the macroscopic properties, the interactions compete in transition metal oxides, leading to strong lattice–electron, electron–spin, and spin–orbit coupling. The ground state resulting from the interactions has multiple low-energy competing phases, and these phases are susceptible to small external perturbations [2]. Oxides in thin-film form offer additional control parameters to obtain delicate balance among the interactions to produce unique collective phenomena [2].

In spite of the great progress that has been made recently in achieving coherent, high quality, oxide thin films and heterostructures, it is very difficult to predict the electrical, magnetic, or optical properties at oxide heterointerfaces given the known properties of the bulk constituents. This complication is due to a limited knowledge of the structure of oxide thin films; in particular, oxygen positions are highly non-trivial to determine using standard diffraction techniques. In addition, the closely competing energies that lead to the desired novel functionalities in turn cause the properties to be

strongly dependent on small modifications in atomic structure and are therefore hard to predict [2]. Oxide thin films have the potential to revolutionize the electronics industry, for example, through next generation Mott devices, or efficient alternatives for our growing energy needs, however, their adoption in practical devices has been slow. This situation is unlikely to change until a detailed microscopic understanding of the atomic and electronic structures in oxide thin films is well developed [6-7].

The structural distortions adopted by perovskite oxides have a profound influence on its electronic properties. The ideal ABO_3 perovskite structure is simple cubic, with space group Pm-3m, and consists of octahedrally coordinated B-site cations (usually transition metals) with three- dimensional, corner-connected BO_6 oxygen octahedra resulting in …O–B–O… chains with 180° B–O–B bond angles. Larger cations occupy the high symmetry positions of the octahedral vacancies between the octahedra (the A sites) [2]. However, only a few ABO_3 oxides adopt this ideal structure and, in practice, most perovskites exhibit various structural distortions that lower the symmetry of the system from that of the cubic prototype.

The most widely occurring deformations are rotations or “tilts” of essentially rigid oxygen octahedra around one or more high symmetry axis. The octahedral units approximately maintain their regularity and strictly keep their corner connectivity. Since the octahedra are connected in three dimensions, a rotation or tilt in one direction restricts the allowed tilts and rotations in other directions. Besides these octahedral rotations, which are determined by geometric and electrostatic factors, electronically-driven distortions, particularly those caused by the first and second-order Jahn-Teller effects, are

important in determining the perovskite structure. First-order Jahn-Teller distortions occur when an electronic degeneracy usually associated with the *d*-electrons on the B-site cation is removed by an appropriate structural distortion [4-5]. This typically manifests as an elongation of some B–O bonds and a shortening of others. Relative displacements of ions that result in polar ferroelectric distortions further lower the crystal symmetry. These distortions are known as second-order Jahn-Teller effects [2, 9-10].

One of the major routes to engineering the properties of a perovskite oxide in a thin film is to control the elastic strain energy imposed by the substrate. Proper choice of the mismatch between the lattice parameters of the substrate and the film, as well as their relative orientations, can be used to enforce a specific amount of strain on the film by the substrate. The strain acts by imposing a new in-plane lattice constant on the film. One possible way is the change in the in-plane lattice parameter is accommodated entirely by a change in the in-plane metal-oxygen bond lengths. In another scenario, the lattice mismatch can be accommodated by a change in magnitude or type of the tilt patterns through rigid rotations of the oxygen octahedra, and the B–O distances remain unchanged. These two responses have significantly different effects on the functionalities of the film. For example, changes in the B–O bond length affect the magnitude and symmetry of the crystal field splitting, whereas changes in B–O–B bond angles determine the strength and the sign of magnetic superexchange interactions. Oxygen positions are difficult to determine experimentally which yield only the cation positions. Hence it is difficult to distinguish between the two strain-responses from experiments [2, 9-10]. One additional possible response to the new substrate-enforced lattice parameters is that the

film changes its equilibrium stoichiometry or defect concentration. Oxygen vacancies are a particularly common point defect in perovskite oxides [9]. Application of different strains requires growth on different substrates, with different growth parameters. Hence it becomes difficult to establish experimentally whether changes in defect concentrations are an intrinsic thermodynamic response to strain, or arise from extrinsic factors during growth. In addition to the change in the in-plane lattice parameter, the details of the interfacial chemistry and structure are also likely to influence the film properties. Possible effects include propagation of a tilt pattern associated with the substrate into the film, chemical bonding across the interface and interfacial electrostatics [2, 9-10].

The perovskite ABO_3 structure, as shown in figure 1.1 [9], is highly open and can accommodate some 30 elements on the A site with 100% substitution and over half the periodic table on the B site. Since good chemical and structural compatibility between many perovskites is obvious, combination of perovskites offers an opportunity to customize electronic, magnetic, and optical properties in thin films heterostructures in ways that are not possible with conventional semiconductors. Integration of epitaxial stacks of different oxide crystals is possible because of the similarity in crystal structure, the chemical compatibility that exists between many oxides, and the directional dependence of properties that can be optimized for particular applications by controlling the orientation of the single crystalline film [9].

The properties of a structurally related family of oxides changes drastically from one end to the other end of the series. For examples the $Sr_{n+1}Ru_nO_{3n+1}$ Ruddlesden–Popper homologous series, as shown in figure 1.2. In this series, the positive integer n

corresponds to the number of perovskite layers that are sandwiched between double SrO rock-salt layers. For n=1 (Sr_2RuO_4) is paramagnetic and superconducting at very low temperature (1.5 K), while the ($SrRuO_3$) is ferromagnetic when n is infinite. This drastic change in properties within series is because of the structural changes from corner-sharing RuO_6 octahedral network that is connected in all three dimensions for the infinite member ($SrRuO_3$) to the n=1 member (Sr_2RuO_4), where the RuO_6 octahedra are only connected in two dimensions and double SrO layers completely disrupt all corner-sharing of the RuO_6 octahedra along the *c*-axis [19-21].

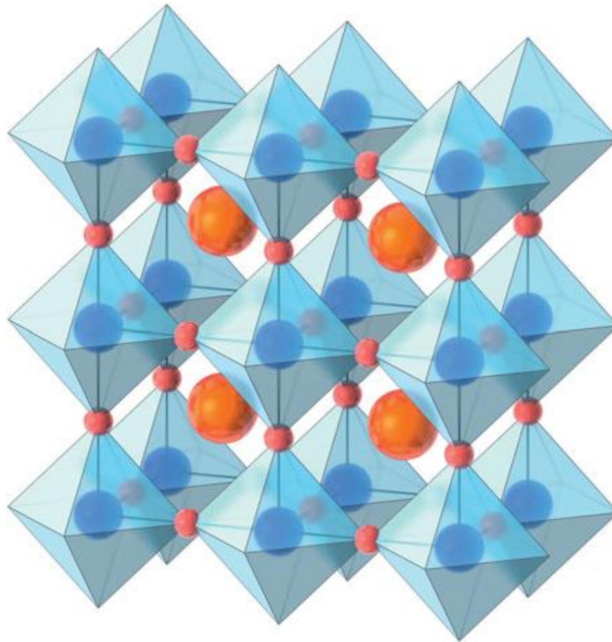

Figure 1.1: Perovskite Prototype Structure [9]

Many other fascinating perovskite oxide series exist showing interesting variation in ferromagnetic, ferroelectric, superconducting, and metal–insulator transition behavior [20]. Bulk synthesis methods are often inadequate to study in detail the changes in a property that occur as n is varied is a series. It is very difficult to produce growth

conditions of temperature and pressure that can yield single phase products for various n values. Attempts to create series with variable n often result in uncontrolled intergrowths that are a result of smaller differences in formation energy as n varies. Single-phase epitaxial films with variable n values can be synthesized using the thin-film techniques. This growth is possible because of the ability to supply reactant species in any desired sequence with atomic-level composition control, even though nearby phases have similar formation energies [20-21].

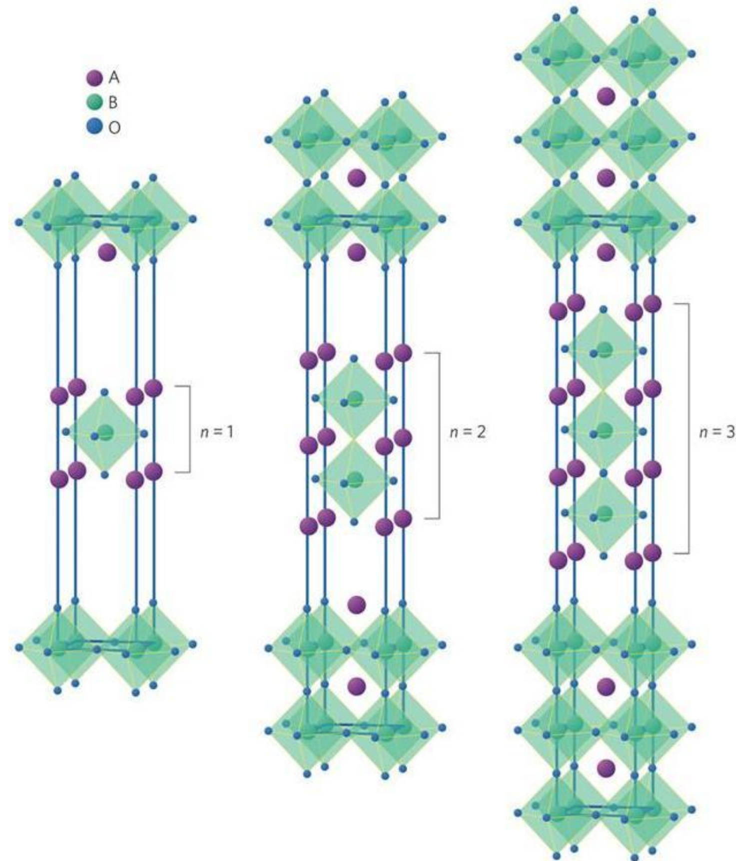

Figure 1.2: Ruddlesden–Popper phases, $A_{n+1}B_nO_{3n+1}$, where A and B are cations, and O an oxygen anion. The n = 1, 2 and 3 members of the series are shown [20].

1.2 Thin Film Deposition

Considerable advances in deposition technologies over the past few decades have enabled the growth of oxide thin films with high structural perfection, sharp interfaces and the ability to customize oxide layering down to the atomic layer level [22]. These advances were stimulated by the discovery of high-temperature superconductivity over 30 years ago [23]. Existing physical-vapor thin-film deposition techniques of semiconductors were rapidly modified to the challenges of functional oxides, including pulsed laser deposition (PLD) [24-25], molecular beam epitaxy (MBE) [22, 26], sputtering and co-evaporation [23]. Chemical techniques including metal-organic chemical vapor deposition (MOCVD) [27-28] and atomic layer deposition (ALD) [29-30] have also been adapted and applied to functional oxides. In this dissertation research, oxide thin films deposited using MBE and ALD were studied using Transmission Electron Microscopy. Hence, we will focus here only on MBE and ALD techniques.

1.2.1 Molecular Beam Epitaxy

The Molecular Beam Epitaxy (MBE) method of thin-film growth in which a thin film is grown layer-by-layer is shown in figure 1.3. The flux of each atomic or molecular beam (vapor pressure) is controlled by the temperature of the effusion cell of each species. The duration for each beam is individually controlled by shutters, which also control the growth sequence. Thus by controlling the shutters (dosage) and the temperature of the effusion cell (flux), the layering sequence of the desired heterostructure can be achieved. MBE is capable of controlling the layering of oxides on the unit-cell level. A low growth temperature is used to kinetically minimize subsequent

bulk reordering and to minimize the loss of the customized metastable layered structures. The huge difference between surface and bulk diffusion rates in oxides allows the growth of films with excellent structural order while at the same time preserving the potentially metastable phases. A clean UHV deposition environment, *in situ* characterization during growth, and the absence of highly energetic species, are some of the distinguishing characteristics of MBE. These capabilities are important to the precise control of oxide heterostructures at the atomic-layer level [22, 26].

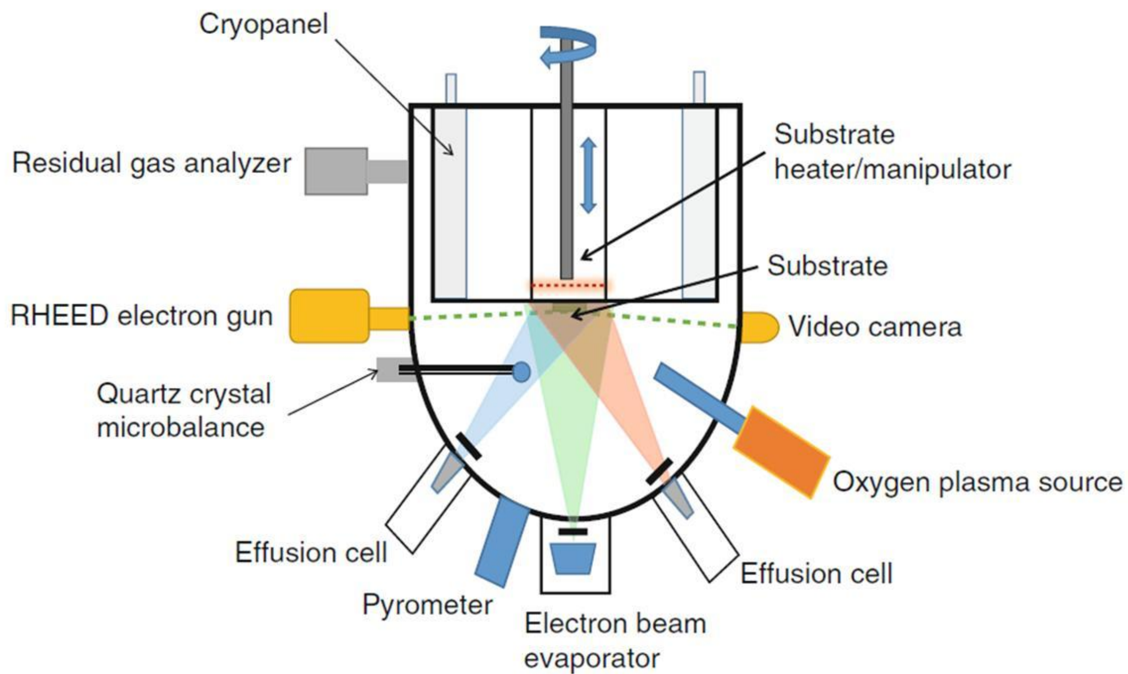

Figure 1.3: Typical MBE system [22]

The major differences between MBE systems of oxides and semiconductors are the presence of an oxidant species, more stringent composition control, and adequate pumping to handle the additional oxidant gas pressure. In a typical MBE growth, molecular beams of the constituent elements of the functional oxide are aimed at a single-

crystal substrate that is located at the center of an MBE chamber and is heated to the desired temperature. Each molecular beam is created by a separate effusion cell (or an electron-gun), each at a different temperature to provide the desired flux of the particular element. Elemental sources are used because multicomponent mixtures (especially oxides) rarely have same vapor pressure. In addition, each elemental source can be controlled independently to obtain desired growth sequence. The computer controlled shutters, which are stationed at the output end of each effusion cell, enables the elemental fluxes to be supplied to the substrate either at the same time (co-deposition) or separately (sequential deposition). In MBE, since molecular beams have long mean mean-free-paths, the shutters are only needed to block the line-of-sight transfer of atoms or molecules from the source to the substrate. The chamber walls are usually kept at low temperatures to hinder any possible off-gassing from wall [22, 23, 26].

In order to oxidize the elemental species reaching the substrate, a molecular beam of oxidant is normally used at proper pressure not to destroy the long mean-free-path necessary for MBE. The maximum pressure depends on the MBE geometry, the element to be oxidized, and the oxidant species used, but oxidant pressures less than about 10^{-4} Torr are typically required for MBE. On some occasions oxidants with higher activity or plasma sources are needed for the growth of oxides containing species that are more difficult to oxidize. The atomic-level precision controlled growth of multicomponent functional oxides is crucially dependent on accurate composition control [23]. The use of atomic absorption spectroscopy (AAS) for oxide MBE composition control has allowed fluxes to be measured with accuracies of better than 1% [23]. A retractable quartz crystal

microbalance provides absolute *in situ* flux measurements for calibration. The depositing fluxes of all sources can be simultaneously monitored during growth by AAS. The AAS signal is fed into the MBE computer control system, which then closes the appropriate shutters after the desired dose has been delivered to the substrate [22-23].

Modern oxide MBE systems contain additional features such as *in situ* reflection high-energy electron diffraction (RHEED), mass spectrometry, scanning tunneling microscopy, load-locked wafer introduction, real-time spectroscopic ellipsometry, and substrate temperature measurement systems that utilize the temperature dependence of the bandgap of oxide substrates, time-of-flight ion scattering and recoil spectroscopy, and even low-energy electron microscopy. The sensitivity of RHEED to surface structure is ideal for monitoring *in situ* the evolution of the growing surface, from initial nucleation to the deposition of each subsequent layer. The formation of intermediate reaction products or impurity phases can be readily monitored and the growth conditions adjusted during growth accordingly [22-23, 26].

The PLD technique is better suited than MBE to the synthesis of heterostructures made up of phases, each of which can be produced by bulk techniques in single-phase form. In the PLD process, a sample prepared in bulk form with exact stoichiometry becomes a target that is bombarded with a high-power laser under vacuum conditions to form thin films with the same exact stoichiometry as the ablated target [22, 24-25].

1.2.2 Atomic Layer Deposition

Atomic layer deposition (ALD, which is a variant of the chemical vapor deposition process, involves alternating self-limited surface reactions of a precursor chemical with the substrate. For the growth of metal oxides, a typical ALD cycle consists of alternating pulses of a metal precursor and a non-metal precursor or reactant. The growth process consists of many repetitions of this ALD cycle until the desired film thickness is achieved. For each ALD sub-cycle, a precursor dosage is carried to the surface of the substrate by a carrier inert gas. After the surface reaction saturates, the excess precursor and the reaction by-products are purged by the same carrier inert gas. Since the surface reactions usually saturate below coverage of one monolayer, ALD allows for some degree of atomic layer control of the deposition similar to MBE [22, 29-30]. A simple schematic of ALD is shown in figure 1.4. Inherent very low growth rate prevented ALD from being choice of growth until the last decade. ALD gained popularity as a thin-film growth method due to its capability of depositing high-*k* dielectric materials in high-aspect-ratio geometries (conformal growth) without pinholes. ALD is now utilized for the deposition of materials in a wide variety of applications including micro-electromechanical, catalytic, magnetic, and optical applications [22, 29-30].

The unique capabilities of ALD are based on the chemistry of the precursors used. Only those precursors that result in self-limiting growth through rapidly saturating surface reactions are proper for ALD growth. Self-limiting growth allows the same amount of material being deposited irrespective of the precursor dosing time. ALD precursors are desired to be volatile, should not etch or dissolve into the substrate, and

should not spontaneously decompose thermally at the growth temperature. The alternating nature of precursor delivery has advantage that there is no danger of gas-phase reactions occurring between the precursors and so more reactive versions of precursor chemicals can be used. The growth rate per cycle becomes constant above a certain precursor pulse time. In an ALD process, the film thickness is controlled only by the number of deposition cycles at a given temperature. One advantage of ALD over MBE is that there is no need to precisely control the source fluxes but one can still obtain atomic level composition control with good reproducibility. A major disadvantage is that there is often some unavoidable impurity inclusion from the precursor molecules and the carrier gas in ALD-grown films [22, 29-30].

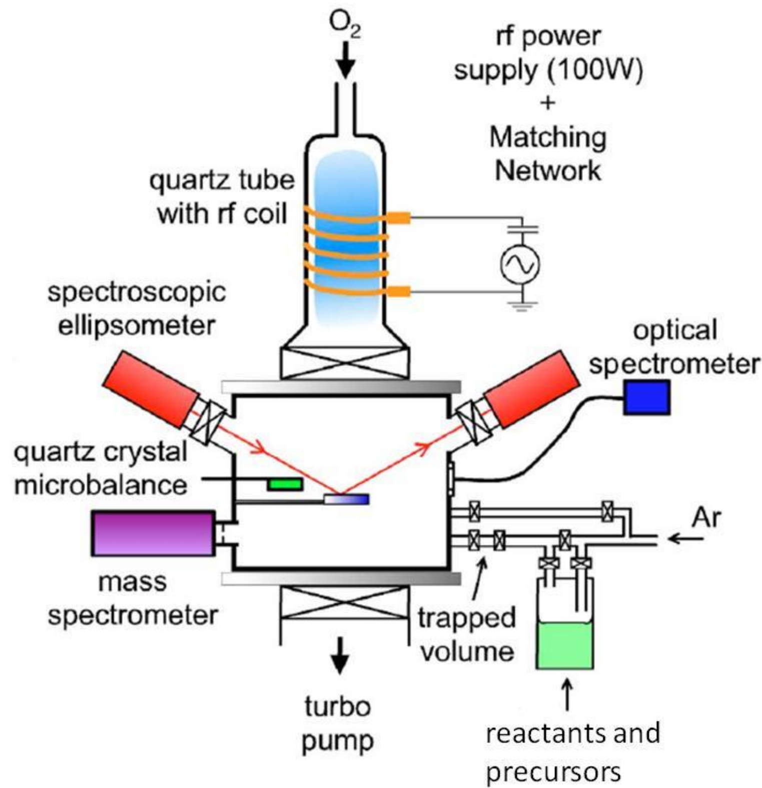

Figure 1.4: Schematic of ALD [30]

In ALD reactors an inert gas is flowed at a fixed flow rate such that the reactor pressure is constant in the range of 1–10 Torr. The substrate temperature is also very important critical growth parameters in ALD. The use of a too low temperature results in condensation of the precursor and hence in slowing down of the surface reaction. On the other hand, the use of a too high temperature leads to spontaneous decomposition of the precursor. Finding the growth temperature range where self-limiting growth occurs is critical. Hence, the ALD growth provides a fine way of depositing oxide thin films that are highly uniform, conformal, and pinhole-free. Because of its sub-monolayer saturation and self-limiting nature, ALD growth is highly repeatable with atomic-level control and provides the ability to grow multilayered materials without interdiffusion [22, 29-30].

1.2.3 Orientation Control and Substrate

Except for the most trivial properties (e.g., density), the functional properties of oxide thin films in general depend on orientation [31]. Hence optimal orientation(s) of epitaxial oxide films are needed for particular applications. For example, orientations that allow aligning the spontaneous polarization of a ferroelectric material with the direction of the applied electric field in order to maximize the polarization. The ability to control the orientation of the film through the choice of substrate, its orientation and the growth conditions is a key advantage of epitaxial growth. Orientation control is vital to the growth of phases that cannot be prepared as bulk single crystals due to their metastability, high melting temperatures, or phase transitions that occur on cooling [23].

The properties of oxide films can be improved by controlling film texture through local epitaxial growth mode for example the ion-beam-assisted deposition [31]. The

structural quality of the underlying crystalline substrate, on which an epitaxial film is grown, is very important. For the growth of superlattices of functional oxides, the availability of appropriate substrates and methods to prepare smooth, properly oriented and perfect surfaces on which the epitaxial growth is to be initiated are very crucial. Intensive research on high-temperature superconductors stimulated the research, development and production of many single-crystal perovskite substrates with excellent structural perfection rivaling that of conventional semiconductors. In addition, a suitable method to prepare the substrate with a specific chemical surface-termination is a prerequisite for atomic-layer-controlled thin-film growth of the epitaxial heterostructure. For example, $SrTiO_3$ substrates with two different terminations of SrO and TiO_2 yield different epitaxial films [23, 32-33].

1.3 Integration of Oxides

An important technological development is the ability to epitaxially integrate functional oxides with conventional semiconductors. Although the structural quality of films of functional oxides grown on semiconductor substrates is often far from the quality of these same materials grown on appropriate oxide substrates, significant improvements have been made over the last two decades [22]. Several substrates are now being used for the epitaxial integration of functional oxides with semiconductors, including Si (001), Ge (001), GaAs (001), InP (001) and GaN (0001). Using these routes, a multitude of functional oxides, with conducting top and bottom electrodes when desired, have been epitaxially integrated with semiconductor materials. This capability could play a significant role in future hybrid devices. Combining functional oxides with existing

semiconductor technology greatly enhances the materials properties available for use in microelectronics, optoelectronics, and spintronics, by bringing new functionalities to conventional semiconductor platforms [23, 34].

Epitaxial integration with silicon is particularly important because Si is the backbone of modern semiconductor technology. Unfortunately, direct growth of functional oxides on Si is frequently accompanied by extensive interdiffusion or chemical reactions that degrade the properties of the oxide, the underlying silicon, or both, leading to electrically active defects at the semiconductor/ oxide interface. Such defects at the semiconductor/oxide interface prevent many potential applications. Due to the difference in bonding natures, most of the oxides are incompatible with silicon substrates. Recent research activity has been focused on overcoming this fundamental obstacle through the identification of compatible buffer layers between silicon and functional oxides [22, 35].

Many factors such as chemical reaction, interdiffusion, crystal structure, and lattice mismatch must be considered in selecting materials for use as buffer layers between silicon and a particular oxide. It is important to avoid interfacial chemical reactions, i.e., to get a thermodynamically stable interface between the Si substrate and the functional oxide or the buffer layer [22]. The large differences in thermal expansion coefficients between silicon and oxides remain a significant problem. Upon cooling after growth, the functional oxide films are often in a state of biaxial tension, which can lead to cracking in thick films [35-37]. This will be discussed in detail in chapters 3 and 5.

1.4 Epitaxial Strain Engineering and Modulation Doping

An advantage of using thin films media to explore various physical effects is the ability to apply strains. These strains can be manifested in the form of differences in lattice parameters and thermal expansion behavior between the deposited film and the underlying substrate or they arise from defects formed during film deposition. Coherent epitaxial films have the advantage that high densities of threading dislocations are avoided. Strain fields around dislocations locally alter the properties of a film, making the ferroelectric properties inhomogeneous and often degraded. As the film is clamped to the substrate, but free in the out-of plane direction, the effect of a biaxial strain state on properties can be dramatic. The effects of biaxial strain and temperature on ferroelectric transitions and domain structures have been theoretically studied for a number of ferroelectrics [38-42].

As an example, $SrTiO_3$, which is not normally ferroelectric, become ferroelectric when strained [38]. These predictions imply that a biaxial tensile strain of order 1% can shift the T_c of $SrTiO_3$, a material that normally is not ferroelectric at any temperature, to the vicinity of room temperature [38]. Ferroelectricity in strained $SrTiO_3$ films has been confirmed by various experiments such as, dielectric constant versus temperature measurements, optical measurements as a function of temperature and applied fields, transmission IR measurements as a function of temperature showing changes in the soft modes, piezo-force microscopy measurements as a function of temperature, and conventional hysteresis loops as a function of temperature and orientation [38-40]. The combined experimental evidence from these methods is consistent with the predicted

effect of strain on the ferroelectric transition and antiferrodistortive transition of $SrTiO_3$. With strain, $SrTiO_3$ becomes a multiferroic material [38, 43].

Two-dimensional electron gases (2DEG) have been widely investigated in conventional semiconductors [1]. However, functional oxides have properties that are drastically different from conventional semiconductors. The perovskite $SrTiO_3$, for example, has an electron effective mass (m_e=5m_o), and dielectric constant (ε_r=20,000 at 4 K) which is orders of magnitude higher than conventional semiconductors, and the highest electron mobility (υ=22,000 cm^2/Vs at 2K) of any known oxide [1, 18]. This totally different set of electronic properties, coupled with the occurrence of superconductivity in properly electron-doped $SrTiO_3$, makes the study of the behavior of the 2DEG in $SrTiO_3$ of great interest [6]. The desire to study a 2DEG in $SrTiO_3$ was recently achieved experimentally using a $LaAlO_3/SrTiO_3$ heterostructure [18].

Modulation doping, which is the dominant technique used to realize 2DEGs in conventional semiconductors, is not unknown to oxides. Indeed, it occurs naturally in layered functional oxides, e.g., oxide superconductors, as ‘‘charge reservoir’’ layers donate their carriers to surrounding CuO_2 layers. In addition to the movement of charge (electronic compensation) relevant for the formation of a 2DEG, another way that an oxide may provide compensating charge is via charged defects such as oxygen deficiencies (ionic compensation) [23]. Modulation doping in oxides can be achieved by overcoming ionic compensation mechanisms [44]. Modulation doping has been applied artificially to oxides, although information on the band offsets, a critical element of bandgap engineering, is generally lacking for oxide heterojunctions. Modulation doping

can be engineered through the controlled growth of oxide heterostructures. The formation, study, and exploitation of 2DEG are an area with tremendous potential. Exploration of the behavior of ferroelectric, magnetic, or even spin-polarized 2DEGs is even possible [6, 18, 44].

1.5 Oxide Superlattices

Thin-film growth techniques offer powerful ways to synthesize new materials, including metastable ones that cannot be made by any other method. In the single layer films, metastable materials are possible through epitaxial stabilization. In multilayered films, the large difference between diffusion coefficients at the surface of the growing thin film compared with the much lower diffusion coefficients within the bulk of the film makes it possible to create two separate phases, even for materials that mix completely with each other in bulk form. For example, heterostructures involving ferroelectrics such as $BaTiO_3/SrTiO_3$ are metastable as it is energetically favorable for these oxides to dissolve into each other forming (Ba, Sr) TiO3 solid solutions. Although these superlattices are metastable, cation diffusion constants in oxides are sufficiently small that annealing at 1000°C for several hours is typically required before intermixing effects become measurable [23, 45].

As shown in figure 1.5, the interface abruptness and layer thickness control of oxide superlattices are comparable to AlAs/GaAs superlattices grown by MBE and MOCVD [23, 45]. Superlattices consisting of periodic stacking of thin functional oxide layers have been predicted or reported to possess many improved physical properties over homogeneous thin films of the same composition. Among the improved properties are

enhancement of dielectric constants and remnant polarization [1, 18, 23, 46]. The improved properties result from the large lattice mismatch leading to huge strains for adequate epitaxial growth [46-47]. Epitaxial heterostructures that make use of phase separation to form connectivities beyond the 2–2 connectivity of superlattices are also being explored by thin-film techniques.

Artificially layered superlattices of functional oxides are enormously important from both the technological and scientific standpoints. Modern deposition techniques makes possible to fabricate superlattices with essentially perfect interfaces with single-unit-cell precision. Superlattices of oxides hold the great potential for tailoring functional properties for particular application such that the properties of superlattices are far superior to the parent materials from which they have been fabricated [18, 23, 46-47].

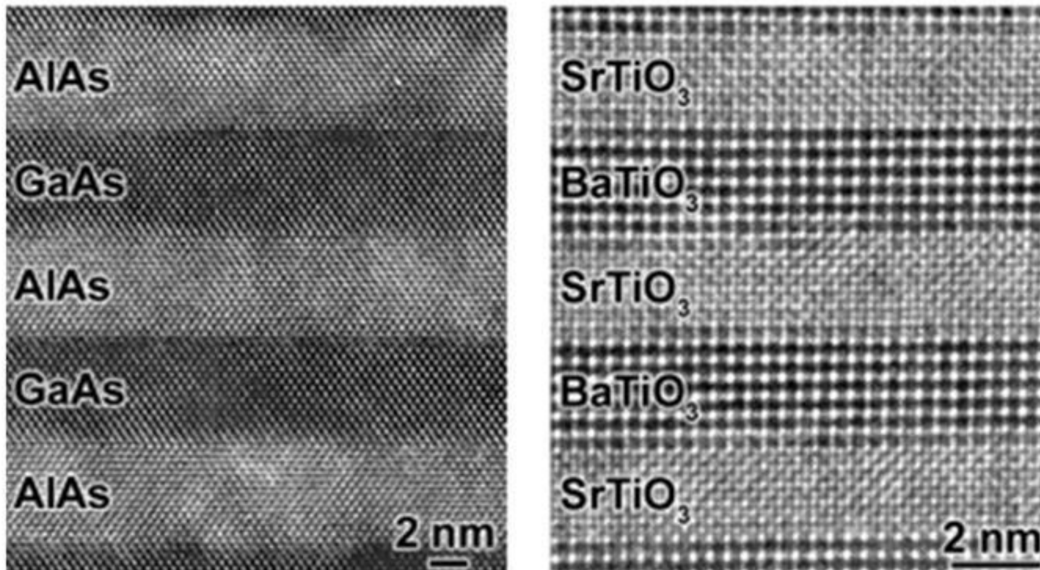

Figure 1.5 HRTEM images of GaAs/AlAs [45] and $BaTiO_3$/$SrTiO_3$ [23] heterostructures

Understanding of how the properties of the resulting superlattice material are related to those of the parent materials used is crucial for synthesizing superior materials. In superlattices of ferroelectric functional oxides where the in-plane lattice parameter of all the constituents is constrained to that of the underlying substrate, the primary consideration is the minimization of polarization mismatch between layers, with any mismatch giving rise to very high electrostatic energy [23, 47-48]. The elastic constraint imposed by the substrate is an important factor in determining the orientation of the polarization in the superlattice layers, and thus has a dramatic effect on the superlattices properties.

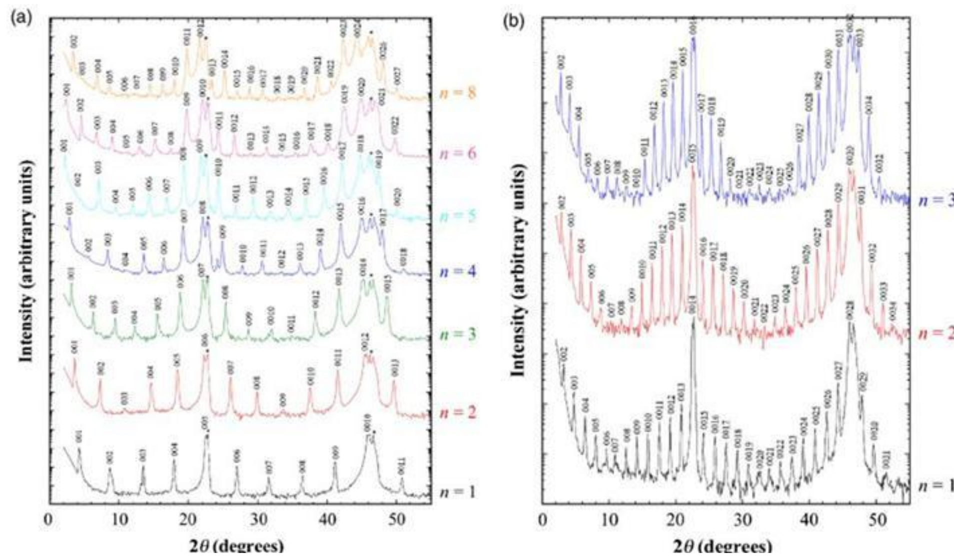

Figure 1.6: θ-2θ XRD scans of $(BaTiO_3)n/(SrTiO_3)m$ superlattices for (a) m=4 and n=1-6, 8 and (b) m=13 and n=1-3. Substrate peaks are marked by star [49]

Relaxation due to misfit dislocations can cause changes in the orientation of the polarization for example in the $SrTiO_3$ layers of relaxed $BaTiO_3/SrTiO_3$ superlattices [48]. These superlattices can be denoted by $(BaTiO_3)n/(SrTiO_3)m$, where n and m refer to the thickness, in unit cells, of the (001)p $BaTiO_3$ and (001)p $SrTiO_3$ layers, respectively.

The regularity of these superlattices grown by MBE is demonstrated by the presence and sharpness of all of the superlattice reflections in their XRD patterns, as shown in figure 1.6 [49]. The presence of virtually all satellite peaks in these superlattices confirms their macroscopic structural perfection [49].

The use of thin film techniques for the growth of functional oxides is under development and many challenges remain to be overcome for these techniques to develop greater structural control at the atomic layer level, reproducibility, and ultimately precise control of electronic, optical, and spintronic properties. MBE and ALD are becoming established as extremely accurate methods of choice for synthesizing epitaxial films and heterostructures of functional oxides. MBE is the premier synthesis technique for the synthesis of layered oxides, with customized layering control down to the atomic layer level [22-23]. As the complexity and metastability of desired functional oxides and heterostructures involving functional oxides increases, the need to improve these atomic layer engineering techniques will become all the more important. Accurate composition control is key to the controlled growth of such structures and with improvements in composition control, further improvements in the perfection of the layering control attainable in the growth of functional oxides by MBE are expected [50-51]. Today's multiscale modeling techniques are a tremendous aid in identifying likely locations for improved functional materials and predicting the properties of new materials [52]. Many of these new functional oxides are metastable and others attain their improved functionality via strain engineering [51].

1.6 Overview of Dissertation

In this dissertation, the microstructure, chemical composition, electronic structure and interface structure of oxide thin films grown on silicon and oxide substrates were characterized using HRTEM, image simulations, selected-area electron diffraction, HRSTEM, EDX and EELS. Research results are presented for the following major projects: (i) Al-doped $SrTiO_3$ for microelectronics, (ii) Co-doped $SrTiO_3$ as ferromagnet, (iii) Spinel Co_3O_4 thin films on $MgAl_2O_4$, (iv) NbO_x thin films on STO and LSAT, and (v) Growth of Zintl $SrAl_4$ on $LaAlO_3$. Synthesis of these thin films has been described very briefly. TEM characterization of these materials has been described in detail, with the intent to characterize and further understand the morphology of these materials.

In Chapter 2, experimental details are presented for various TEM techniques including HRTEM, image simulations, Geometric Phase Analysis, STEM-EDX and STEM-EELS, and sample preparation using mechanical polishing and grinding.

In Chapter 3, the results of HR(S)TEM, STEM-EDX, and STEM-EELS investigation of Al-doped and Co-doped $SrTiO_3$ are presented. The microstructure, chemical composition and electronic structure of doped-STO are investigated in detail. It was found that Al substitutes Ti sites, while Co partially substitutes Ti with associated oxygen vacancies forming Co-O complexes.

In Chapter 4, $Co_3O_4/MgAl_2O_4$ spinel heterostructure are characterized using HRTEM and image simulations. $MgAl_2O_4$ substrates were found to be Al-O terminated. Defects and associated strain fields in spinel heterostructure were investigated.

In Chapter 5, NbO_x thin films deposited on STO and LSAT are discussed. Microstructure, crystal structure and lattice constants were determined. Interface structure was investigated using HRTEM and image simulations. Zintl $SrAl_4$ thin-films grown on LAO were investigated for interface structure. $SrAl_4$ terminated with Sr on AlO_2-terminated LAO was found to be the interface with minimum energy.

In Chapter 6, the findings of chapters 3, 4, and 5 are summarized and recommendations for further research related to oxide thin films and oxide-oxide interfaces are presented.

References

1. J. Mannhart and D. G. Schlom, Science 327, 1607 (2010).

2. J. M. Rondinelli and N. A. Spaldin, Adv. Mater. 2011, 23, 3363–3381

3. C. H. Ahn, K. M. Rabe, J.-M. Triscone, Science 303, 488 (2004).

4. L.W. Martin, Y.-H. Chu, R. Ramesh, Materials Science and Engineering R 68 (2010) 89–133.

5. S. Stemmer and S. J. Allen, Annu. Rev. Mater. Res. 2014, 44:151–71.

6. J. Mannhart, D.H.A. Blank, H.Y. Hwang, A.J. Millis, and J.-M. Triscone, MRS Bulletin, Volume 33, November 2008, 1027-1034.

7. H. Y.Hwang, MRS Bulletin, Volume 31, January 2006, 28-35.

8. H. Y. Hwang, Y. Iwasa, M. Kawasaki, B. Keimer, N. Nagaos and Y. Tokura, Nature Materials, Vol. 11, FEB. 2012, 103-113.

9. F. M. Granozio, G. Koster, and G. Rijnders, MRS Bulletin, Volume 38, December 2013, 1017-1023.

10. L Bjaalie1, B Himmetoglu, L Weston, A Janotti and C G Van de Walle, New Journal of Physics 16 (2014) 025005.

11. Koida, M. Lippmaa, T. Fukumura, K. Itaka, Y. Matsumoto,M. Kawasaki, and H. Koinuma, Phys. Rev. B, 66 [14] 144418 (2002).

12. Yamada, M. Kawasaki, T. Lottermoser, T. Arima, and Y. Tokura, Appl. Phys. Lett., 89 [5] 052506 (2006).

13. Bhattacharya, X. Zhai, M. Warusawithana, J. N. Eckstein, and S. D. Bader, Appl. Phys. Lett., 90 [22] 222503 (2007).

14. J. May, A. B. Shah, S. G. E. te Velthuis, M. R. Fitzsimmons, J. M. Zuo, X. Zhai, J. N. Eckstein, S. D. Bader, and A. Bhattacharya, Phys. Rev. B, 77 [17] 174409 (2008).

15. Bhattacharya, S. J. May, S. G. E. te Velthuis, M. Warusawithana, X. Zhai, B. Jiang, J.-M. Zuo, M. R. Fitzsimmons, S. D. Bader, and J. N. Eckstein, Phys. Rev. Lett., 100 [25] 257203 (2008).

16. Ohtomo and H. Y. Hwang, Nature, 427 [6973] 423–6 (2004).

17. Brinkman,M. Huijben,M. vanZalk, J. Huijben,U. Zeitler, J.C.Maan,W.G. van der Wiel, G.Rijnders, D. H. A. Blank, andH. Hilgenkamp, Nat. Mater., 6 [7] 493–6 (2007).

18. Reyren, S. Thiel, A. D. Caviglia, L. Fitting Kourkoutis, G. Hammerl, C. Richter, C. W. Schneider, T. Kopp, A.-S. Ruetschi, D. Jaccard, M. Gabay, D. A. Muller, J.-M. Triscone, and J. Mannhart, Science, 317 [5842] 1196–9 (2007).

19. S. N. Ruddlesden and P. Popper, Acta Cryst., 11 [1] 54–5 (1958).

20. G. Rijnders, Nature Materials Vol. 13, 844-845 (2014).

21. J. H. Lee, G. Luo, I. C. Tung, S. H. Chang, Z. Luo, M. Malshe, M. Gadre, A. Bhattacharya, S. M. Nakhmanson, J. A. Eastman, H. Hong, J. Jellinek, D. Morgan, D. D. Fong and J. W. Freeland, Nature Materials 13, 879–883 (2014).

22. A. A. Demkov and A. B. Posadas, Integration of Functional Oxides with Semiconductors, Springer 2014.

23. D. G. Schlom, L. Q. Chen, X. Pan, A. Schmehl, and M. A. Zurbuchen, J. Amer. Ceram. Soc., 91; [8] 2429–2454 (2008).

24. R. Ramesh, K. Luther, B. Wilkens, D. L. Hart, E. Wang, J. M. Tarascon, A. Inam, X. D. Wu, and T. Venkatesan, Appl. Phys. Lett., 57 [15] 1505–7 (1990).

25. B. Chrisey, and G. K. Hubler (Ed), Pulsed Laser Deposition of Thin Films. Wiley, New York, 1994.

26. D. G. Schlom, J. N. Eckstein, E. S. Hellman, S. K. Streiffer, J. S. Harris Jr., M. R. Beasley, J. C. Bravman, T. H. Geballe, C. Webb, K. E. von Dessonneck, and F. Turner, Appl. Phys. Lett 53 [17] 1660–2 (1988).

27. J. Eckstein and I. Bozovic, Annu. Rev. Mater. Sci., 25, 679–709 (1995).

28. M. de Keijser and G. J. M. Dormans, MRS Bull., 21 [6] 37–43 (1996).

29. A.C. Jones, M. Hitchman (eds.), Chemical Vapor Deposition: Precursors, Processes and Applications (RSC Publishing, Cambridge, 2009) Chap. 4.

30. S. B. S. Heil, J. L. van Hemmen, M. C. M. van de Sanden, and W. M. M. Kessels, J. Appl. Phys., 103, 103302 (2008)

31. R. Ramesh and D. G. Schlom, Science, 296 [5575] 1975–6 (2002).

32. J. M. Phillips, J. Appl. Phys., 79 [4] 1829–48 (1996).

33. A. G. Schrott, J. A. Misewich, M. Copel, D. W. Abraham, and Y. Zhang, Appl. Phys. Lett., 79 [12] 1786–8 (2001).

34. J. Lettieri, J. H. Haeni, and D. G. Schlom, J. Vac. Sci. Technol. A, 20 [4] 1332–40 (2002).

35. S. Matsubara, T. Sakuma, S. Yamamichi, H. Yamaguchi, and Y. Miyasaka, pp. 243–53 in Ferroelectric Thin Films, Materials Research Society Proceedings, Vol. 200, Materials Research Society, Pittsburgh, PA, 1990.

36. M. Suzuki, J. Ceram. Soc. Jpn. Int. Ed., 103 [11] 1088–99 (1995).

37. K. J. Hubbard and D. G. Schlom, J. Mater. Res., 11 [11] 2757–76 (1996).

38. D. G. Schlom, L. Q. Chen, C. B. Eom, K.M. Rabe, S. K. Streiffer, and J.-M. Triscone, Annu. Rev.Mater. Res., 37, 589–626 (2007).

39. T. R. Taylor, P. J. Hansen, B. Acikel, N. Pervez, R. A. York, S. K. Streiffer, and J. S. Speck, Appl. Phys. Lett., 80 [11] 1978–80 (2002).

40. M.-W. Chu, I. Szafraniak, R. Scholz, C. Harnagea, D. Hesse, M. Alexe, and U. Gosele, Nat. Mater., 3 [2] 87–90 (2004).

41. S. P. Alpay, I. B. Misirlioglu, V. Nagarajan, and R. Ramesh, Appl. Phys. Lett., 85 [11] 2044–6 (2004).

42. V. Nagarajan, C. L. Jia, H. Kohlstedt, R. Waser, I. B. Misirlioglu, S. P. Alpay, and R. Ramesh, Appl. Phys. Lett., 86 [19] 192910 (2005).

43. A. Vasudevarao, A. Kumar, L. Tian, J. H. Haeni, Y. L. Li, C.-J. Eklund, Q. X. Jia, R. Uecker, P. Reiche, K. M. Rabe, L. Q. Chen, D. G. Schlom, and V. Gopalan, Phys. Rev. Lett., 97 [25] 257602 (2006).

44. R. J. Cava, Science, 247 [4943] 656–62 (1990).

45. A. K. Gutakovskii, L. I. Fedina, and A. L. Aseev, Phys. Status Solidi A, 150 [1] 127–40 (1995).

46. S. M. Nakhmanson, K. M. Rabe, and D. Vanderbilt, Phys. Rev. B, 73 [6] 060101 (2006).

47. L. Kim, D. Jung, J. Kim, J. S. Kim, and J. Lee, Appl. Phys. Lett., 82 [13] 2118–20 (2003).

48. Y. L. Li, S. Y. Hu, D. Tenne, A. Soukiassian, D. G. Schlom, L. Q. Chen, X. X. Xi, K. J. Choi, C. B. Eom, A. Saxena, T. Lookman, and Q. X. Jia, Appl. Phys. Lett., 91 [25] 252904 (2007).

49. A. Soukiassian, W. Tian, V. Vaithyanathan, J. H. Haeni, L. Q. Chen, X. X. Xi, D. G. Schlom, D. A. Tenne, H. P. Sun, X. Q. Pan, K. J. Choi, C. B. Eom, Y. L. Li, Q. X. Jia, C. Constantin, R. M. Feenstra, M. Bernhagen, P. Reiche, and R. Uecker, J. Mater. Res., 23 [5] 1417–1432 (2008).

50. A. A. Demkov, P. Ponath, K. Fredrickson, A. B. Posadas, M. D. McDaniel, T. Q. Ngo, and J. G. Ekerdt, Microelectronic Engineering Volume 147 (2015) 285-289.

51. Schlom, D., L. Q. Chen, C. Fennie, V. Gopalan, D. Muller, X. Q. Pan, R. Ramesh, R. Uecker. MRS Bulletin (2014) 39 118-130.

52. C. Ederer and N. A. Spaldin, Phys. Rev. Lett., 95 [25] 257601 (2005).

CHAPTER 2

EXPERIMENTAL TECHNIQUES

2.1 Transmission Electron Microscopy

The Transmission Electron Microscope (TEM) is a highly versatile instrument that provides structural and chemical information about materials, thin films and interfaces over a wide range of magnification. The TEM consists of an illumination system, an image-formation system, and a viewing screen or recording device. The illumination system consists of an electron source that provides an intense beam of high-energy electrons and condenser lenses that transfer electrons to the specimen giving either a broad beam or a focused beam. The image-forming system consists of an objective lens, one or more intermediate lenses and a projector lens. The role of the objective lens is to form the first intermediate image or electron diffraction pattern which are then magnified and projected onto the viewing screen or final detector by the intermediate and projector lenses [1].

The operating modes of the Conventional Transmission Electron Microscope (CTEM) include amplitude or diffraction contrast imaging, where only a fraction of the electrons that have passed through the sample are used to form the final image. This mode is achieved by locating an objective aperture in the back focal plane of the objective lens. Diffraction-contrast imaging provides detailed information about the strain associated with crystal defects and the distribution of different crystallographic phases. Many common structural defects, such as dislocations, stacking faults, and grain

boundaries, have a highly characteristic appearance under diffraction contrast conditions. Every defect can be characterized in terms of local displacements away from the perfect crystal atom positions. The amplitude of the diffracted beam is sensitive to the displacement vector $\mathbf{\Delta r}$ and to the deviation parameter $\mathbf{s}$, indicative of deviation from the exact Bragg condition: $\mathbf{\Delta k}=\mathbf{g}$, where $\mathbf{\Delta k}$ is the difference between the incident and scattered wave vectors and $\mathbf{g}$ is the reciprocal lattice vector. By comparing the defective and perfect crystal regions, a phase difference of $\mathbf{g}\cdot\mathbf{\Delta r}$ can be found, and this difference determines the image contrast at the defect [1].

Selected-Area Electron Diffraction (SAED) patterns can be obtained at the back focal plane of the objective lens. The SAED pattern is used to orient samples with respect to the incident electron beam direction. When the SAED pattern is calibrated by reference to a known sample, then lattice spacings and angles of unknown specimens can be determined. By combining beam tilt and specimen tilt, various forms of diffraction contrast imaging can be realized such as bright field, dark field and weak-beam dark field. One limitation of the diffraction contrast technique is that the position of the dislocation image does not correspond exactly to the position of the dislocation core, because this contrast arises from variations in the orientation of crystal planes around the defect. In order to study directly the microstructural nature of defects, and the atomic configuration of the material, high-resolution TEM is indispensable [1-3].

2.2 High Resolution Transmission Electron Microscopy (HRTEM)

HRTEM is a technique in which a much larger objective aperture is used in imaging. Multiple beams that pass through the specimen interfere with each other and the contrast across the image depends upon the relative phases of the various interfering beams. Hence, HRTEM is often called phase-contrast imaging. The image-forming objective lens affects the phase of the electron beam, adding complexity to the image contrast. High contrast images are often hard to decipher and may not be useful for quantitative measurements. However, when the microscope imaging conditions such as beam alignment, defocus and lens aberrations are properly adjusted, it is possible to interpret phase contrast images quantitatively using image simulations. Individual atomic columns can be separately resolved in many crystalline materials using the latest generations of HRTEM instruments. Over the last few decades, HRTEM has evolved into a major materials characterization technique at the nanometer scale. Important applications of HRTEM include determining the microstructure of crystalline defects, interfaces and grain boundaries, investigating nanocrystalline features in amorphous films, and studying small-particle catalysts [2-3].

Image formation in the TEM can be considered as a two-step process. The first step is electron-specimen scattering as the incident electron beam interacts very strongly with the sample, undergoing both elastic and inelastic scattering. Electrons that are elastically scattered mainly contribute to the high-resolution bright-field image. Strong beam-specimen interactions mean that the electron beam can be scattered multiple times as it traverses through the specimen. Multiple scattering events are described by

dynamical theory as the kinematical scattering approximation is inadequate for understanding image formation except for the very thinnest parts of the specimen. With thick samples and multiple electron scattering, phase changes are usually quite large. Hence, knowledge about the relative heights and locations of different atoms in the specimen becomes important for quantitative interpretation of image features. Image simulation becomes an integral part of quantitative HRTEM for extracting detailed information about atomic arrangements at dislocations and interfaces. The electron beam emerging from the exit surface of the sample is often described as the exit-surface wavefunction [2-3].

In the second part of image formation, the exit-surface wavefunction passes through the objective lens, and additional magnifying lenses are used to form the final image. The wavefunction undergoes additional phase changes and interference before reaching the final imaging plane. The objective lens is the most important lens since resolution and aberrations affecting HRTEM images are determined by this lens. Subsequent lenses in the TEM column usually magnify the image formed by the objective lens but without affecting image resolution and major aberrations. In HRTEM, the recorded image is not usually a direct representation of crystallographic structure of the sample since high image intensity may or may not indicate the presence of an atomic column at that location. The relationship between the exit wavefunction and the image wavefunction is highly nonlinear and is described by the Phase Contrast Transfer Function (PCTF) [2, 4].

For the weak-phase-object (very thin specimen) approximation, the amplitude in the back focal plane of the objective lens is given by:

$$Q(u) = \delta(u) + \sigma\Phi(u)E(u)A(u)\sin[\chi(u)] \quad \text{.................................(1)}$$

where u is the spatial frequency, given by $|u| = \frac{2\sin\theta}{\lambda}$,

θ is scattering angle and λ is the electron wavelength, $\delta(u)$ is the transmitted beam, σ is the interaction constant, $\Phi(u)$ is the object function, $E(u)$ represents the envelope functions which describe attenuation of the wavefunction at higher spatial frequency, $A(u)$ is the objective aperture function, and $\sin[\chi(u)]$ is a phase factor that should be maximized for the largest possible range of u. The PCTF is defined as:

$$T(u) = E(u)A(u)\sin[\chi(u)] \quad \text{..(2)}$$

Therefore, in terms of PCTF, the image amplitude referred back to object plane becomes:

$$\psi'(r) = \psi(r) * t(r) \quad \text{..(3)}$$

Where * represents the convolution integral, and $\psi(r)$ and $t(r)$ are Inverse Fourier Transforms of Q(u) and T(u). $\chi(u)$ is given by:

$$\chi(u) = \Delta f\, \lambda\pi u^2 + \pi C_s^3 \frac{u^4}{2} \quad \text{..(4)}$$

Where Δf is the defocus, and C_s is the spherical aberration coefficient of the objective lens. The PCTF is a function of defocus and lens aberrations, and is highly oscillatory at higher spatial frequencies. Thus, electrons scattered to different angles undergo reversals

in phase. These phase reversals causes artifacts in the final image that often require image simulations before the image is interpretable [4-5].

The damping envelope function E(u) represents loss of coherence from focal spread (temporal coherence) and finite beam divergence (spatial coherence) at larger scattering angles. Thus, specimen information scattered to higher spatial frequencies is lost. The interpretable or structural resolution is defined at the optimum or Scherzer defocus, where the PCTF has the largest possible band of spatial frequencies without any phase reversal. In other words, the first zero cross-over, as indicated by the arrow in figure 2.1, gives the interpretable resolution.

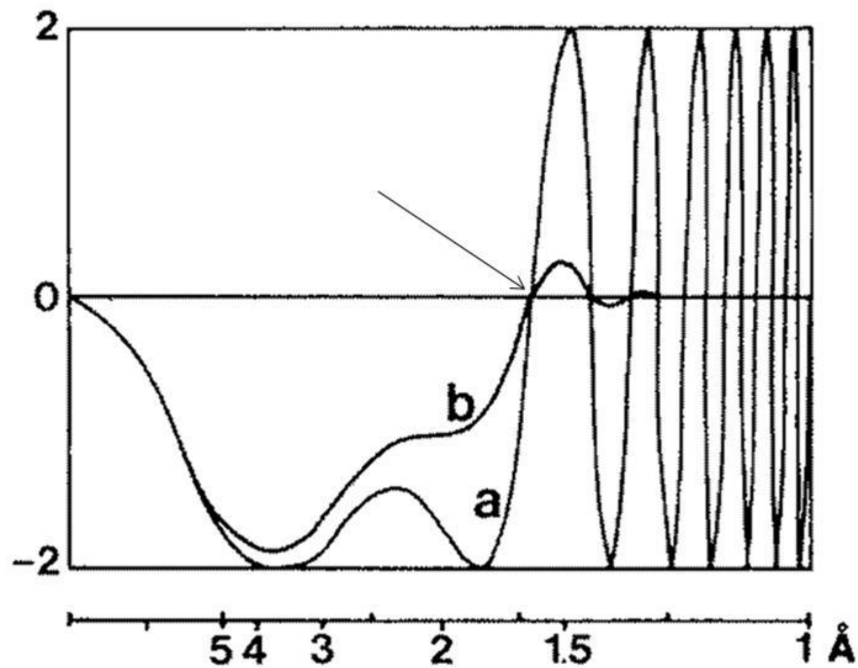

Figure 2.1: Comparison of PCTF curves for a 400 keV HREM, axial illumination, C_S= 1.0 mm. (a) coherent illumination, no damping functions; (b) effect of damping functions for a focal spread of 8 nm and an incident illumination semi-angle of 0.5 mrad. Arrow indicates the interpretable resolution limit [3].

The positions of the PCTF zeroes are not affected by the envelope functions unlike the information transfer at higher spatial frequencies. The envelope functions define the instrumental resolution or information limit of the HRTEM. A value of ~15% [exp(–2)] is usually taken as the resolution cutoff since this level is commonly regarded as the minimum acceptable for image-processing requirements. By using field-emission electron sources, the instrumental resolution limit can extend well beyond the interpretable resolution limit [4-5].

The PCTF oscillations lead to very fine details in HRTEM images that are not directly related to the specimen features [5]. Phase modulations caused by the PCTF can be reduced by inserting a suitable-sized objective aperture to prevent beams with inverted phase from contributing to the image [3] or they can be removed by a *posteriori* image processing such as focal-series reconstruction [6]. The lattice-fringe resolution refers to the very finest fringe spacing that can be obtained as a result of interference between two or more diffracted beams. Better instrumental stability, less external noise, reduced stray magnetic fields and vibration-free environment are critical for finer fringe spacing [6, 7]. Fine lattice fringes do not necessarily contain any useful local information about atomic structure since the HRTEM images may be recorded at significant underfocus conditions when there are many PCTF oscillations and the interfering diffracted beams can originate from comparatively large specimen areas [4-5]. Very few HRTEM lattice images are directly interpretable in terms of atomic arrangements because of the phase reversals that are caused by PCTF oscillations when the defocus is changed. Finding the optimum image defocus for given sample thickness can become a major issue. Dynamical multiple scattering causes further complications in thicker crystals as the intensity of the direct

beam is reduced when the sample thickness is increased. The direct beam might become so low in intensity that the image is then dominated by second-order interference processes between many different diffracted beams [3-5, 8].

By increasing the electron accelerating voltage, the electron wavelength is reduced, so that the interpretable resolution can be improved. However, higher accelerating voltage is not always desirable as the likelihood of electron radiation damage of specimen is higher, and maintaining the stability of power supplies at high accelerating voltages is more demanding. The power supply for the objective lens current must also be highly stable [8]. The objective lens current determines its focal length and spherical aberration coefficient. Therefore, TEMs are usually operated with fixed current and the lens current should be monitored continuously. The sample height should then be adjusted whenever the sample is tilted or another field of view is selected. The sensitivity of the image appearance to defocus means that knowledge of this parameter is essential for correct image interpretation. Optimum defocus and local specimen thickness can be determined by cross-correlating experimental and simulated images [7, 9].

2.3 HRTEM Image Simulations

Image simulations were originally used to explain ambiguities in the HRTEM image contrast of complex oxides in which heavy metal sites sometimes appeared dark and other times bright [10]. Image simulations have become indispensable for quantitative HRTEM in recent years. Important uses of image simulations include interpreting high-resolution information recorded in experimental micrographs,

improving the resolution, determining structure using proposed models, analyzing crystal defects, and understanding the effect of microscope parameters [11].

The HRTEM provides a very powerful instrument for investigating microstructural details of many types of structures at the atomic scale. Even for thin samples, the electron beam interacts very strongly with the specimen leading to multiple dynamical scattering by the sample. The dynamical scattering influences the image appearance such that it is no longer related to the specimen structure in a simple intuitive manner. In addition, the amplitudes and phases of the transmitted beams are influenced by the aberrations of the objective lens. The goal of image simulation is to interpret the image: to separate the effects of the specimen and the instrument on the image, and to unravel the effects of multiple scattering. Reliable analysis of a materials interface needs theoretical understanding of image contrast simulations [12-13].

There are two primary techniques for calculating a transmission electron microscope image: the Bloch-wave method, and the multislice method. In the Bloch-wave method, the electron wave function is expanded in terms of Bloch waves inside a crystalline specimen. These Bloch waves have the same periodicities as the specimen and satisfy the Schrodinger equation. The eigenvalue and eigenvector components of Bloch waves can be determined by solving the fundamental equations of dynamical theory [10-11, 14]. The phase-shift term in the image intensity distribution contains defocus Δz and the spherical aberration coefficient C_s, and hence it is impossible to image a large number of hkl Bragg reflections around an [mno] zone axis with $mh + nk + ol = 0$ with the same phase shifts. Thus, the superposition of the reflection amplitudes in the image becomes

incorrect [11, 14]. For better accuracy, Bloch-wave analysis requires a large number of eigen-vectors. Hence, the method is preferred for small perfect crystals. The computer time needed scales as N^3 where N is the number of Bloch waves or Fourier components (N increases with resolution). The major limitation of the Bloch-wave method is a practical limitation on the number of Fourier components that can be used [11].

The Multislice Method is the most versatile and most widely used method of image simulation. It was introduced by Cowley and Moodie [15], and numerically solved for the first time by Goodman and Moodie [16]. The Fast-Fourier-Transform (FFT) based multislice method, which is numerically highly efficient, was developed by Ishizuka and Uyeda [17], and simultaneously by Bursill and Wilson [11]. The major limitation of the Bloch-wave method of limited Fourier components, as mentioned earlier, is overcome in the multislice method by factoring the electron wavefunction into a slowly changing component and a fast changing wavelength-dependent phase part. Hence, sampling of the slowly varying portion may be spaced many wavelengths apart. Using efficient FFT, the computing time scales roughly as N*log(N) where N is the number of Fourier components (N increases with resolution) [11]. The multislice method is applicable to both perfect and defective crystals with large unit-cell parameters. The specimen is sliced perpendicular to the direction of propagation of the incident plane wave which enters the specimen at one side, propagates through the specimen and exits at the other side. The specimen is divided into many slices, each of which is thin enough to be approximated by a simple phase shift of the electron beam. The electron beam propagates between slices as a small-angle outgoing wave (Fresnel diffraction). The wave is transmitted through a slice of thickness (Δz) and then propagates a distance Δz to the next layer [11, 14].

The multislice method typically involves the following steps [11]:

Step 1: Divide the specimen into thin slices of same thickness Δz perpendicular to the direction of the incident electron beam.

Step 2: Calculate the projected atomic potential $V_{zn}(\mathbf{r})$ and phase shift $\sigma(x, y)$ for each slice by integrating the crystal potential $V(\mathbf{r})$ between limits $(n-1)\Delta z$ and $n\Delta z$ for the nth slice.

Step 3: Calculate the transmission function $t_n(\mathbf{r}) = \exp[i\sigma V_{zn}(\mathbf{r})]$ for each slice.

Step 4: Initialize the incident wavefunction $\psi_0(x, y) = 1$.

Step 5: Recursively transmit and propagate the wavefunction through each slice $\psi_{n+1}(x, y) = P_n(x,y,\Delta z_n)*[t_n(x, y)\psi_n(x, y)]$, where P_n is the Fresnel propagator for wave propagation through vacuum and t_n is the transmission function defined earlier. The transmission function is applied at the center or bottom of the slice. $*$ is a convolution integral. Repeat until the wavefunction is all the way through the specimen thickness. For crystalline materials, this integral becomes a sum over the reciprocal lattice vectors **g**. Higher accuracy demands a very large number of slices and hence the smallest possible slice thickness. In practice, Δz should be close to 0.25–0.33 of the unit-cell dimensions [11, 14].

Step 6: The calculations are conveniently done in Fourier space. Fourier transform the wave function at the exit surface of the specimen $\Psi_n(k_x, k_y) = FT[\psi_n(x, y)]$.

Step 7: Multiply the transmitted wave function $\Psi_n(k_x, k_y)$ by the transfer function of the objective lens $T(\mathbf{k})$ defined in section 2.2, to get the diffraction pattern in the back focal plane $\Psi_i(\mathbf{k}) = T(\mathbf{k})\Psi_n(\mathbf{k})$.

Step 8: The inverse Fourier transform of the diffraction pattern yields the wavefunction $\psi_i(\mathbf{r}) = FT^{-1}[\Psi_i(\mathbf{k})]$.

Step 9: Final image intensity can be calculated by finding square modulus of the image wavefunction (in real space) $g(\mathbf{r}) = |\psi_i(\mathbf{r})|^2 = |\psi_n(\mathbf{r}) * T(\mathbf{r})|^2$.

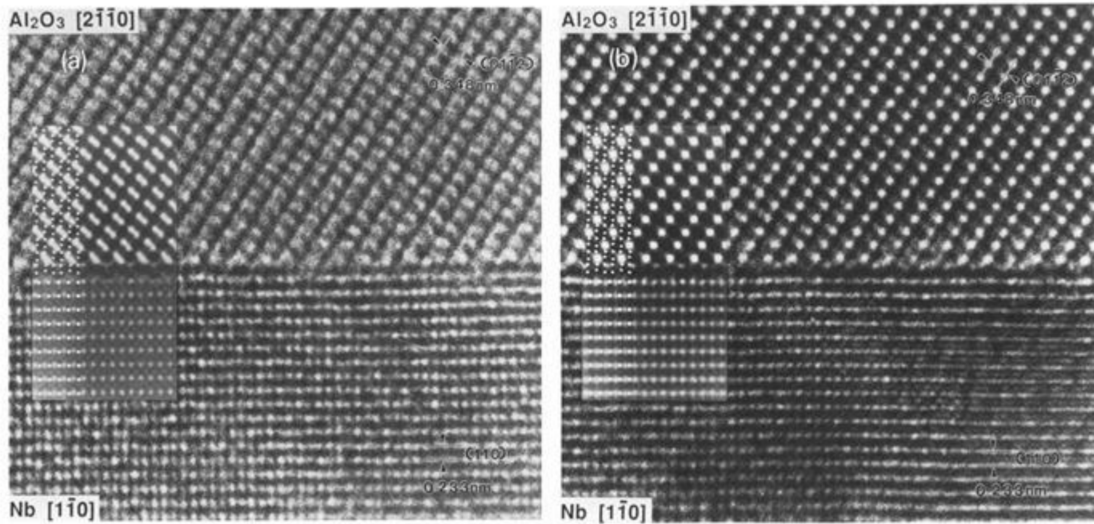

Figure 2.2: Al_2O_3/Nb interface. HRTEM images at defocus value $\Delta f = 40$ nm and (b) $\Delta f = 50$ nm. The insets represent simulated images for the interface model [18]

Figure 2.2 is an example of image simulation, showing HRTEM images of Al_2O_3/Nb interface at defocus value (a) $\Delta f = 40$ nm, and (b) $\Delta f = 50$ nm, and the insets represent the simulated images for the interface model [18].

In this dissertation research, the atomic models of crystals and interfaces were created using the commercial software package Crystalmaker by supplying individual

atom positions and symmetry information. These crystal models were then imported into the commercial software program JEMS for simulation studies. JEMS (Java Electron Microscope Simulator) is a comprehensive electron microscopy simulation package developed by Stadelmann for electron diffraction analysis, HRTEM and HRSTEM image simulations [19]. JEMS can be used to calculate images using both Multislice and Bloch-wave analysis methods, and it can handle unit cells with small defects or large cells with extended defects. In this dissertation work, HRTEM images have been calculated using the Multislice method and diffraction analysis was done using the Bloch-wave approach.

2.4 Geometric Phase Analysis

Quantitative analysis of the strain in oxide thin films is becoming increasingly important, particularly since film thicknesses are being reduced and different film/substrate combinations are being used to achieve multifunctionality. Strain measurements must be carried out at smaller and smaller length scales and with increasing accuracy and reliability. In this respect, HRTEM has become a powerful tool for mapping strain at the nanoscale due to the development of quantitative methods such as Geometric Phase Analysis (GPA) [20-21].

An HRTEM image formed at a crystal zone axis consists of an interference pattern of fringes that are related to the atomic planes of the specimen. These interference fringes can be used individually to extract information concerning strain. The GPA technique measures the displacement of lattice fringes with respect to a perfect lattice (for example, a region of unstrained substrate). The method is based on calculation of the local Fourier components of the lattice fringes. The phases of these local Fourier

components, or geometric phase $P_g(\mathbf{r})$, are directly related to the components of the displacement field, $\mathbf{u}(\mathbf{r})$, in the direction of the reciprocal lattice vector, **g** as given by:

$$P_g(\mathbf{r}) = -2\pi\mathbf{g}.\mathbf{u}(\mathbf{r}) \qquad \text{...(5)}$$

It is assumed that the displacement field is constant along the electron-beam direction through the foil or if there are small variations, that they are averaged out [20]. When the geometric phase of two diffracted beams is known, the displacement field can be determined as:

$$\mathbf{u(r)} = -(1/2\pi)*(P_{\mathbf{g1}}(\mathbf{r})\mathbf{a_1} + P_{\mathbf{g2}}(\mathbf{r})\mathbf{a_2}) \qquad \text{..(6)}$$

where $\mathbf{a_1}$ and $\mathbf{a_2}$ are the real-space basis vectors corresponding to the reciprocal lattice defined by $\mathbf{g_1}$ and $\mathbf{g_2}$. In the GPA, the geometric phases of any two lattice fringes are enough, as long as their reciprocal lattice vectors are non-collinear. In practice, the lattice fringes giving the best signal-to-noise are chosen. The two-dimensional deformation tensor can be obtained by differentiating the displacement field $\mathbf{u(r)}$ given by:

$$\varepsilon_{ij} = \frac{1}{2}\left(\frac{\partial u_i}{\partial x_j} + \frac{\partial u_j}{\partial x_i}\right) \qquad \text{...(7)}$$

In a similar way, the local in-plane rigid-body rotation is given by:

$$\omega_{ij} = \frac{1}{2}\left(\frac{\partial u_y}{\partial x} - \frac{\partial u_x}{\partial y}\right) \qquad \text{..(8)}$$

For small rotations, the angle is in rad and anticlockwise rotations are taken as positive. The more developed calculations for large deformations are often not necessary [20-21].

Deformation and strain are different, because strain in a mechanical sense can only be meaningful with respect to the stress-free, or undeformed, state. When the reference lattice $\mathbf{g_1}$ and $\mathbf{g_2}$ used to measure the deformation in GPA coincide with this undeformed lattice such as the substrate, the deformation is same as the strain. For the case in which $\mathbf{g_1}$ and $\mathbf{g_2}$ are not substrate lattice vectors, the deformation is not the same as the strain. In the presence of compositional variations which change the shape of the unit cell, the undeformed state is not the same everywhere. Mixtures of strain and compositional variations are the most difficult cases to analyze [20-21].

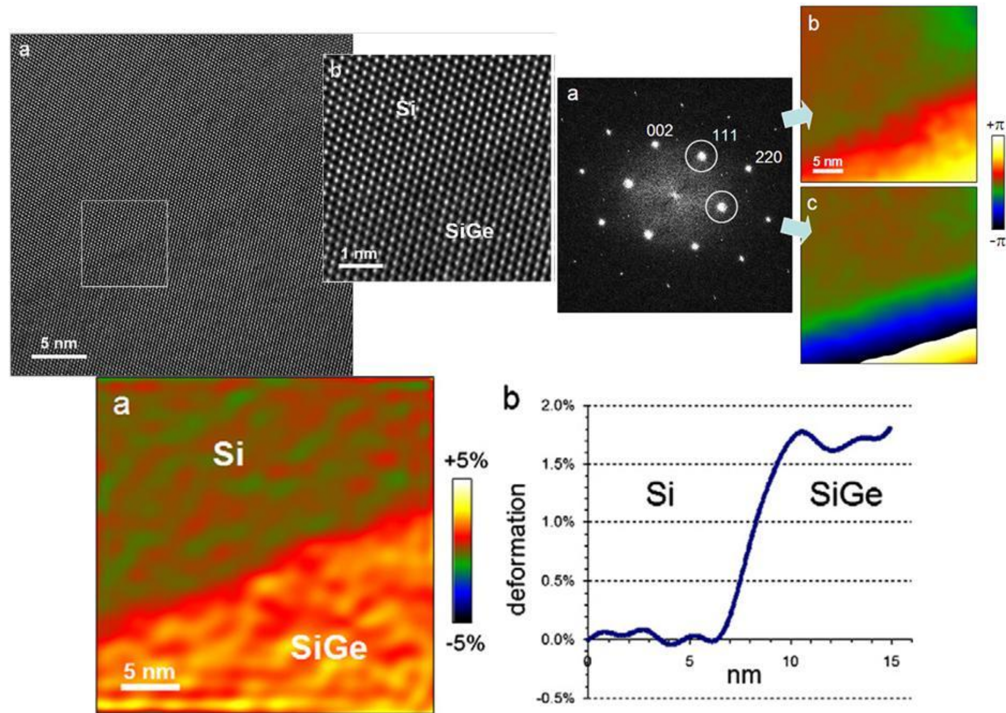

Figure 2.3: Left top is HRTEM of interface region between $Si_{0.7}Ge_{0.3}$ and Si substrate in [1-1 0] orientation. Right top show GPA analysis with Fourier transform of the HRTEM image and spots analyzed 111 and 11-1 circled and geometric phase of (111) lattice fringes and geometric phase of (11-1) lattice fringes. Bottom image shows deformation map of interface region: with deformation perpendicular to interface plane, e_{yy}, with respect to Si lattice the line profile averaged along 20 nm of interface. The average deformation in SiGe layer is calculated to be 1.7 ± 0.1%. [24]

In this dissertation research, GPA analyses has been done using a Digital Micrograph plugin FRWRtools developed by C. T. Koch [22-23], which is based on the original work of Hytch [20]. Figure 2.3 is an example of the application of GPA to find the deformation field across a SiGe/Si interface [24].

2.5 Scanning Transmission Electron Microscopy (STEM)

In the STEM operating mode, a convergent beam of electrons is focused and scanned across the specimen. The transmitted electrons scattered at different angles are then collected by detectors to form an image or spectrum. In general, the STEM unit consists of an electron source, several lenses to focus these electrons into a small probe, a scanning unit to scan this probe across the sample and detectors that collect signals after the electrons have interacted with the specimen [25-26]. In the STEM, scanning of the beam is accomplished by using two pairs of scanning coils located between the condenser lens and the objective pole piece. The scanning coils also help to keep the beam parallel to the optic axis while it is scanned across the specimen. The probe in a modern instrument can be about the size of an atom or even smaller, although the relevant interaction volumes may be much larger. Typically, very high brightness electron sources are needed to get high currents into a given size probe. The total current in the probe will ultimately determine the image acquisition time and the signal-to-noise ratio. Figure 2.4 shows a schematic of a STEM instrument [25-26].

In STEM imaging, serial recording is done instead of parallel recording, which is the case for TEM imaging. The STEM signal generated at each point on the specimen is detected, amplified, and the proportional signal is displayed at an equivalent point on the

monitor. An image is formed by recording the signal of interest as a function of probe position. The image therefore relates to the part of the sample that the probe interacts with at each position.

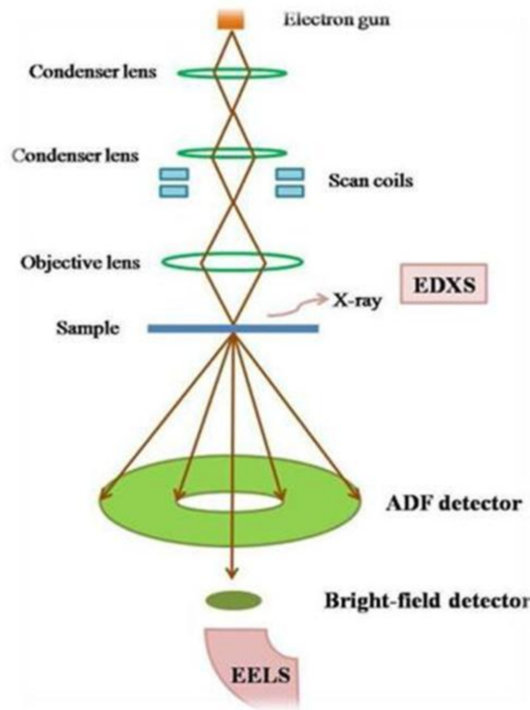

Figure 2.4: Schematic construction of a STEM [25]

Two types of STEM images can be obtained depending on whether the signal includes the direct beam or only scattered electrons. If the on-axis direct beam is detected, it is called bright-field (BF) STEM imaging. The BF detector collects electrons that have undergone relatively small angles of scattering including principally undiffracted, Bragg diffracted and inelastically scattered electrons. The BF STEM image is the coherent addition of purely elastically scattered electrons, the same as in BF TEM. Since TEM images are recorded in parallel, this mode is more efficient compared to STEM imaging in which the points are recorded serially. The STEM mode has the

advantage that a variety of different signals such as annular-dark-field (ADF), BF, energy-dispersive x-ray spectroscopy (EDX), and electron-energy-loss spectroscopy (EELS) can be collected simultaneously [27-28].

High-angle annular-dark-field (HAADF) images are obtained from the integration of incoherently scattered electrons at relatively high angles (larger than ~50 mrad) using the ADF detector. Since HAADF images result from incoherently scattered electrons, the lack of interference terms makes them directly interpretable. The incoherency in the high angle-scattered electrons is the effect of Thermal Diffuse Scattering (TDS) or phonon scattering, in which finite temperatures cause thermal motion of atoms. The low-angle scattering is dominated by elastic scattering, while the high-angle scattering is dominated by TDS [26]. The HAADF image contrast is insensitive to diffraction and phase contrast effects but is sensitive to the projected atomic number, because at high scattering angles, the atomic scattering factor is approximately given as: $f(r) = \frac{e}{16\,\pi^2 \varepsilon_0} \frac{Z}{r^2}$ [26]. Hence, the HAADF image contrast is strongly correlated to the atomic number Z of the specimen and the thickness, thus providing direct identification of atomic structure at heterostructure interfaces, based on atomic number. HAADF imaging, often referred to as Z-contrast imaging, relies on Rutherford scattering ($I \sim f(r)^2 \sim Z^2$). In practice, the image intensity can be expressed in the form $I \sim Z^{\alpha}$, where α is usually in the range between 1.6 and 1.9 depending on the geometry of ADF detectors, in particular, the inner and outer ADF detection angles [25-27].

The `Ronchigram' or `shadow image' taken with a slightly defocused probe is one of the most useful ways for characterizing and optimizing the electron probe shape. For a

typical Ronchigram from an amorphous region of sample, taken at slight underfocus, radial circles of infinite magnification are visible. These correspond to the angles at which defocus and spherical aberration effectively cancel and are characteristic of Ronchigrams from a round, probe-forming condenser lens. Axial astigmatism can be accurately corrected by exciting the condenser stigmator coils so that these Ronchigram features are circularly symmetric. As the beam is focused, the central region of the Ronchigram has minimum contrast and highest magnification. Assuming voltage centering is correct, the coma-free axis is clearly defined by this central position of the Ronchigram. All alignment and positioning of detectors, apertures, and also sample tilt can be performed with respect to this central spot [26].

Qualitative chemical information at atomic resolution can be obtained in STEM by using EDX or EELS. The EDX technique makes use of X-rays generated by electronic excitations in the sample to provide information about elemental distribution. An incident electron beam ionizes the atom by removing one or more of the bound electrons leaving the atom in an excited state. In the process of relaxation, the primary electron generates x-rays (along with Auger electrons) which are detected by the EDX detectors. This characteristic X-ray energy is unique to the specific atom and can be used to identify the elements present in the sample [29-30].

In addition, transmitted electrons that have lost measurable amounts of energy when passing through the sample are analyzed using the technique of EELS in order to extract further information about local variations in sample composition. When the incident electron beam is transmitted through the sample, some of the incident electrons

transfer energy to the sample, and a spectrometer can be used to record the energy lost by the primary electrons. A typical EELS spectrum consists of two regions; the low-energy losses are bulk excitations (e.g. valence-electron excitations, plasmons, etc.) that depend on the dielectric properties of the sample, and a core-loss region, in which an inner-shell electron in the sample is excited from an occupied state to an unoccupied state above the Fermi level. The final state depends upon the band structure of the sample. Thus, the EELS spectrum contains information on the elemental composition of the sample and its oxidation state, and it also probes the local electronic structure [29-30].

2.6 TEM Sample preparation

During this dissertation research, different thin-film/substrate combinations were studied. Since almost every sample was different, and since every material had unique mechanical and physical properties, sample preparation was far from universal. The following variables had to be optimized for each sample to get the best possible TEM sample: ion-gun modulation, rotational speed, ion-beam energy, angle of ion incidence, duration of ion milling, sample temperature during ion milling, amount of dimple polishing, final sample thickness before dimple polishing, grit size of polishing papers, differences in the rate of material removal during ion milling, and the amount of polishing time. Since oxides are in general, hard and brittle materials, the mechanical and dimple polishing procedures often proved to be quite different from those used for semiconductor materials.

2.6.1 Conventional Mechanical Method of Sample Preparation

For cross-sectional TEM observation, samples were cut into slabs with sizes of about 2.5 mm × 1.5 mm using a diamond wafer blade, and the two pieces were then glued together using M-bond glue, with epitaxial film layers placed face-to-face. Additional dummy samples were often glued on sides for mechanical support. Mechanical polishing was done successively using 30 μm, 9 μm, 3 μm, 1 μm and 0.1 μm diamond lapping films. Once scratch-free mirror-finish was obtained on the first side, second side was polished down to a total thickness of ~100 micron. The sample was then dimple-polished using a cloth wheel, typically reducing the sample thicknesses to ~25 μm. Since the removal rate for oxides materials was extremely low, the dimple polishing often took a very long time. For softer film/hard substrate combination, dimpling was usually stopped at a sample thickness of about 40μm to protect the film. The samples were then glued to copper grids suitable for the TEM sample holder. Finally, the specimens were thinned by argon ion-milling, using the Gatan Model 691 precision-ion-polishing system (PIPS) operated at energy of 3.5~4.0 keV until perforation was obtained. This thinning was then followed by low-energy ion-milling to remove ion damage caused by milling at high ion energies. Differences in the rate of material removal occurred during ion milling. A liquid-nitrogen-temperature cooling stage was used for some specimens to minimize any thermal or ion-beam damage [31, 32].

For plan-view TEM observation, samples were cut into slabs with sizes of about 2.5 mm × 2.5 mm using a diamond wafer blade. Mechanical polishing using 30 μm, 9 μm, 3 μm, 1 μm and 0.1 μm diamond lapping films, and dimpling using copper and cloth

wheels, were applied to thin specimens from the substrate side only down to ~10-μm thickness. The specimens were glued to copper girds and finally thinned from the backside only using argon ion-milling at low energy, off-mode of Gatan Mode 691 PIPS, until a small perforation appeared. The liquid-nitrogen-temperature cooling stage was again used during ion-milling to minimize any thermal or ion-beam damage. Every film/substrate combination demanded a slightly modified recipe [31-32].

2.6.2 Focused Ion Beam Sample Preparation

The Focused Ion Beam (FIB) technique was also tried for TEM cross-sectional sample preparation for spinel-spinel specimens but without much success. Most FIB instruments nowadays combine the scanning electron microscope (SEM) and FIB columns, as in DualBeam model of FEI Nova 200 FIB. The FIB system uses a Ga^+ ion beam which is rastered over the sample surface in a similar way to the electron beam in an SEM. The Ga^+ ions mill the sample away while the generated secondary electrons are collected to form an image of the sample surface. The major advantages of FIB over conventional TEM specimen preparation methods are that samples can be extracted from specific areas, and larger uniform thin areas can be obtained. For oxide-oxide specimens, Ga+ ion-beam-induced damage such as amorphization and local chemistry change was not much of an issue. To minimize FIB damage, a platinum protection layer was first deposited over the area of interest to protect the film. Our oxide samples, being very resistive, often became hot during focused ion milling. Due to excessive heat, the Pt layer disintegrated during FIB processing and could not protect the oxide thin films [33].

References

1. D. W. Williams & C. B. Carter, Transmission Electron Microscopy. New York: Springer(1996).

2. A. I Kirkland and J. L Hutchison, Nanocharacterisation, RSC Publishing 2007, Chapter 1, 1-27.

3. D. J Smith, Rep. Prog. Phys. 60 (1997) 1513–1580.

4. D.J. Smith, Adv. Opt. Electron Microsc., 1988, 11, 1.

5. M.A. O’Keefe, Ultramicroscopy, 1992, 47, 282.

6. W. Coene, G. Janssen, M. Op de Beeck and D. van Dyck, Phys. Rev. Lett., 1992, 69, 3743.

7. A. Thust and K. Urban, Ultramicroscopy, 1992, 45, 23.

8. D. J. Smith, Ultramicroscopy 108 (2008) 159–166.

9. M.A. O’Keefe, U. Dahmen and C.J.D. Hetherington, Mater. Res. Soc. Symp. Proc., 1990, 159, 453.

10. J. M. Cowley, Diffraction Physics, Elsevier Science B.V., Amsterdam, 1995.

11. E. Kirkland, Advanced Computing in Electron Microscopy, Second Edition, Springer 2010.

12. S. Thoma and H. Cerva, Ultramicroscopy 38 (1991) 265-289.

13. R. W. Glaisher and A. E. C. Spargo, Ultramicroscopy 27 (1989) 131-150.

14. L. Reimer, Transmission Electron Microscopy, Springer 4th Edition, (1997).

15. J. M. Cowley and A. F. Moodie, Acta. Cryst. (1957) 10, 609–619.

16. P. Goodman and A. F. Moodie, Acta. Cryst. A (1974) 30, 280–290.

17. K. Ishizuka and N. Uyeda, Acta Cryst. A33 (1977) 740-748.

18. D. Knauss and W. Mader, Ultramicroscopy 37 (1991) 247-262.

19. P.A. Stadelmann, Ultramicroscopy, 1987, 21, 131.

20. M. Hytch, F. Snoeck, and R. Kilaas, Ultramicroscopy 74 (1998) 131-146.

21. F. Hue, M. Hytch, H. Bender, F. Houdellier, and A. Claverie, Phys. Rev. Lett. 100, 156602 (2008).

22. C.T. Koch, V.B. Ozdol and P.A. van Aken, Appl. Phys. Lett. 96 (2010) 091901.

23. V. B. Ozdol, D. Tyutyunnikov, P. A. van Aken and C. T. Koch, Cryst. Res. Technol. 49 (2014) 38-42

24. M.J. Hytch, F. Houdellier, Microelectronic Engineering 84 (2007) 460–463.

25. E.M. James, N.D. Browning, Ultramicroscopy 78 (1999) 125-139.

26. P. D. Nellist and S. J. Pennycook, Advances in Imaging and Electron Physics, Vol 113 (2000) 147-202.

27. D. O. Klenov and S. Stemmer, Ultramicroscopy 106 (2006) 889–901.

28. S. J. Pennycook, M. Varela, A. R. Lupini, M. P. Oxley and M. F. Chisholm, J. Electron Microsc 58(3): 87–97 (2009).

29. S. J. Pennycook and C. Colliex, MRS Bulletin, Vol. 37, JAN 2012, 13-18.

30. W. Sigle, Annu. Rev. Mater. Res., (2005) 35, 239-314.

31. J.C. Bravman and R. Sinclair, J. Electron. Microsc. Technol. (1984) 1, 53.

32. S.B. Newcomb, C.B. Boothroyd and W.M. Stobbs, J. Microsc. (1985) 140, 195.

33. L. A. Giannuzzi, and F.A. Stevie, Micron (1999) 30, 197.

CHAPTER 3

EPITAXIAL THIN-FILMS OF DOPED-$SrTiO_3$ ON Si

3.1 Introduction

The perovskite $SrTiO_3$ (STO) is a highly promising material for applications in microelectronics because of its high charge-storage capacity, good insulating properties with high dielectric constant, excellent optical transparency in the visible region with a wide band gap of ~3.2 eV, and its chemical stability [1]. By processing in oxygen-reducing atmosphere, or by cation substitution at fairly low carrier density (~10^{18} cm $^{-3}$), STO can be made semiconducting [1-2]. The magnitude of the conductivity for STO and the type of majority carriers depend on the relative concentrations of defects. Reduction creates oxygen vacancies that act as effective donors [3]. The resulting *n*-type material can be modified by changing the oxygen partial pressure or by acceptor/donor doping. Conductivity is more accurately controlled by doping than oxygen-deficiency control [3]. At temperatures as low as 1K, STO exhibit superconductivity when doped, for example, with Nb, La, Ta or oxygen vacancies [3]. The ability to control conductivity in STO is important in the design of various electronic devices such as capacitors, metal-oxide-semiconductor field effect transistors (MOSFETs), thermistors and varistors [1]. In the case of MOSFETs, STO is becoming one of the preferred high-*k* dielectric candidates to replace SiO_2 as the gate insulator when its thickness is as small as a few atomic layers. Thus, the SiO_2 power consumption increase due to gate current leakage is overcome [1]. The high dielectric permittivity along with the low microwave losses makes STO the most attractive material for tunable microwave devices such as phase-shifters, filters,

oscillators, etc [2]. For any potential electronics applications, it is necessary to fabricate both *n*-type and *p*-type STO.

STO properties can be modified by doping STO at the cation positions. Heavy doping of STO with Nb or La turns STO into an *n*-type degenerate semiconductor and good thermoelectric materials with improved Seebeck coefficient and conductivity [4-5]. Through indium doping, STO becomes a *p*-type semiconductor [6] or a superconductor through introduction of oxygen vacancies [7]. Nb doped-STO is of technological interest as Nb-doped STO thin films can potentially be used as electrodes for metal/insulator/metal (M/I/M) and superconductor/normal metal/superconductor (S/N/S) junctions [4]. Polycrystalline Dy-doped STO thin films showed oxygen sensing characteristics at room temperature. The oxygen gas-sensing characteristics depended on the amount of Dy-doping, with 1.5% Dy-doping being most effective. The oxygen gas-sensing characteristics were closely related to leakage current characteristics of Dy-doped STO. The suppression of leakage current by Dy-doping suggests that Ti^{4+} is substituted by Dy^{3+}, and the Dy^{3+} acts as an acceptor. Further doping of Dy^{3+} increased the leakage current and lowered the oxygen gas sensitivity [8]. Resistive switching MIM structures, which can potentially be used for resistive random access memories, have been fabricated from Fe-doped [9] and Cr-doped [10] STO thin films grown on metallic single-crystal substrates (1% Nb-doped STO). It has been observed that interface traps, particularly oxygen deficiency, are crucial in determining space-charge region. Epitaxial Rh-doped STO thin-film photocatalysts have shown highly efficient hydrogen-producing characteristics [11]. High quality, optically transparent, Sb-doped STO thin films with

transmittances higher than 85% in the visible region have been grown on STO substrates [12]. The electrical conductivity of Sb-doped STO films changed from metallic to semiconductor to insulator as Sb doping is increased.

The crystal structure of STO has Ti^{4+} ions that are six-fold coordinated by O^{2-} ions, whereas each of the Sr^{2+} ions is surrounded by four TiO_6 octahedra. Therefore, each Sr^{2+} ion is coordinated by 12 O^{2-} ions. Within the TiO_6 octahedra, hybridization of the O-2p states with the Ti-3d states leads to pronounced covalent bonding, while Sr^{2+} and O^{2-} ions exhibit ionic bonding character. A distortion from cubic to lower symmetries occurs if the temperature is lowered or if a foreign cation/dopant is introduced into the lattice [3]. Distortions to the STO lattice are assigned to three main effects: size effects, deviations from the ideal composition and crystal-field effects, also known as Jahn-Teller effect. Usually, a combination of these factors is responsible for distortion of the STO crystal lattice [3].

The integration of functional perovskite oxides on silicon enables the possibility of achieving both improved performance in standard field-effect transistors, as well as obtaining hybrid electronic devices where multifuctionality of the oxide thin films can be directly coupled to the charge density of the semiconductor [14]. STO was originally envisioned as a replacement gate dielectric for scaled CMOS technology because of its very high dielectric constant. One major difficulty that has prevented this technology from being developed is the absence of a conduction-band offset between Si and STO, making STO unsuitable for use as a gate dielectric. Different routes have been proposed to increase the STO/Si conduction-band offset, including insertion of high-band-gap

offset buffer layers and modification of the interface oxygen stoichiometry. It is possible to modify the band structure of STO by systematically doping the Ti cations with different dopants [3]. The ability to modulate the band gap of a material without altering its desirable functional properties is crucial for fabricating heterojunctions for device applications.

3.2 Al-doped $SrTiO_3$ for Oxide Electronics

Independent work by our collaborators at the University of Texas-Austin using Density Functional Theory, Ellipsometry and XPS has revealed the effects of the substitution of Ti with Al on the band gap of perovskite oxide STO [14]. The band-gap of Al-doped STO is increased by approximately 0.3 eV compared with undoped STO. The Al dopant effectively behaves like a Ti vacancy in the energy range of the valence and conduction bands, and its main effect on the electronic structure is to block Ti-Ti hopping, which reduces the conduction band width and therefore increases the band gap. The higher the Al%, then the larger is the resulting increase in the band gap [14].

The Al-doped STO film studied in this work was deposited directly on an Si(001) substrate using Molecular Beam Epitaxy. Sr, Ti, and Al were all deposited using effusion cells operated at approximately 425°C, 1780°C, and 1010°C, respectively, resulting in a growth rate of about 1 monolayer per minute. The film stoichiometry was controlled by shuttering the metal sources for the appropriate length of time during growth. The metal fluxes were calibrated using a quartz-crystal thickness monitor with feedback from *in situ* x-ray photoelectron spectroscopy (XPS) measurements of the film composition. During growth, the sample surfaces were monitored by reflection-high-energy electron

diffraction (RHEED) using an electron energy of 18 keV at a glancing angle of ∼3°. Growth on Si was performed at a substrate temperature of 500–550 °C under an oxygen partial pressure of 4–5 × 10^{-7} Torr. These particular growth conditions have previously been found to result in an SiO_x layer thickness of <1 nm for undoped STO, as measured by cross-section transmission electron microscopy [15]. For the growth of Al-doped STO, the Sr shutter was held constantly open while the Ti and Al shutters were opened alternately to achieve the desired Al doping concentration. The total growth rate was ∼4 Å per min. Prior to growth, the *n*-type Si substrates were degreased and then exposed for 15 min to UV/ozone. The native oxide was removed using Sr-assisted de-oxidation, followed by deposition of a half monolayer of Sr-Zintl template at 550°C [14].

3.2.1 Experimental Work

In this work, these Al doped-STO thin-films deposited on Si were studied using transmission electron microscopy to determine the film-substrate interface, and the crystalline quality, to monitor the Al distribution in STO, and to determine the electronic structure and effect of Al substitution on crystal-fields. The composition of sample was intended to be Si(001) / 1.5-nm STO / 8-nm 10% Al-doped STO / 8-nm 20% Al-doped STO / 6-nm 10% Al-doped Sr_2TiO_4. Cross-sectional TEM samples were prepared using conventional mechanical polishing and dimple grinding followed by precision ion milling at ~ 3.0 keV to achieve final thickness for electron transparency. The samples were studied using the JEOL JEM-2010F electron microscope operated at 200 keV with C_s = 0.5 mm, yielding the structural resolution of ~1.9 Å. High-angle annular-dark-field (HAADF) images were recorded with the microscope operated in STEM mode at 200

keV with probe size ~2 Å. The inner and outer angles of HAADF detector were ~45 mrad and ~170 mrad respectively. Energy-dispersive spectroscopy (EDS) spectrum was recorded with probe size ~5 Å. All samples were plasma-cleaned before TEM investigation to remove contamination and often required beam-shower to remove beam damage that occurred when using HAADF imaging in the STEM mode.

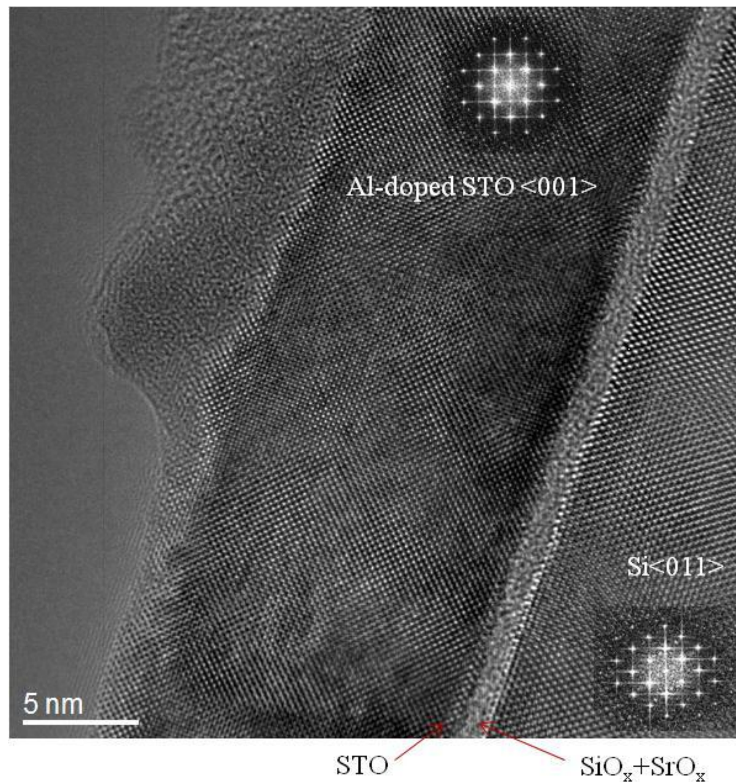

Figure 3.1: HRTEM image showing cross-section of Al-doped STO thin film grown on silicon. Insets are diffractograms from film and substrate.

Figures 3.1 and 3.2 show cross-sectional high resolution transmission electron microscopy (HRTEM) images. The micrographs show the excellent crystallinity of the Al-doped STO throughout the thin film. The clear presence of oxide phases of SiO_x+SrO_x with thickness of ~ 1 nm is apparent at the STO/Si interface. Even the sample with 20%

Al concentration shows excellent crystallinity. The HRTEM imaging also revealed the occasional presence of grain boundaries (not shown here) in the epitaxial STO film.

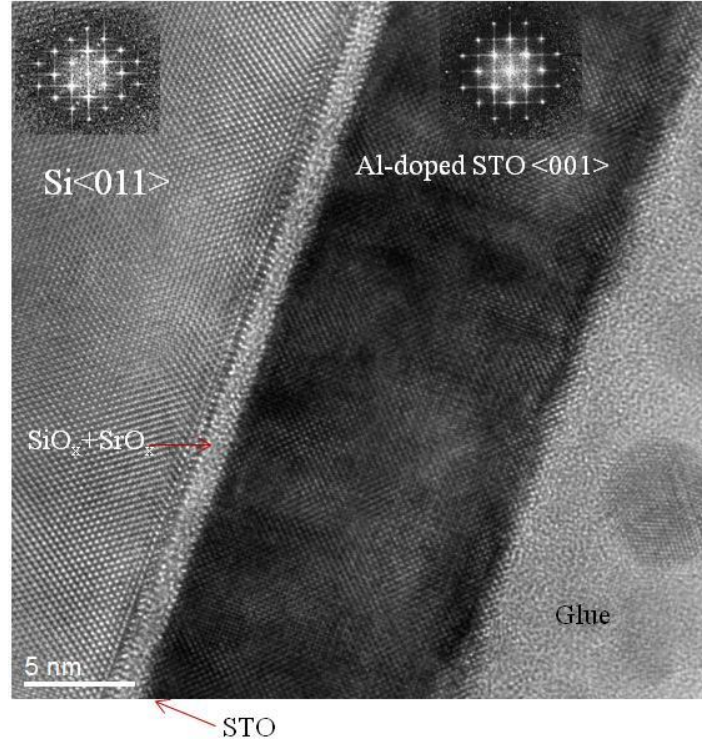

Figure 3.2: HRTEM image showing cross-section of Al-doped STO thin film grown on silicon. Insets are diffractograms from film and substrate.

Figures 3.3 and 3.4 are HAADF images of the Al-doped STO on Si. These HAADF images again show the very high quality defect-free crystal. Images taken at higher magnification are also shown. In HAADF imaging mode, the intensity of scattering scales with the atomic number Z as ~ $Z^{1.7}$ [15] so that brightest spots are located at columns of Sr atoms (large green spheres in atom models), and the less bright gray spots in between the bright spots are the Ti–O columns. Distinct dark amorphous region of SiO_x+SrO_x phase is present at the Si/STO interface. The interface between the 1.5-nm STO layer and the 10% Al-doped STO is not distinguishable.

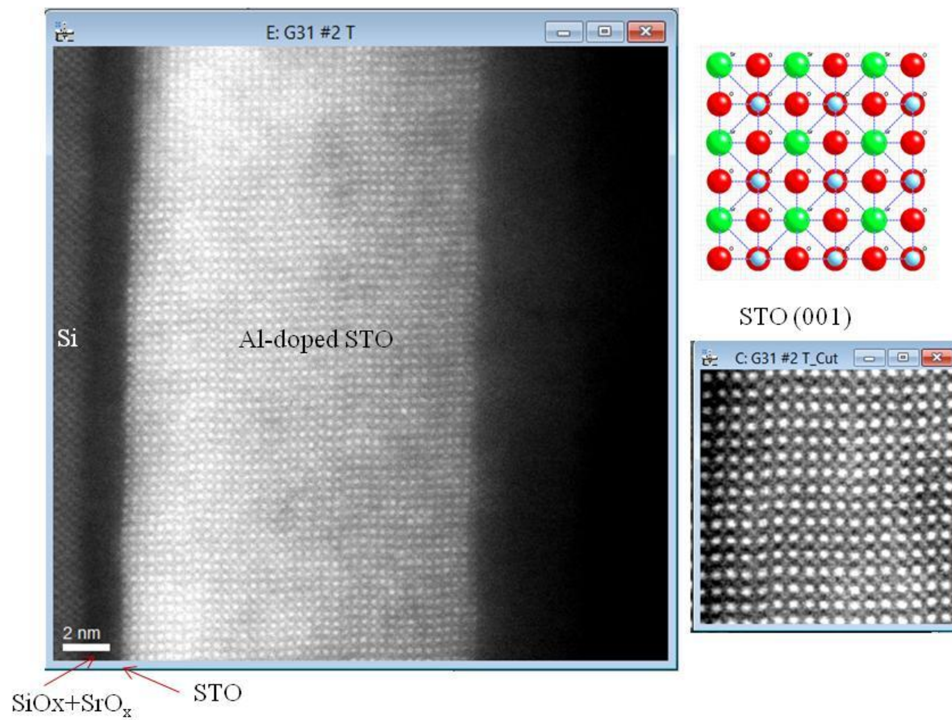

Figure 3.3 Cross-sectional HAADF image of Al-doped STO grown on silicon, enlarged view and atomic model of STO in (001) projection.

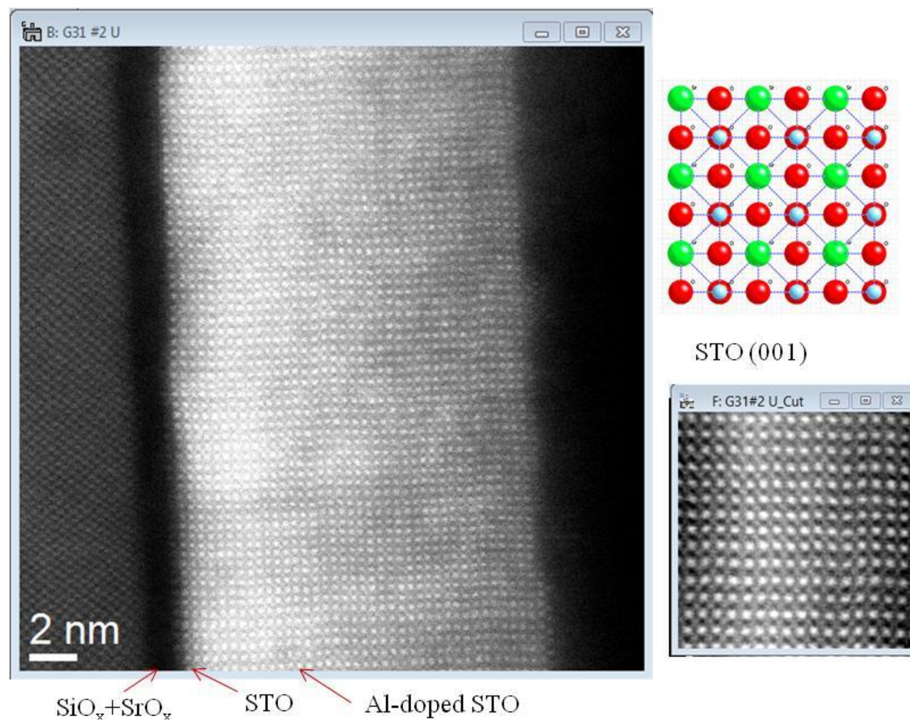

Figure 3.4 Cross-sectional HAADF image of Al-doped STO grown on silicon, enlarged view and atomic model of STO in (001) projection.

The chemical composition and Al distribution in the STO film were characterized by Energy-Dispersive X-ray Spectroscopy (EDS) and by Electron-Energy-Loss Spectroscopy (EELS) techniques. Line scans consisting of multiple spectra across a width of the sample were obtained and spectral images were recorded. Each spectrum was obtained for a dwell time of ~ 0.5 s and the spectra were ~ 5Å apart. Since the probe size used was ~ 5Å, each spectrum came from overlapped regions. Care was taken to ensure that the sample drift was minimal. The EDS and EELS spectral images were then processed using Digital Micrograph. Figure 3.5 show the raw data from elemental mapping of the sample using EDS. The data is noisy but the general trend of Al distribution across the sample is visible in the extracted and smoothened Al data shown in figure 3.6. Since the Al-doped thin films were deposited at ~ 500 - 550 ^{o}C, it is to be expected that Al will diffuse in the STO lattice. The Al distribution across STO / 10% Al-doped STO and 10% Al-doped STO / 20 % Al-doped STO interfaces was not sharp, as can be seen in figure 3.6.

In all the profiles, the origin on the *x* axis corresponds to the substrate-thin film interface. Thus, all scans are directed from the substrate-thin film interface across the thin film. From figure 3.6, the Al profiles in general roughly follow the desired doping distribution of Si/ STO (1.5 nm) / 10% Al doped-STO (~8 nm) / 20% Al doped-STO (~8 nm) / 10% Al-doped SrO-STO (~6 nm). The EDS profiles are not sharp step functions, possibly because of Al diffusion in the STO lattice at high deposition temperature and high interaction volume in the EDS technique, instrument limitation and random errors could also have contributed to the absence of sharp steps in the Al profile.

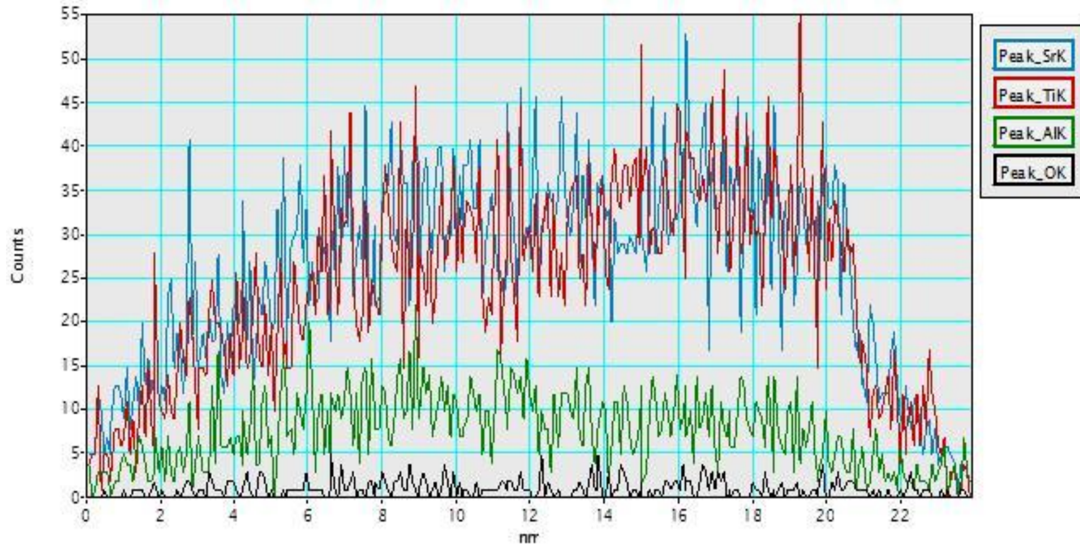

Figure 3.5: Elemental distribution across Al-doped STO sample.

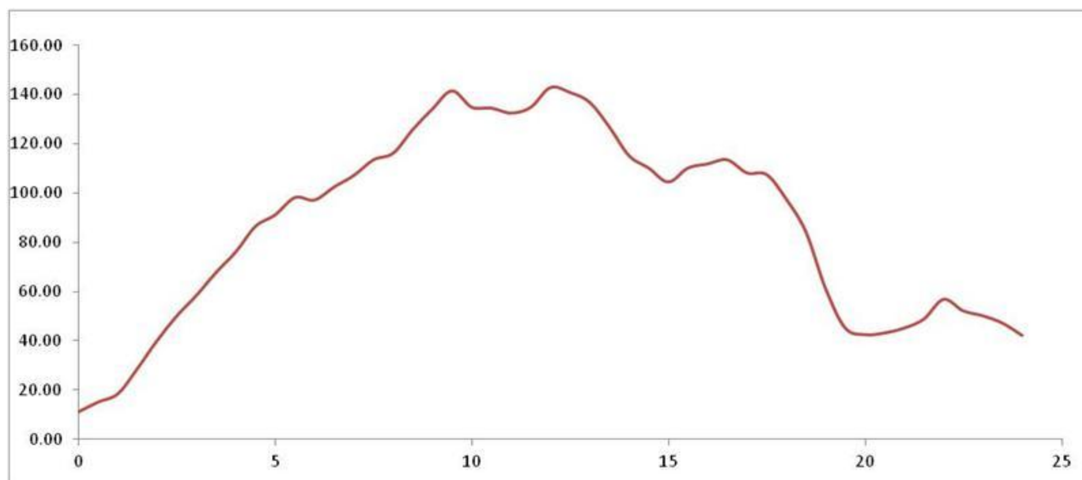

Figure 3.6 Al distribution across the Al-doped STO sample taken from figure 3.5

Elemental mapping was also done using EELS. Elemental profiles made using EELS tend to be less noisy than EDX mapping and have higher accuracy. The Al, Ti and O peaks were all observed in the EELS spectrum. Figure 3.7 show an example of the Ti and O distributions across the Al-doped STO cross-section. Figure 3.8 shows the Ti/O relative composition ratio for the same line scan.

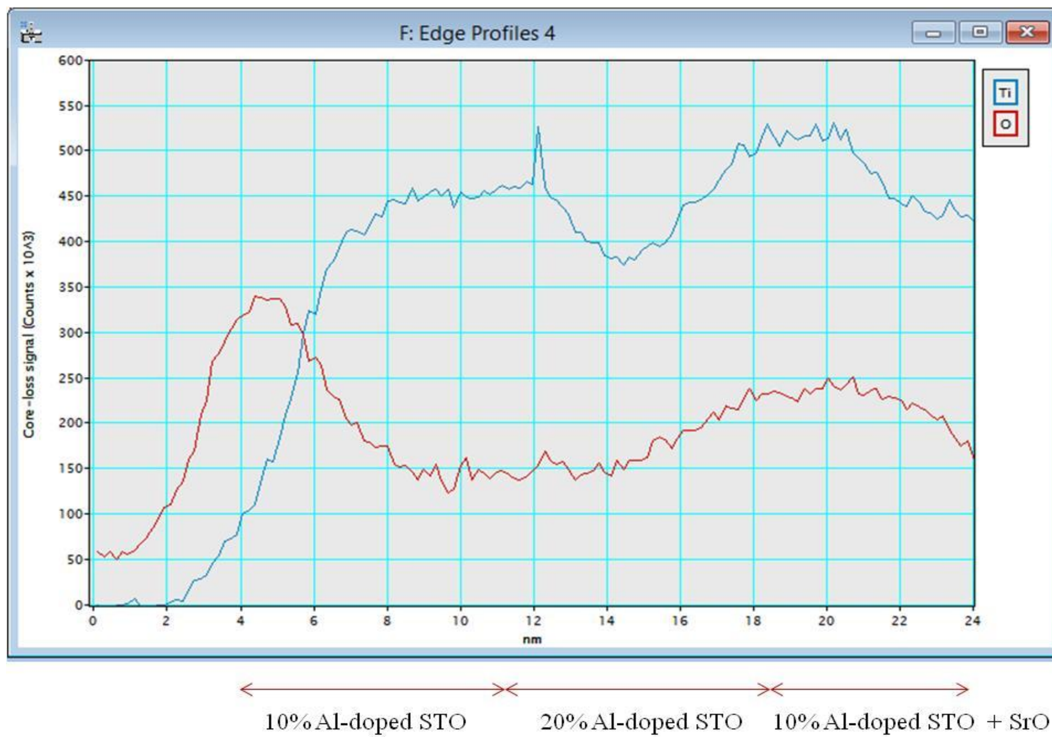

Figure 3.7 Ti and O distribution in Al-doped STO thin film

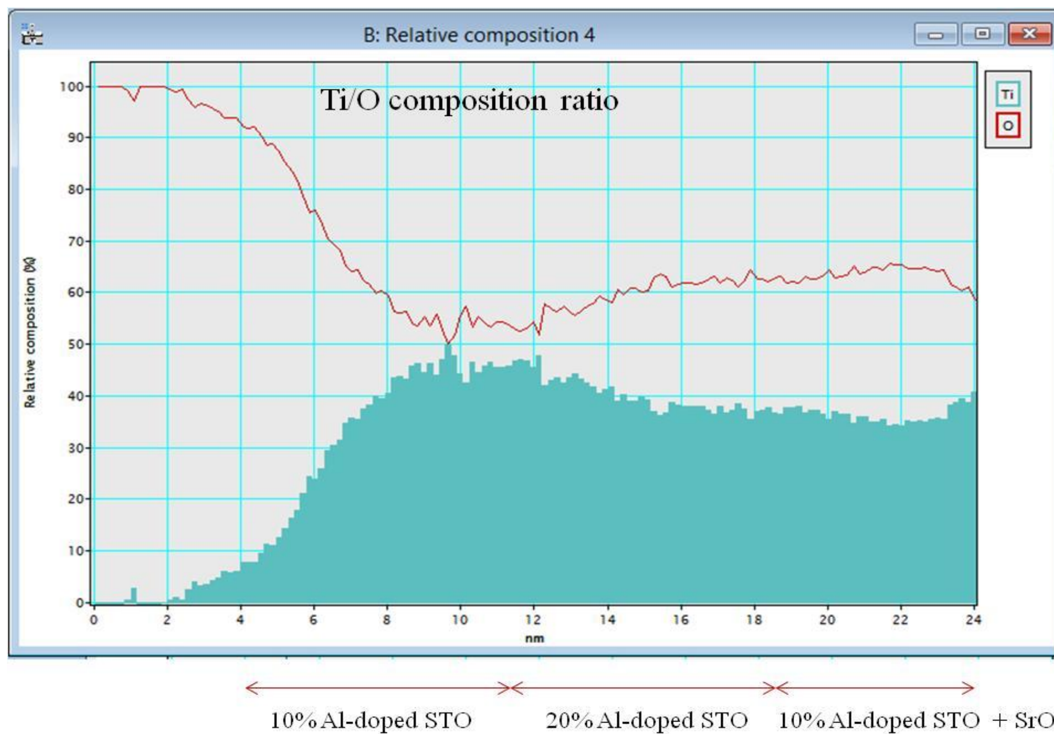

Figure 3.8 Relative composition ratio of Ti/O

The Ti/O ratio is a measure of the amount of Ti^{4+} converted into Ti^{3+}, which is associated with production of oxygen [16-17]. The middle dip at the top of the Ti curve in figure 3.7 corresponds to the 20% Al-doped STO layer in the middle of the film. The same trends were also seen in the EDS elemental profiles in figure 3.5 although the EDS data is noisier. The increase of Al doping corresponds to decrease in Ti % and rise in O vacancies to bring charge neutrality. This is evident from figure 3.8, where Ti is replaced by Al, and the oxygen vacancy level increased. The Ti % rises again in the last layer as the Al is reduced back to 10%.

3.2.2 Determining Electronic Structure

Al doping in STO strongly affects the STO electronic structure as well as the chemical structure and the surrounding environment [17]. Considering the fact that the ionic radii of Al^{+3} (~ 0.53Å) and Ti^{+4} (~ 0.60Å) are comparable, it can be anticipated that the doped Al partially or completely substitutes for Ti with some possibility of Al^{3+} going in interstitial sites. When Al substitutes for Ti, then corresponding oxygen vacancies are created for charge neutrality.

EELS, especially in the core-loss region, is a very powerful way to probe the electronic structure and to detect changes in the local chemical environment. The Ti-L_3 (456 eV) and Ti-L_2 (462) doublet and nearby O K (532) peaks are very susceptible to changes in chemistry, and have been used to detect changes in the amount of Ti and corresponding oxygen vacancies. As Al atoms substitute for Ti atoms, the shapes of the Ti L peaks and O K peaks should change as the doping percentage of Al in STO lattice

changes across the width of the film. Changes in the core-loss peak shapes corresponding to changes in the crystal symmetry are well established [16-18].

EELS line scans were recorded using GATAN Enfina EELS detector with the STEM probe (~ 5 Å) with dwell time ~ 0.5 s and entrance aperture of 2 mm. The EELS and EDS line-scan geometry is depicted in figure 3.9. For the electron probe in analytical mode, energy resolution of ~ 1.1 eV was obtained for the dispersion of 0.1 eV/pixel for the spectra. Line scans were processed using Digital Micrograph. An original EELS spectra line-scan corresponding to figure 3.9 consisted of ~80 spectra (alternatively referred as Series in this chapter). For practical reasons, only 40 equally-spaced spectra of Ti-L and the corresponding O-K fine edge structures were processed, and 30 are shown in figures 3.10 - 3.14. All the spectra are background-subtracted to get spectra normalized to the continuum interval 30 eV before the onset of the Ti-L or O-K edges. The fine structure of the Ti-L and O-K edges changed from thin film / substrate interface moving into the Al-doped STO.

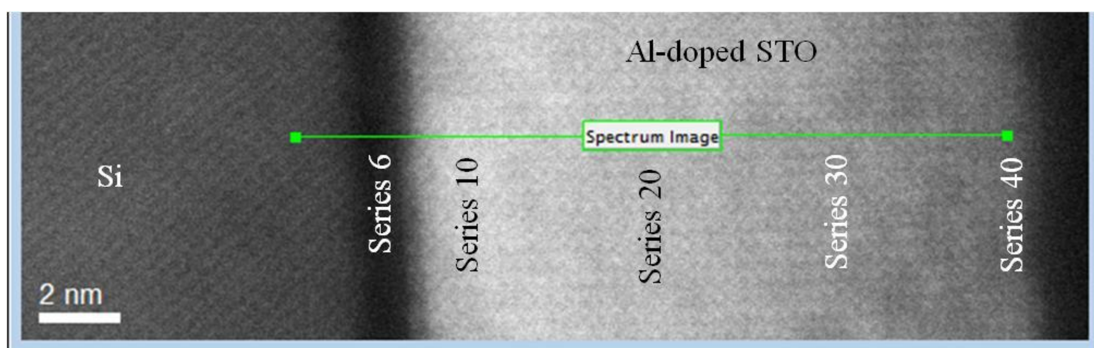

Figure 3.9 EELS and EDS line-scan geometry

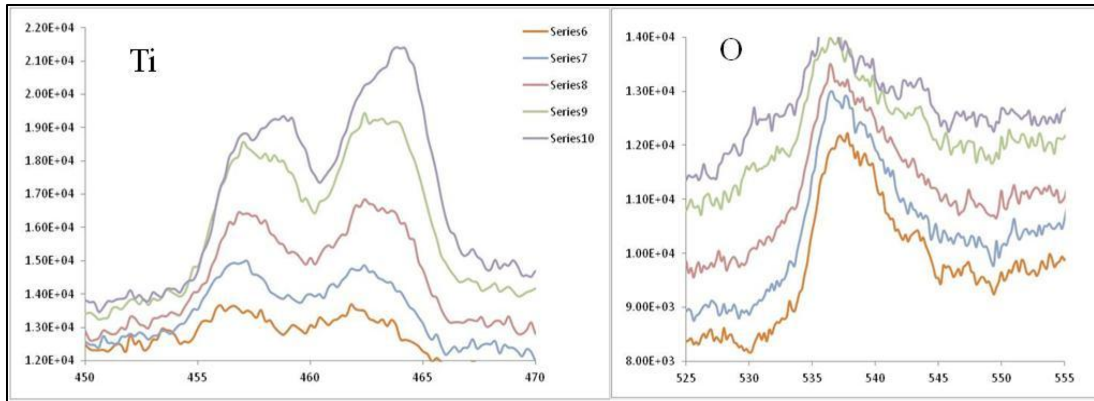

Figure 3.10 EELS spectra of Al-doped STO. The Ti-L and O-K fine edge structure change across the sample starting with series 6 at the Si-STO interface.

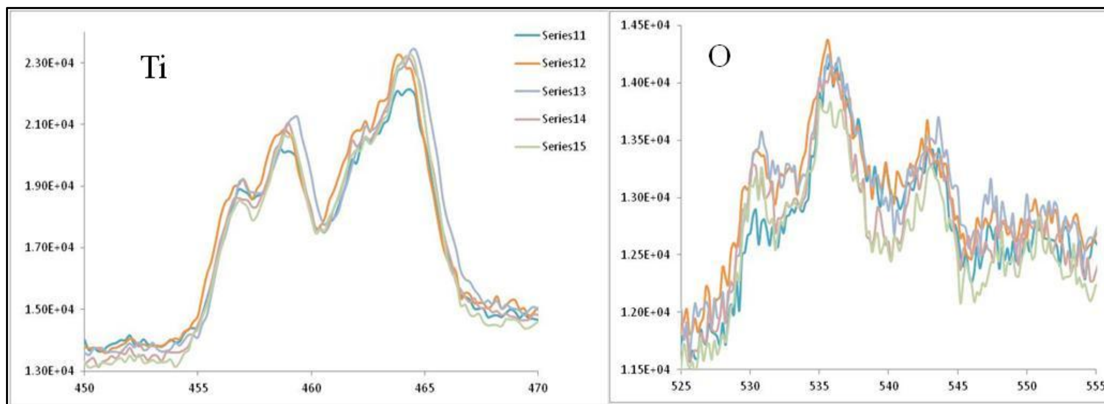

Figure 3.11 Ti-L and O-K fine edge structure evolve from amorphous SiOx + SrOx +TiOx phases at the interface (series 11) into Al-doped STO (series 15)

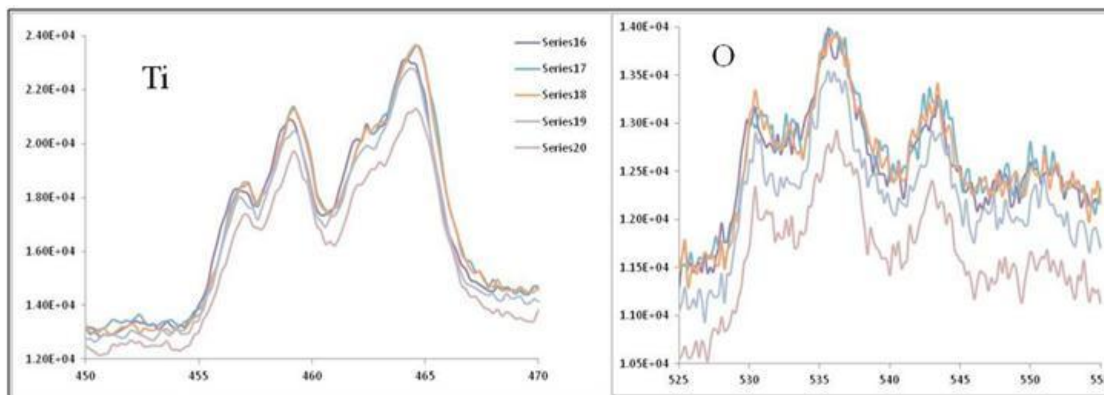

Figure 3.12 Ti-L and O-K fine edge structure in 10% Al-doped STO (from Series 16 to Series 20)

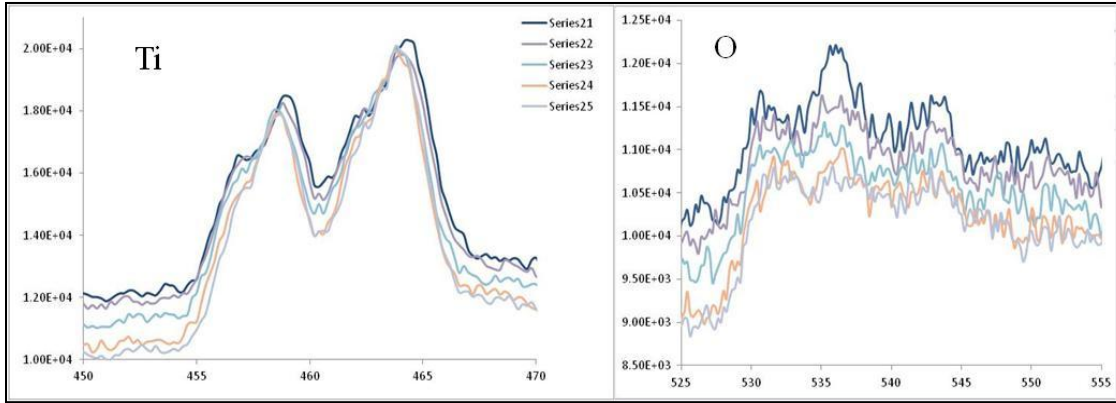

Figure 3.13 Ti-L and O-K fine edge structure in 20% Al-doped STO (Series 21 through Series 25)

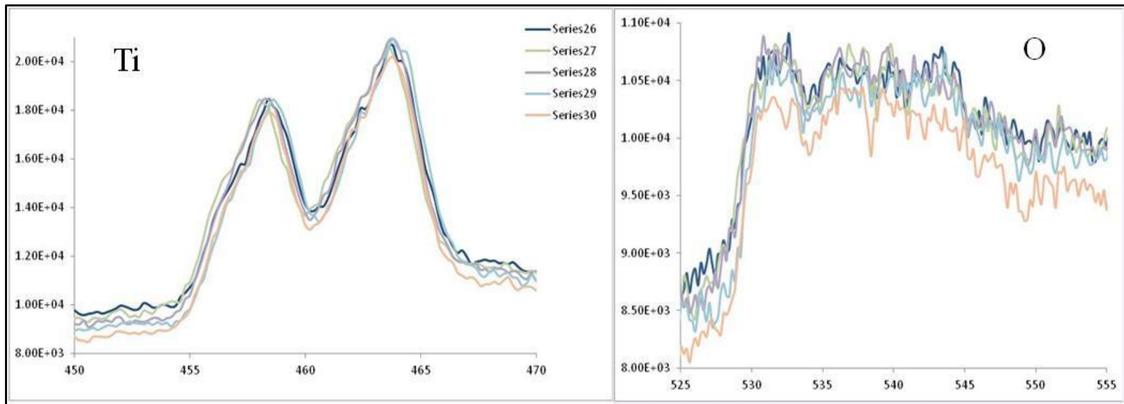

Figure 3.14 Ti-L and O-K fine edge structure evolve fromz 20% Al-doped STO moving into 10% Al-doped STO +SrO (series 26-30). The O-K fine edge structure starts damping out as % of O vacancies rises.

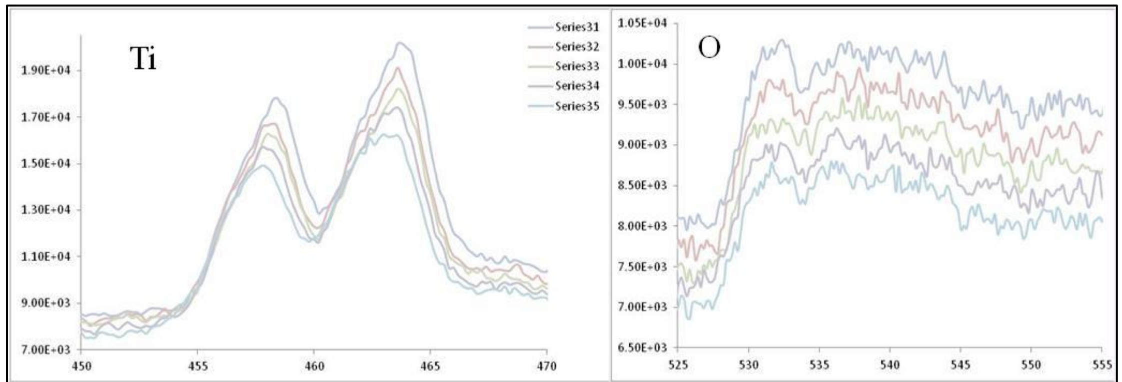

Figure 3.15 Ti-L and O-K fine edge structure evolving into10% Al-doped STO +SrO (series 31-35). Large number of oxygen vacancies are apparent as the O-K fine structure damps out completely and Ti-L fine structure disappears.

The top region of the thin film was disordered with O-K fine structure completely damping out because of very high concentration of O vacancies (series 30-35). Comparing this data with standard Ti-L and O-K fine edges, published by Muller et al [16] as shown in figure 4.16, it can be seen that Al doping changes both the Ti-L and O-K edge structure. Spectrum Series 6 starting at the STO / Si interface and Series 35 near the top edge of the thin film, across the differently Al-doped STO sample, directly show that the Ti-L and O-K fine edge structures change with the amount of Al-doping and corresponding amount of O vacancies.

The very high amount of O vacancies at the top edge of the thin film was also confirmed by XPS measurements [13]. DFT calculations have shown that Al doping in STO directly substitutes for Ti and creates oxygen vacancies in the vicinity of the Al atoms, tightly binding the Al atoms in the STO lattice [13]. Al-doped STO has less leakage current [13] compared to undoped STO, which further proves that O vacancies, which are responsible for leakage current, are tightly bound to Al. Reduction in leakage current can be interpreted as an increase in the band gap of Al-doped STO [13]. When Ti^{4+} ions are replaced by Al^{3+} ions, two O vacancies, which act as electron donors are created for charge balance. The central dip in the Ti profile of figure 3.7 corresponds to the rise in Al doping levels, also proving that Al indeed replaces Ti. From figure 3.8 it is evident that Ti/O composition ratio decreased as the Al doping levels increased.

EELS spectra provide very useful chemical and electronic information on the O and Ti states from the O-K (O 1s-2p) and Ti-L (Ti 2p-3d) core-edge structure. In general, ratios of integrated O-K and Ti-L edge intensities can directly give Ti/O ratio as shown in

figure 3.10. The Hartree-Slater cross sections were used for the EELS quantification [18]. However, absolute quantification is not practical for low oxygen vacancy concentrations, especially in ultrathin-film structures, such as these, considering the fact that the errors in background subtraction can easily be a few percent [16]. The shape of the EELS edge, which reflects the underlying electronic structure, becomes more reliable. As shown in figure 3.16, the O-K fine edge structure (which is proportional to the unoccupied O p-density of states) damps out with increasing oxygen vacancies. The Ti-L edge is also useful and shows distinctly different spectra for the $Ti_{3þ}$ and $Ti_{4þ}$ formal valences [16].

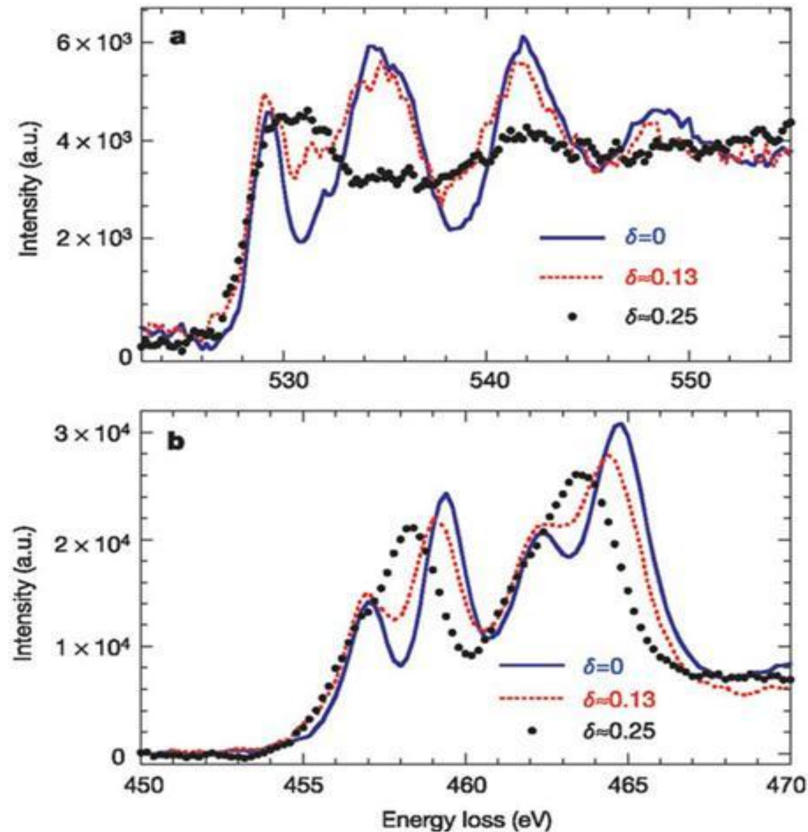

Figure 3.16 EELS for oxygen-deficient $SrTiO_{3-d}$, for d ~ 0, 0.13 and 0.25. a, The O-K edge fine structure is sensitive to O–O ordering, and damps out with increasing vacancy concentration b, The Ti-L edge shifts from 4þ to 3þ valence with increasing oxygen vacancies [16].

The Ti-L splits into Ti-L_3 and Ti- L_2 peaks due to spin-orbit interaction. The spin-orbit interaction can be explained in terms of hybridization of 4s and 3d orbitals. L_3 and L_2 further split each into t_{2g} and e_g. This finer splitting is due to Crystal fields also known as Jahn-Teller fields. In the O fine spectrum, peaks are named with letters a, b c and correspond to t_{2g}+e_g from Ti_{3d}-O_{2p} hybridization, Sr_{3d} and Ti_{4sp} hybridization respectively [19-20]. Oxygen peaks a, b and c in general represent the crystal quality. Ti_{3d} and O_{2p} form hybridized orbitals t_{2g} and e_g. Fine-edge structure details based on the hybridization theory shown in figure 3.17, are useful in explaining near edge structure.

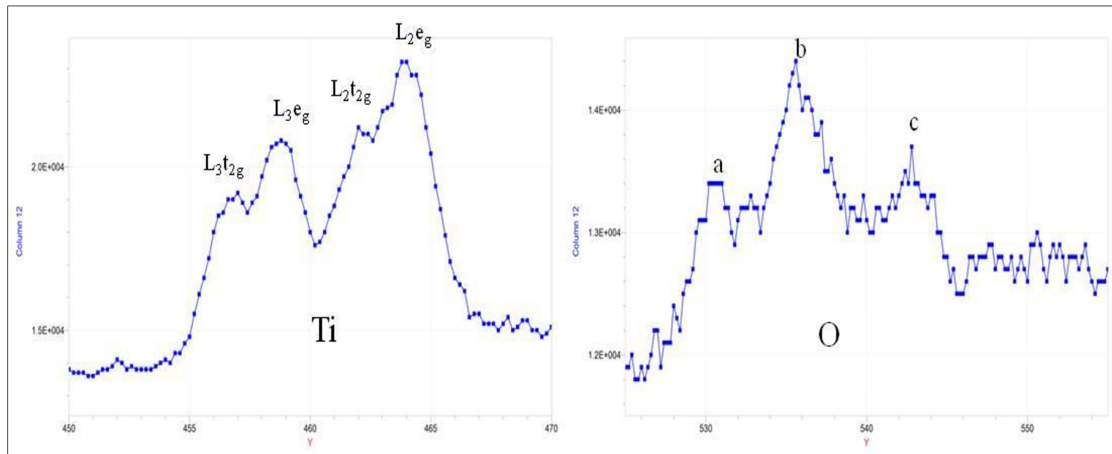

Figure 3.17 Experimental fine-edge structure details of Ti-L and O-K in STO

From oxygen fine spectra in figures 3.15 and 3.16, it is obvious that the uppermost area of sample (~ Series 28- Series 35) has excessive O vacancies. From Series 12 through Series 22, distinct a, b and c peaks are clearly visible in the O-L edge. This is an indication of good long-range order and moderate oxygen vacancies. The area of the sample between observation point Series 12 and 24 has best crystalline quality, as also shown by clear presence of both L_2 and L_3 doublets in Ti fine edge. Additional

evidence for the presence of oxygen vacancies is provided by a shift down in energy of the Ti L-edge and increase in the L_3/L_2 intensity ratio by few percent. Both are indicative of a lowering of the Ti valence to compensate for oxygen vacancies.

All the Ti-L and O-K fine edge structures are compared with standard Ti-L and O-K curves given by Muller et al [16], as shown in figure 3.16. These curves are for $SrTi_xO_{3-d}$, with d changing from 0 to 0.25. For these fine edge spectrum, d=0.13 corresponds to O vacancy of ~ 4 %. In order to verify and quantify change in the Crystal fields and downward shift in Ti-L peaks, the ELNES of Ti-L and O-K for series 10 through Series 36 were put together as shown in figure 3.18 and 3.20 respectively. Figure 3.19 and 3.20 show ELNES Ti-L and O-K data from ~10% Al-doped STO region of the sample (Series 13 through Series 18) put together with the ELNES Ti-L and O-K data from ~20% Al-doped STO region of the sample (Series 22 through Series 27). The crystal field affecting splitting of L_2 and L_3 Ti fine edges was observed to decrease in strength from Series 12 through Series 28. The Crystal field strength is given as (e_g-t_{2g}) ~ 2.4 eV for undoped-STO. The crystal field strength (shown by double-headed arrow) decreased from ~ 2.3 eV for Series 13 to ~1.7 eV for Series 28. Additional evidence for the presence of oxygen vacancies is provided by a down-shift (shown by arrow pointing towards left) in the Ti L-edge energy. Figure 4.18 clearly shows (using vertical lines) this shift of ~0.7 eV from Series 13 through series 28. This downward energy shift is indicative of lowering of the Ti valence from Ti^{4+} to Ti^{3+} and in our case from Ti^{4+} to Al^{3+} and associated creation of oxygen vacancies for charge balance.

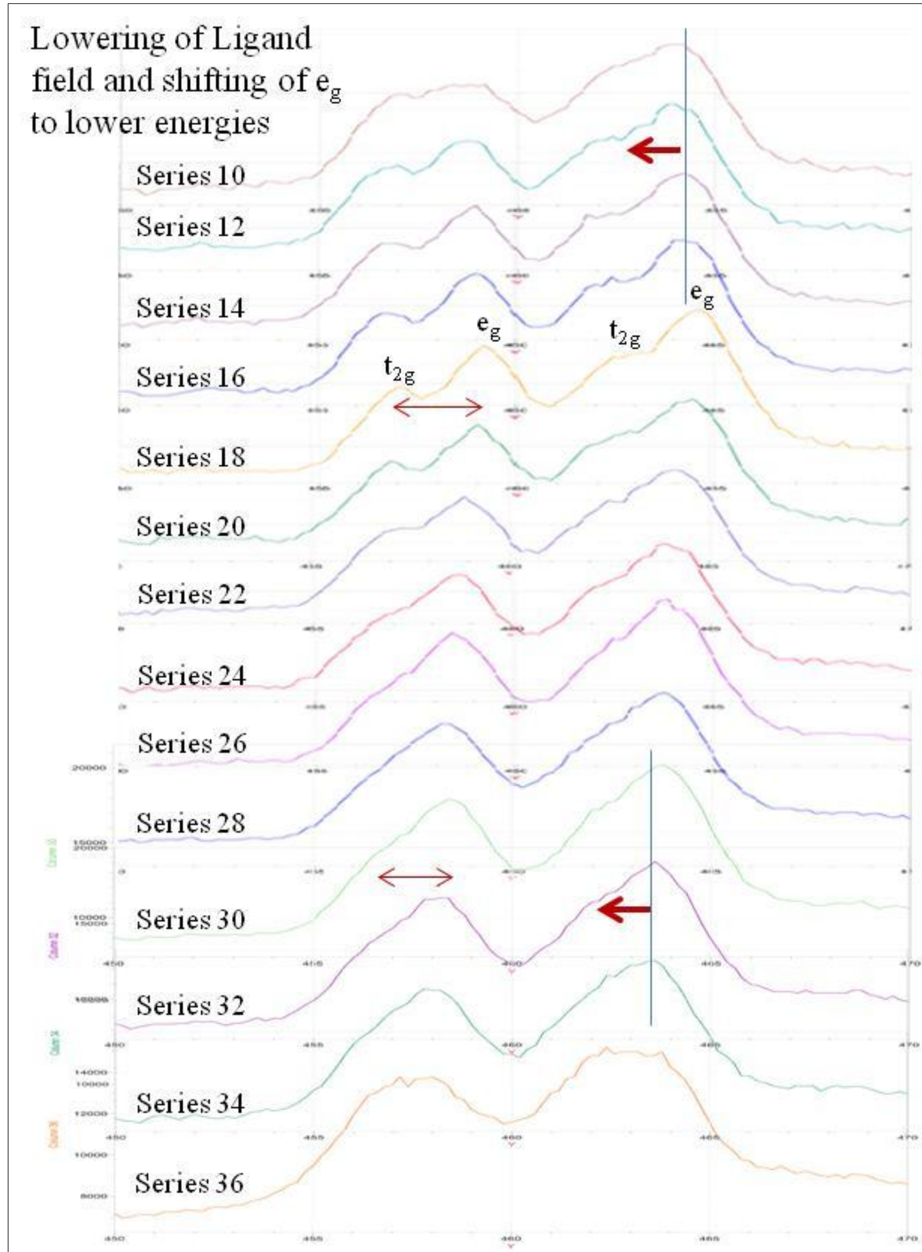

Figure 3.18 Ti-L near-edge spectra for Series 10 - Series 36

The L_3/L_2 intensity ratio was calculated by finding the area under the L_3 and L_2 peaks for Series 13 through Series 30 and the ratio values were unusually high ~0.9 and increased to ~0.94 for Series 30. These L_3/L_2 ratios were too high compared to 0.8 reported for undoped STO [20]. It is expected that the L_3/L_2 ratios would increase with

higher Al doping levels producing higher number of associated oxygen vacancies. Figure 3.19 shows a direct comparison of ~10% Al-doped STO (Series 13 through Series 16) with ~20% Al-doped STO (Series 22 - Series 27). Two distinct regions are clearly seen.

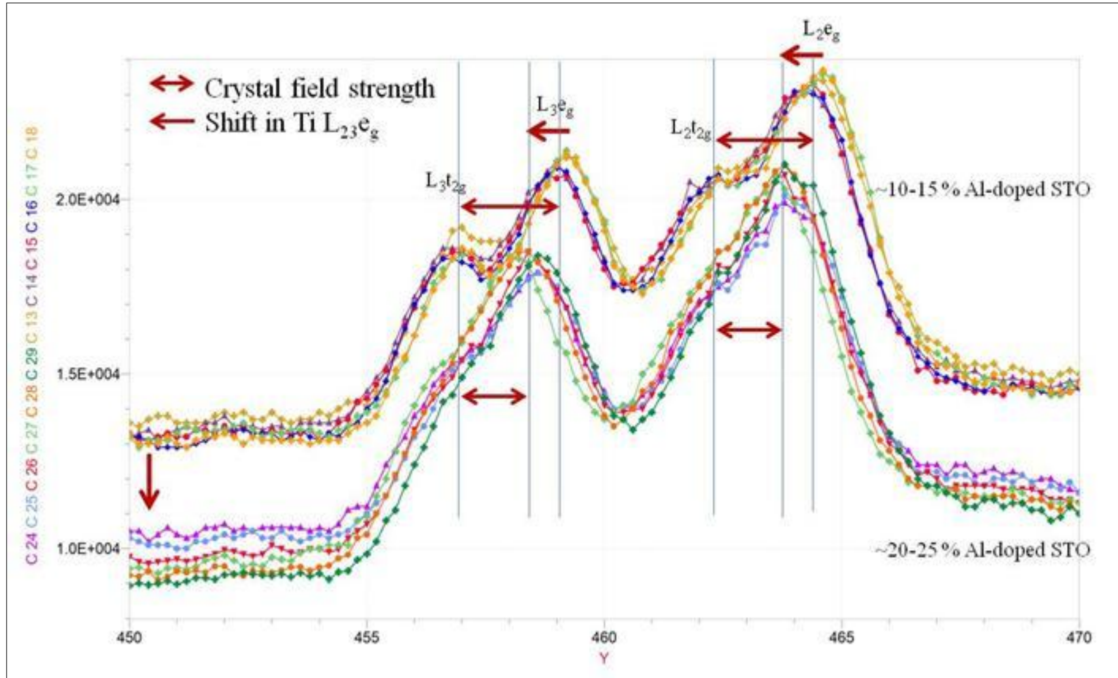

Figure 3.19 Ti-L ELNES from ~10 % Al-doped STO region (Series 13-Series 18) compared with spectra from ~20 % Al-doped STO region (Series 22 - Series 27)

From the oxygen fine-edge spectrum in figures 3.20 and 3.21 it is clear that the distinct a, b and c peaks in the O-K edge are clearly visible. This feature is the indication of good long-range order and moderate oxygen vacancies. Thus, the amount of O vacancies has increased from Series 12 through Series 30, but not to the level of affecting the overall crystallinity. Peaks a, b, and c eventually washed out from Series 28 through Series 36 with increased Al-doping and an increase in associated oxygen vacancies affecting crystallinity of STO lattice. From figure 3.21, two distinct regions corresponding to ~10% Al-doped STO and ~20% Al-doped STO are clearly visible.

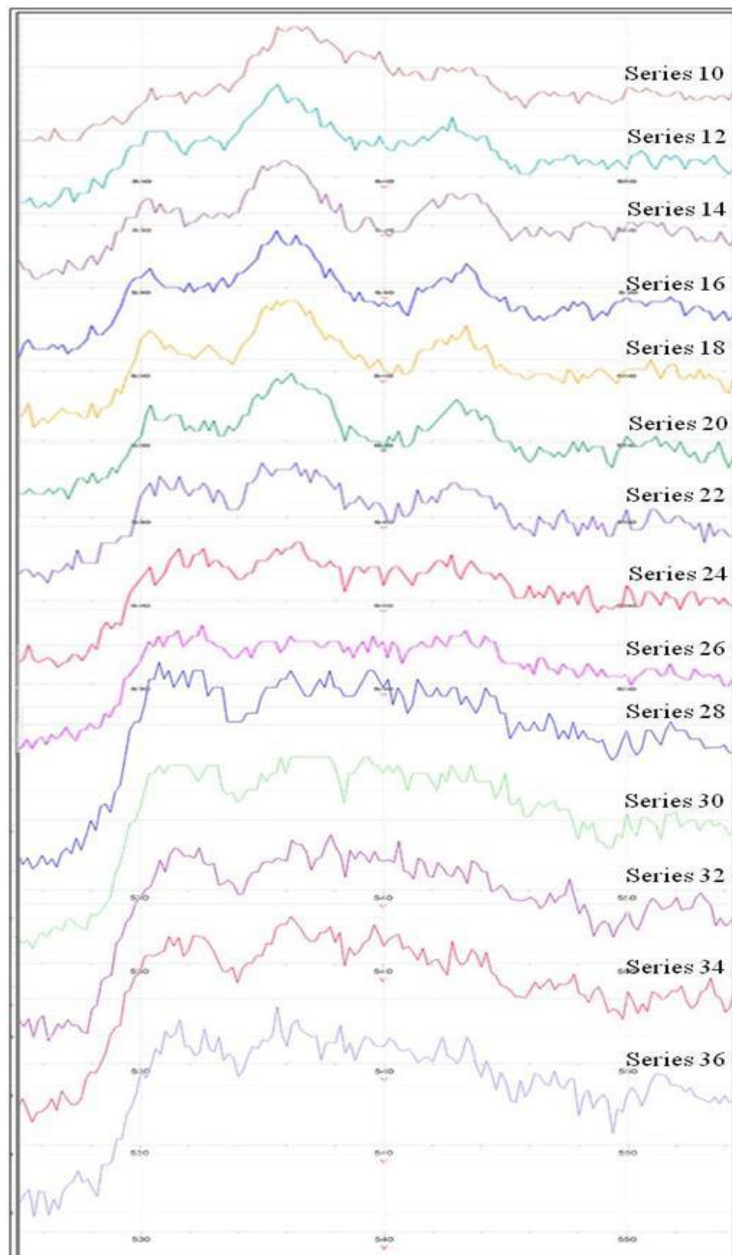

Figure 3.20 O-K near-edge spectra for Series 10 - Series 36

Overall peak intensity decreased from Series 12 through Series 36 also indicating increase in disorder in the STO lattice. Independent theoretical work by our collaborators at the University of Austin using DFT revealed that the Al^{3+} and associated oxygen vacancy are adjacent to each other because this configuration is energetically favored and

facilitates charge transfer between Al^{3+} and O vacancy [13]. From figures 4.1 through 4.4 it is clear that even at ~20% Al doping levels and corresponding oxygen vacancies, Al-doped STO has very high crystallinity.

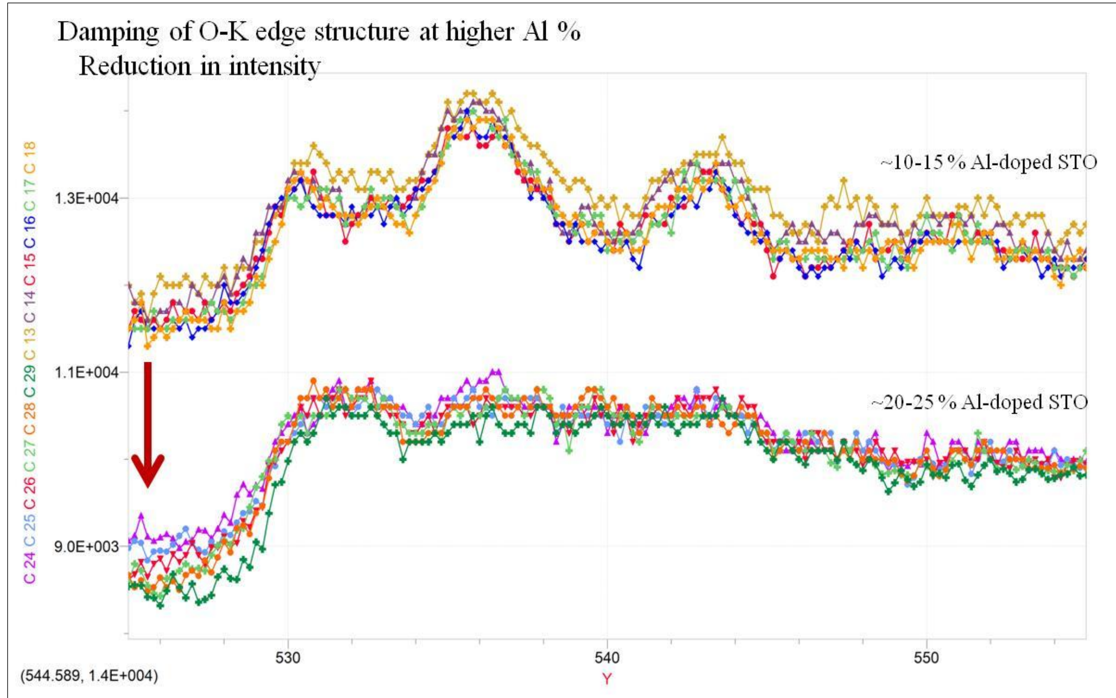

Figure 3.21 O-K ELNES from ~10 % Al-doped STO region (Series 13-Series 18) compared with spectra from ~20 % Al-doped STO region (Series 22 - Series 27)

3.3 Ferromagnetic Cobalt-Substituted $SrTiO_3$ Thin-films

The ability to manipulate both the spin and the charge in electronic materials could potentially lead to a new generation of advanced devices that have higher speed, higher integration density, higher reliability of data security, and lower energy consumption [21]. In one of the proposed spin-electron devices, the spin-field-effect transistor (spin-FET), it is very challenging to realize efficient injection of a spin-polarized current from a ferromagnetic metal contact into a semiconductor such as

silicon. A major challenge is the large density-of-states (DOS) mismatch between the metal and the semiconductor, resulting in a current injection efficiency of less than 1% [22]. Dilute magnetic semiconductors have been used as spin-injection contacts. These materials have high-quality interfaces with common semiconductors and do not have any conductivity mismatch problem. However, magnetic semiconductors have Curie temperatures well below room temperature, thus limiting their practical application [23].

Semiconducting oxides with room-temperature ferromagnetism are potentially very interesting for realizing future spin-based electronics devices such as spin-transistors, non-volatile semiconductor memory, or polarized optical emitters. Transition-metal oxides doped with magnetic ions such as Mn or Co has been found to exhibit room-temperature ferromagnetism [24-27]. The origin of the ferromagnetism in these transition-metal doped-oxides is not well understood. One major unanswered question is the distribution of the transition metal in the oxide lattice, in particular whether the transition metal is uniformly distributed in the oxide lattice or segregated in clusters, precipitates or secondary microscopic phases, which are responsible for the observed magnetic nature [27].

One issue limiting the potential application of most ferromagnetic-doped metal oxides is the difficulty of integrating them with a suitable semiconductor material. STO is one of a handful of perovskite oxides that can be epitaxially grown directly on silicon with a clean epitaxial interface [28], making it a candidate for the integration of a ferromagnetic oxide onto silicon. Bulk STO doped with Co generally does not show ferromagnetism except when a significant number of oxygen vacancies are present [29].

Thin films of insulating/semiconducting Co-doped STO exhibit ferromagnetism at very high doping levels (>~20 %) but not at low doping [30].

In this work, Co-substituted STO thin films were grown by MBE on a very thin STO (3uc) buffered-Si (001) pseudo-substrate at 550°C [31]. Growth of Co-doped STO was carried out using an MBE system equipped with effusion cells for Sr and Ti, an electron-beam evaporation source for Co, and molecular oxygen under a constant background oxygen partial pressure of 2×10^{-7} Torr. Sr, Ti and Co fluxes were measured using the quartz microbalance and RHEED, and adjusted to yield a growth rate of one monolayer per minute. The growth process was monitored *in situ* with RHEED to ensure that the film was crystalline and epitaxial. The nominal sample stoichiometry was $SrTi_{1-x}Co_xO_{3-y}$. The as-deposited films were observed to be crystalline and epitaxial and hence they were not annealed. The films were characterized *in situ* using XPS to determine stoichiometry, x-ray diffraction to determine lattice constants and crystalline quality, a magnetometer for magnetic measurements, and resistivity measurements [31]. The RHEED pattern for a sample with 10% Co substitution showed sharp streaks similar to that obtained for undoped STO on Si, indicative of high crystallinity. When the Co doping level was increased to 20–30 %, the streaks became broader, indicative of a greater degree of crystalline disorder but still well defined and single phase. At 40 % Co substitution, RHEED patterns showed the appearance of weak extra spots that indicated the presence of extraneous secondary phases. The XRD for compositions of 10-40% showed only peaks from the Si substrate and STO. A small extra peak was observed for 50 % Co composition, which is attributed to CoO precipitates [31].

3.3.1 Experimental Work

In this work, 25% and 30% Co-doped STO thin films deposited on Si were studied using transmission electron microscopy to determine the film-substrate interface, the crystalline quality of the thin films, and the Co distribution in STO lattice, as well as to determine the electronic structure, chemical environment and effect of Co substitution. The structure of the samples was intended to be Si(001) / 1.5 nm STO / 5-10 nm Co-doped STO. Cross-sectional TEM samples were prepared using conventional mechanical polishing and dimple grinding followed by precision ion milling at ~ 3.0 keV to achieve final thickness for electron transparency.

The samples were studied using the JEOL JEM 4000EX electron microscope operated at 400 keV with C_s = 1.0 mm yielding structural resolution of ~ 1.7 Å, and JEOL JEM-2010F electron microscope operated at 200 keV with C_s = 0.5 mm, yielding the structural resolution of ~1.9 Å. High-angle annular-dark-field (HAADF) images were recorded with the latter microscope operated in STEM mode at 200 keV with probe size ~2 Å. The inner and outer angles of the HAADF detector were ~45 mrad and ~170 mrad respectively. Energy-dispersive spectroscopy (EDS) spectra were recorded with probe size ~5 Å. All samples were plasma-cleaned before TEM investigation to remove contamination and often also required beam-shower. Figure 3.22 is a cross-sectional high-resolution transmission electron microscopy (HRTEM) image of a 5-nm 30 % cobalt-substituted film grown on 1.5-nm undoped STO/Si pseudo-substrate. The uniformity of the cobalt-substituted layer is evident. Figure 3.22 also shows that the initial undoped STO layer appears to have become amorphized and that a thin (~1.5 nm)

SiO_x layer has also formed at the STO/Si interface. The reason for the loss of crystallinity in the undoped STO layer is still unclear and may be due to reaction of the thin STO layer with Si-containing silicates and silicides [32]. Figure 3.23 is a HRTEM cross-section TEM image of a 10-nm 25 % Co-substituted STO grown on 1.5-nm STO-buffered Si pseudo-substrate. From diffractograms, figures 3.22 and 3.23, Si is <011> projected and the Co-doped film is <001> projected. From figure 3.22 and 3.23 the uniform crystallinity of the Co-substituted STO is evident, but both the images also shows amorphization of the undoped STO layer as well as a thin (~1.5 nm) SiO_2 layer. The level of amorphization of the undoped STO layer decreased in the later stages of the research project, as evident in figure 3.23, owing to improved deposition.

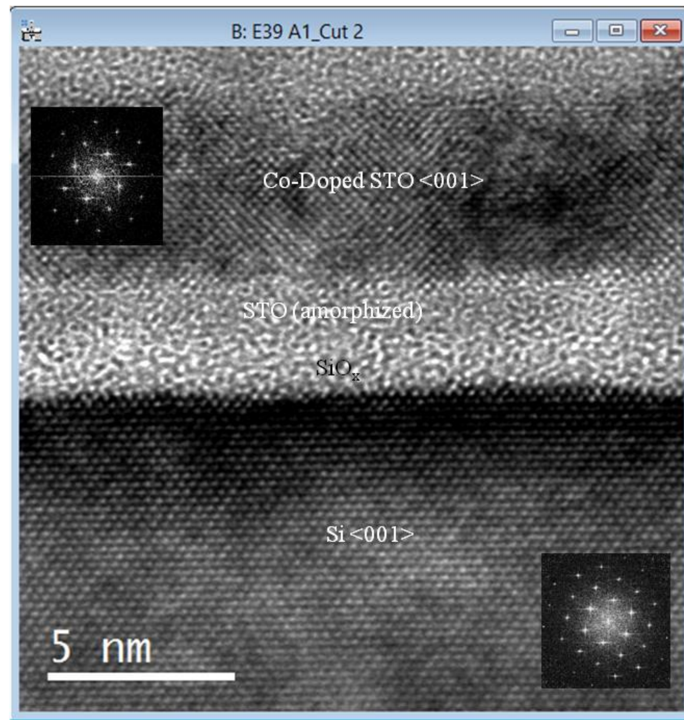

Figure 3.22 HRTEM image of cross-section of 30% Co-doped STO thin film on Si (001). Amorphized STO, SiO_x and SrO_x phases at interface. Insets are diffractograms from film and substrate.

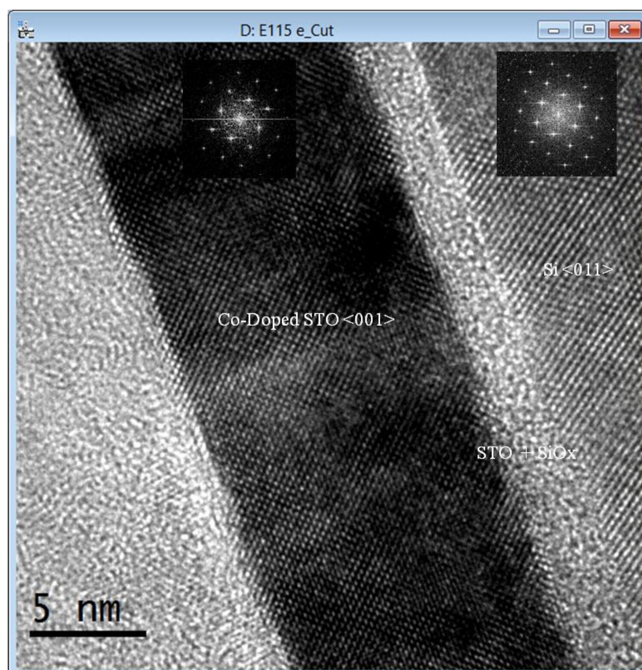

Figure 3.23 HRTEM image of cross-section of 25% Co-doped STO thin film on Si (001). Amorphous SiO_x and SrO_x at interface. Insets are diffractograms from film and substrate.

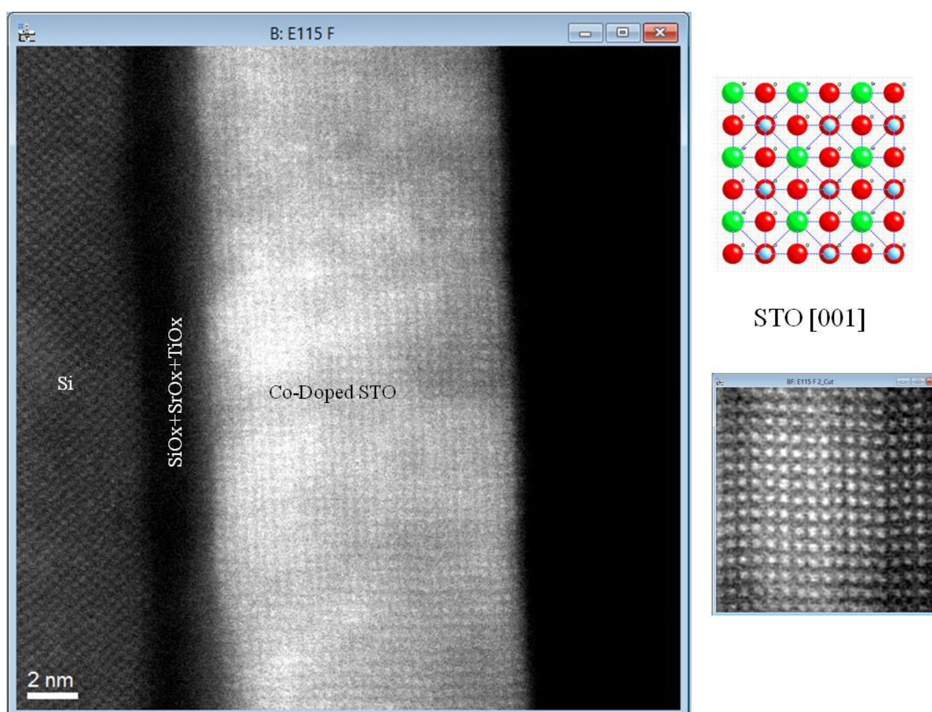

Figure 3.24 Cross-sectional HAADF image of 25% Co-doped STO grown on silicon, magnified view and atomic model of STO in (001) projection

HRTEM imaging also revealed the occasional presence of grain boundaries (not shown here) in the epitaxial STO film. Upon close HRTEM inspection and using Fourier filtering, the Co-doped films were observed to have a number of different types of defects, including stacking faults and edge dislocations (not shown). At 30% Co doping levels and without post-deposition annealing, this defect microstructure was anticipated.

Figures 3.24 is HAADF image showing the 25 % Co-doped STO on Si. These HAADF images show that the crystal quality of these films was not as high as Al-deposited films. Also shown is an image taken at higher magnification. In the HAADF imaging mode, the scattering intensity scales with the atomic number Z as ~ $Z^{1.7}$ [16] so that the brightest spots are at the positions of columns of Sr atoms (large green spheres in atom models), and the less bright spots in between the bright spots are the Ti–O or Co-O columns. Distinct dark amorphous region of SiO_x+SrO_x phase is also visible at the Si/STO interface. The ~1.5 nm undoped STO layer was observed to be amorphized.

Chemical composition and Co distribution in the STO films were characterized by Energy-Dispersive Spectroscopy (EDS) and by Electron-Energy-Loss Spectroscopy (EELS) techniques. Line-scans consisting of multiple spectra across a width of the sample were obtained and spectral images were recorded. The STEM probe size used for EDS was ~7 Å and for EELS was ~ 5 Å. Depending upon the step size, each individual spectrum was obtained from overlapped regions. Caution was taken to ensure that the sample drift was minimal. The EDS and EELS spectral images were then processed using Digital Micrograph. Figure 3.25 shows the raw data from elemental mapping of the sample using EDS. The data is quite smooth owing to the large probe size and long dwell

time ~0.5 s. Figure 3.26 depicts the line-scan geometry. The general trend of Co distribution across the sample is visible in figure 3.25. Since the Co-doped thin films were deposited at ~ 550 ^{o}C, it is to be expected that Co will diffuse in the STO lattice. Multiple line and area scans showed that the Co distribution in the STO lattice was quite random although occasional segregation of Co atoms in STO lattice corresponding to a peak in EDS distribution cannot be ruled out. Segregation of CoO phase in 40% Co-doped STO have been reported from XRD studies [31].

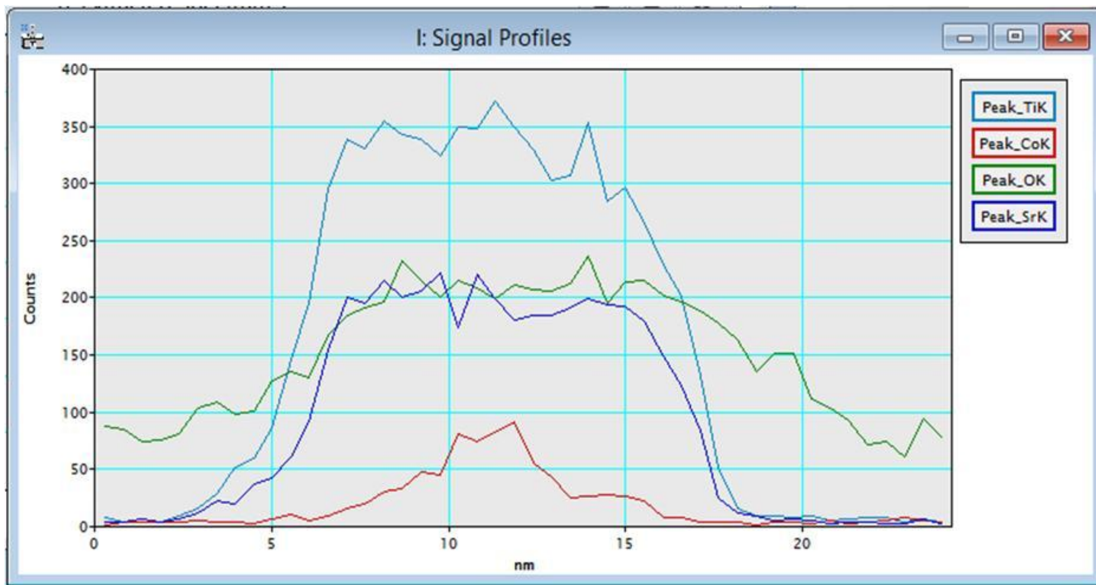

Figure 3.25 Elemental distribution across 25% Co-doped STO sample.

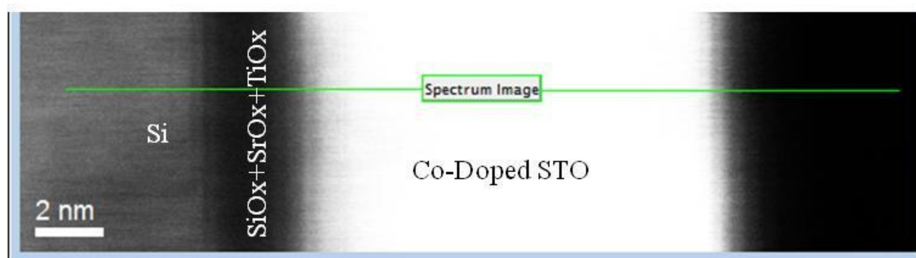

Figure 3.26 EDS line-scan geometry corresponding to figure 3.25

Elemental mapping made using EELS line-scans as shown in figures 3.27 and 3.28. The geometry of the line-scan is shown in figure 3.29. Areal density map of O-K and Ti- is shown in figure 3.27 and relative Ti:O composition is shown in figure 3.28. EELS elemental mapping tends to have better accuracy. The Ti-L and O-K peaks were all observed in the EELS spectrum. EELS quantification was done using Hartree-Slater algorithm in Digital Micrograph. The area density is quite uniform The Ti:O relative composition is a measure of amount of Ti^{4+} which is converted into Ti^{3+} or Ti^{2+} because of Ti atoms being substituted by Co^{3+} or Co^{2+} and associated production of oxygen for charge balancing [15-17]. The region of interest in figure 3.29 is a line of length ~4 nm in the middle of the Co-doped STO lattice. Uniform distribution of Ti and O is expected. A total of uniformly spaced 40 spectra were recorded along this line. Background subtracted spectra were processed for quantification purpose and electronic structure of Ti-L and O-K ELNES.

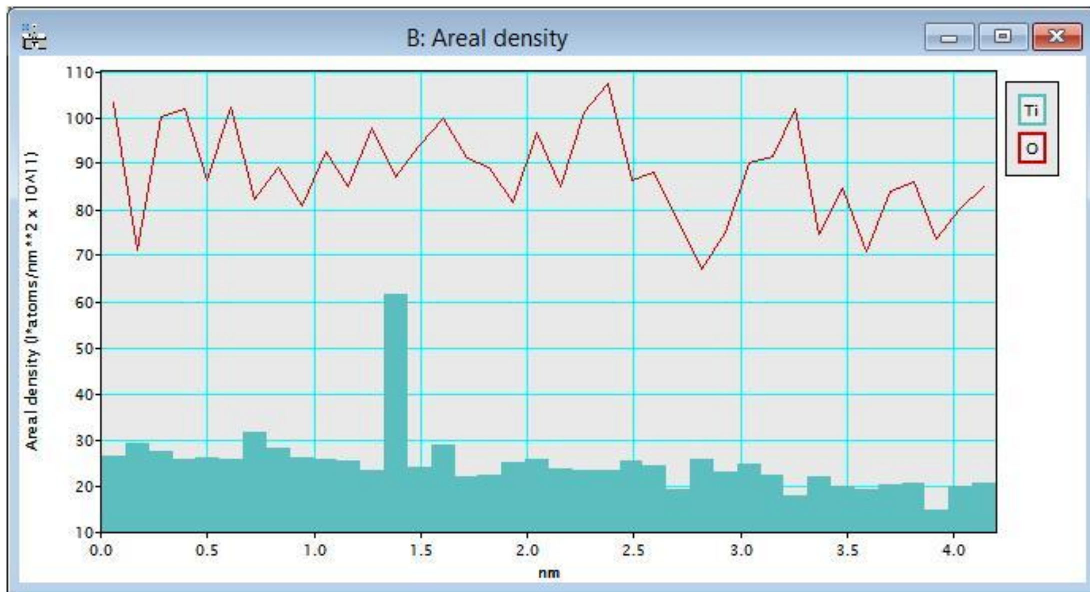

Figure 3.27 Ti and O areal distribution in 25% Co-doped STO lattice

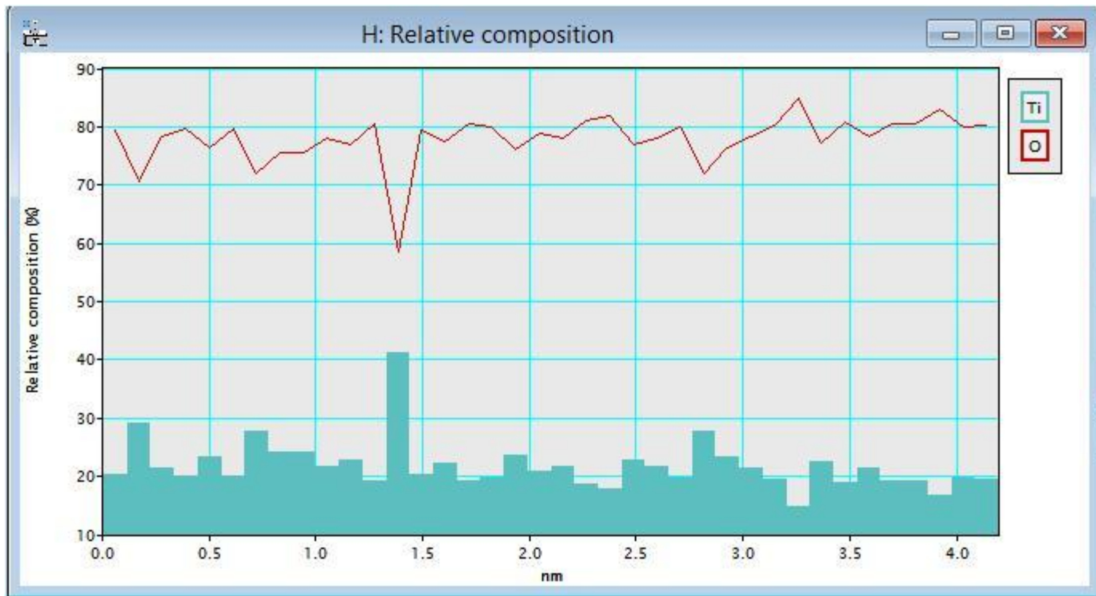

Figure 3.28 Relative composition of Ti and O distribution in 25% Co-doped STO

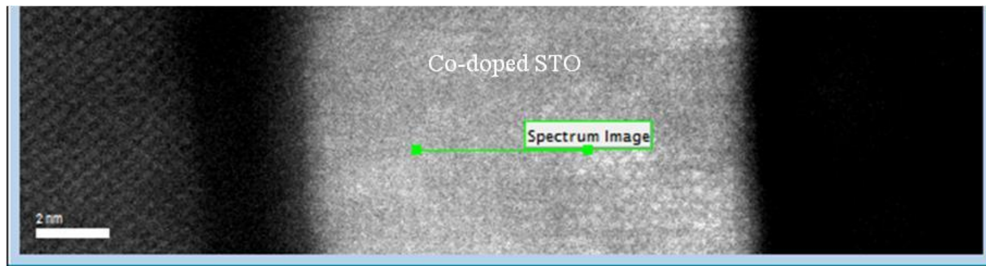

Figure 3.29 EELS line-scan geometry

3.3.2 Determining Electronic Structure

EELS line scans were recorded using GATAN Enfina EELS detector with the STEM probe (~ 5Å) with dwell time ~ 0.5 s and entrance aperture of 2 mm. For the electron probe in analytical mode, energy resolution of ~ 1.2 eV was obtained with the dispersion of 0.1 eV/pixel. Line-scans were processed using Digital Micrograph and spectra were background subtracted to get spectrum normalized to the continuum interval

30 eV before the onset of the Ti L edge and K-edge. The ELNES structure of Ti-L and O-K edges were averaged over 40 spectra and are shown in figure 3.30 and 3.31.

Co doping in STO deeply affects the STO electronic structure as well as the chemical structure and surrounding environment [15, 17]. Considering the fact that the ionic radii of Co^{+3} (~ 0.6 Å) [Co^{+2} (~ 0.7 Å)] and Ti^{+4} (~ 0.60Å) are almost the same, it can be anticipated that the dopant Co partially or completely substitutes for Ti. When Co substitutes for Ti then corresponding oxygen vacancies are created for charge neutrality. EELS, especially in the core-loss region, is a very powerful way to probe the electronic structure and to detect changes in the local chemical environment. The Ti-L_3 (456 eV) and Ti-L_2 (462) doublet and nearby O K (532) peaks are highly susceptible to the chemistry change, and have been used to detect changes in the amount of Ti and corresponding oxygen vacancies. As Co atoms substitute for Ti atoms, the shapes of the Ti L peaks and O K peaks should change because of Co doping in the STO lattice.

Changes in the core-loss peak shapes corresponding to changes in the crystal symmetry is well established [15-18]. Comparing our data with standard Ti-L and O-K fine edge structure published by Muller et al [16], as shown in figure 3.16, it is apparent that Co doping changed both the Ti-L and O-K fine-edge structure. EELS spectra provide very useful chemical and electronic information on the O and Ti states from the O-K (O 1s-2p) and Ti-L (Ti 2p-3d) core-edge structure. In general, ratios of integrated O-K and Ti-L edge intensities can directly give Ti/O ratio, as shown in figure 3.30. The Hartree-Slater cross sections were used for the EELS quantification [18].

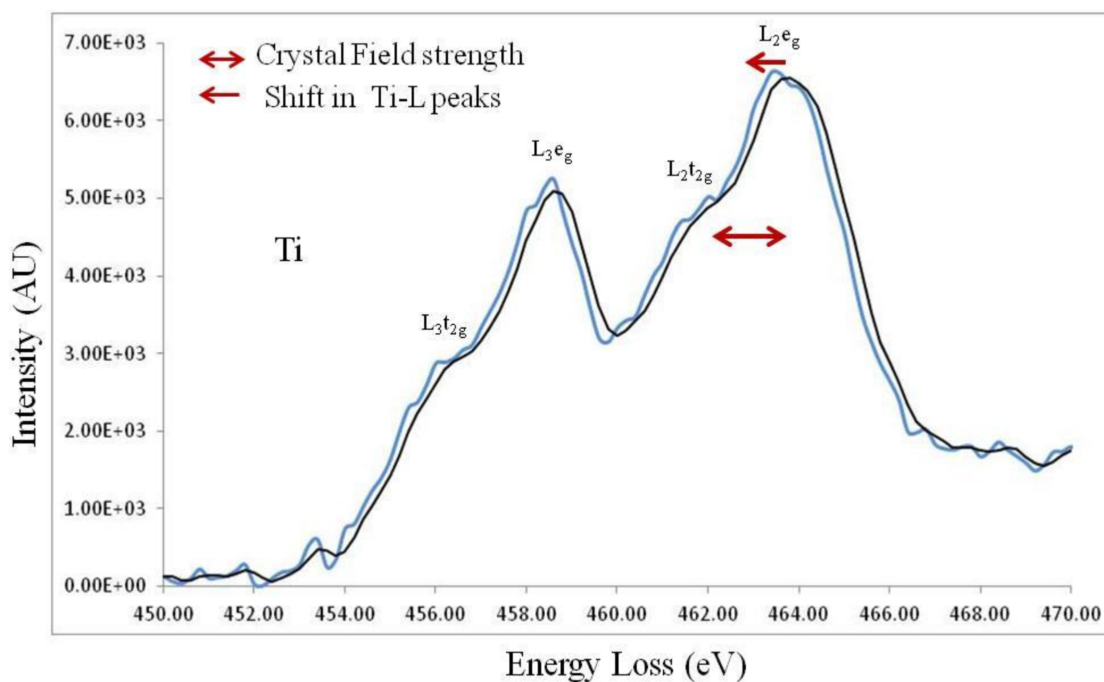

Figure 3.30 ELNES of Ti-L fine edge averaged over 40 spectra recorded along line-scan of length ~4 nm (blue). A trend line is added (black).

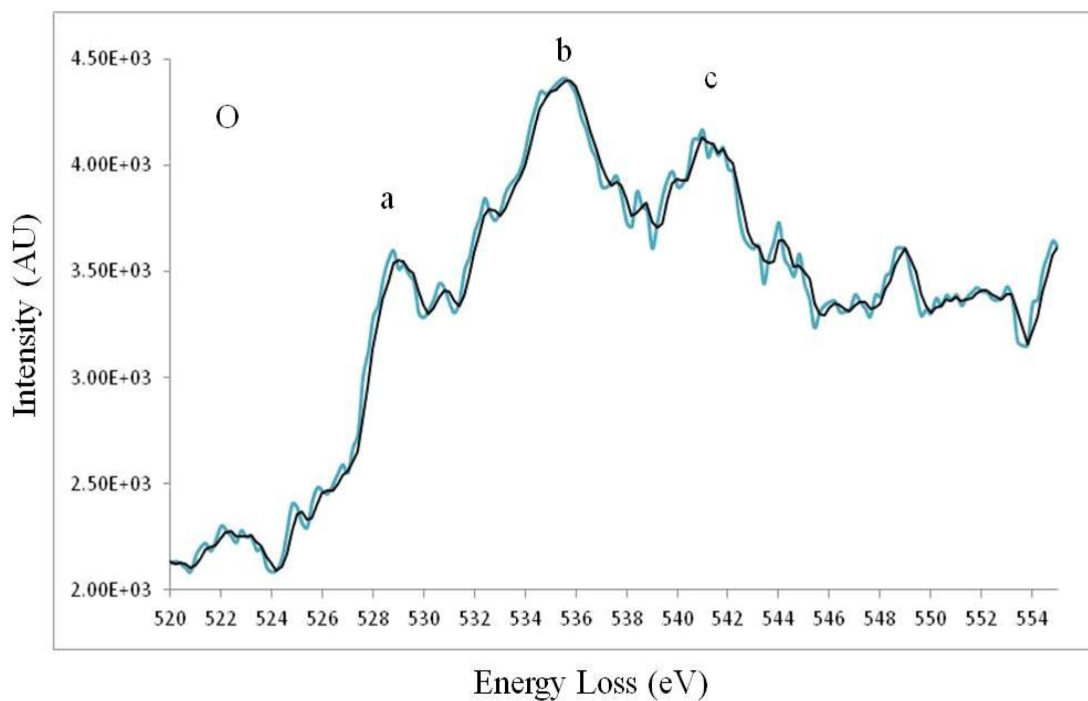

Figure 3.31 ELNES of O-K fine edge averaged over 40 spectra recorded along line-scan of length ~4 nm (blue). A trend line is added (black).

However, absolute quantification is not practical for low oxygen vacancy concentrations, especially in ultrathin film structures, such as ours, considering the fact that the errors in background subtraction can easily be a few percent [16]. The shape of the EELS edge, which reflects the underlying electronic structure, becomes more reliable. As shown in figure 3.16, the shape of the O-K fine edge structure changes (which is proportional to the unoccupied Op-density of states) and eventually damps out with the increasing amount of oxygen vacancies. The Ti-L edge is also useful and shows distinctly different spectra for the Ti_{3p} and Ti_{4p} formal valences [16].

The Ti-L edge splits into Ti-L_3 and Ti- L_2 peaks due to spin-orbit interaction. The spin-orbit interaction can be explained in terms of hybridization of 4*s* and 3*d* orbitals. L_3 and L_2 further split each into t_{2g} and e_g. This finer splitting is due to Crystal fields also known as Jahn-Teller fields. In the O fine spectrum, peaks are named with letters a, b c and corresponds to t_{2g}+e_g from Ti_{3d}-O_{2p} hybridization, Sr_{3d} and Ti_{4sp} hybridization respectively [18-19]. Oxygen peaks a, b and c in general represents quality of crystal. Ti_{3d} and O_{2p} form hybridized orbitals t_{2g} and e_g. This model is useful in explaining some of the features of EELS fine structure.

From the oxygen fine-edge spectrum in figure 3.31, and comparing it with standard data provided in figure 3.16, it is obvious that the oxygen percentage has changed in the Co-doped STO lattice. The distinct a, b and c peaks in the O-K edge are clearly visible. This feature is the indication of good long-range order and moderate amounts of oxygen vacancies. Thus, the amount of O vacancies has increased but not to the level of affecting the overall crystallinity. The crystal field affecting splitting of L_2

and L_3 Ti fine edges was observed to have reduced to (e_g-t_{2g}) ~ 1.5 eV from 2.4 eV observed in undoped STO [15]. Additional evidence for the presence of oxygen vacancies is provided by a down-shift in the Ti L-edge energy by ~0.4 eV. This is indicative of a lowering of the Ti valence from Ti^{4+} to Ti^{3+} to compensate for oxygen vacancies. The L_3/L_2 intensity ratio was calculated by finding the area under the L_3 and L_2 peaks and was found to be 0.79. This ratio was similar to the experimental value of the L_3/L_2 ratio of 0.8 reported for Ti-L peaks in undoped-STO [20]. Thus, the L_3/L_2 ratio obtained in our Co-doped STO sample was not in agreement with reported values.

The standard Ti-L and O-K curves by Muller et al [16] shown in figure 3.16, are for $SrTiO_{3-\delta}$, with δ changing from 0 to 0.25. For these fine-edge spectra, δ=0.13 corresponds to O vacancy of ~ 4 % and for δ=0.25 corresponds to O vacancy ~ 8 %. From the ELNES of Ti-L and O-K as in 3.30 and 3.31, and by comparing the graphs to 3.16, it is clear that for 25% Co doped-STO sample, the O vacancy levels were 5-8 % from Ti-L data and O vacancy levels were ~ 5 % from O-K data.

These results indicate that even at 25% Co doping levels, the O vacancy is ~5-8% and that Ti^{4+} valence has not changed much. There is some reduction in the Crystal field from 2.4 eV by ~0.5 eV indicating some change in the Ligand fields of Ti^{4+} and hence reduction in the Crystal symmetry. So if Ti^{4+} is not much being replaced by Co^{3+} or Co^{2+}, where is it going? Which site of STO lattice is being replaced by substituted Co? Is it cation A that is the Sr site? Independent work by our collaborators at the University of Austin using XPS, resistivity measurements, magnetic measurements and DFT revealed that most of the substituted Co is Co^{2+} and an associated oxygen vacancy forms a Co-O

complex in STO. Significantly large amount of Sr vacancies were also observed possibly due to Co-O complex replacing Sr atoms [31].

Is it possible that most of the doped Co in STO is segregating? Is Co segregating at grain boundaries? A similar work on Mn-doped STO showed that the doping mechanism remains ambiguous as Mn^{4+} is found to substitute Ti^{4+} in bulk STO, but Mn^{2+} segregates inside grain boundaries at both Sr and interstitial sites [33]. Like in the case of Mn is it possible that Co is occupying cation interstitial sites (which are not observed in the image or in the integrated intensity of the EELS spectra). These interesting questions remain to be answered in the future.

3.4 Conclusions

The ~10% and ~ 20% Al-doped STO thin films epitaxially grown on Si were high quality single crystal thin films. EDS and EELS line scans followed expected Al doping in STO lattice. The Ti/O ratio from EELS line scan revealed that any possible substitution of Ti by Al created associated O vacancies. Crystal field in STO was measured directly using ELNES and it was found that the Crystal field strength decreased by ~1.0 eV as Ti^{4+} was substituted by Al^{3+}. The decreased Crystal-field strength suggested loss of crystalline symmetry owing to changed bond-angles and bond-radius. Shift of L_2 and L_3 towards lower energy and slight rise in the L_3/L_2 ratio as a function of Al substitution confirmed the increased oxygen valence levels. The damping of peaks in O-K ELNES data confirmed the rise in oxygen vacancies. By doping Ti^{4+} with Al^{3+} creates associated oxygen vacancies that possibly block Ti-Ti hopping conduction

mechanism, suggest mechanism of an enlarged band gap for Al-doped STO. Al-doped STO could be a possible way for band-gap engineering in STO integrated in semiconductor devices.

Cobalt-substituted STO films grown on Si were observed to be good quality single crystal. EDS and EELS line scans across the samples revealed that Co doping was quite random. By substituting Ti^{4+} with Co^{3+} or Co^{2+} created associated oxygen vacancies for charge balance. Presence of oxygen vacancies was confirmed by shift of L_2 and L_3 towards lower energy by ~0.4 eV. Crystal field in Co-doped STO was measured directly using ELNES and it was found that the crystal field strength decreased by ~0.8 eV as Ti^{4+} was substituted by Co^{3+} or Co^{2+}. The decreased Crystal-field strength suggested loss of crystalline symmetry. Theoretical calculations revealed that oxygen vacancies are crucial in stabilizing ferromagnetism in this system and that a cobalt-oxygen vacancy complex is responsible for the observed insulating and magnetic behavior. Co-doped STO could be a possible route for epitaxially integrating a room-temperature ferromagnetic insulator on silicon for future spin-electronics devices.

References

1. H. Y.Hwang, MRS Bulletin, Vol 31 (2006) 28-35.

2. D. G. Schlom and J. Mannhart, Nature Materials, 10 (2011) 168-169.

3. W. Luo, W. Dua, S. G. Louie and M. L. Cohen, Physical Review B, 70 214109 (2004).

4. Y.L. Zhu, X.L. Ma, D.X. Li, H.B. Lu, Z.H. Chen, G.Z. Yang, Acta Materialia, Vol. 53, Issue 5, March 2005, Pages 1277–1284.

5. S.Y. Dai, H. B. Lu, Z.Y. Ren, D.H. Ng, Appl Phys Lett, 80 (2002), 3545-3548.

6. H. Guo, L. Liu, Y. Fei, W. Xia, Y. Zhou and Z. Chen, J. Appl. Phys. 94, 4558 (2003).

7. A. Leitner, C.T. Rogers, J.C. Price, D.A. Rudman, D.R. Herman, Appl Phys Lett, 72 (1998), 3065-3069.

8. Wakiya, N., Kimura, Y., Sakamoto, N., Fu, DS, Hara, T., Ishiguro, T., Kiguchi, T., Shinozaki, K., Suzuki, H., JOURNAL OF THE CERAMIC SOCIETY OF JAPAN, Volume: 117 Issue: 1369 Pages: 1004-1008.

9. Muenstermann, R., Menke, T., Dittmann, R ., Waser, R., Advanced Materials, Volume: 22 Issue: 43 Pages: 4819-4824.

10. Phan, B.T., Choi, T., Lee, J ., Integrated Ferroelectrics, Volume: 96 Pages: 146-152.

11. Kawasaki, S., Nakatsuji, K., Yoshinobu, J., Komori, F., Takahashi, R., Lippmaa, M., Mase, K., Kudo, A., Applied Physics Letters, Volume: 101 Issue: 3, 033910.

12. Huan-hua W., Da-fu C., Sou-yu D., Hui-bin L., Yue-liang Z., Zheng-hao C. and Guo-zhen Y. J. Appl. Phys. 90, (2001) 4664-4667.

13. A. B. Posadas, C. Lin, A. A. Demkov, S. Zollner, Applied Physics Letters, 103, 142906 (2013).

14. M. D. McDaniel, A. Posadas, T. Q. Ngo, A. Dhamdhere, D. J. Smith, A. A. Demkov, and J. G. Ekerdt, Journal of Vacuum Science & Technology B 30, 04E111 (2012).

15. R.F. Klie, I. Arslan, and N.D. Browning, Journal of Electron Spectroscopy and Related Phenomena 143 (2005) 105–115.

16. D. A. Muller, N. Nakagawa, A. Ohtomo, J. L. Grazu, H. Y. Hwang, Nature, Vol 430, 5 Aug. 2004, 657-661.

17. M. Varela, J. Gazquez, S. J. Pennycook, MRS Bulletin Vol. 37 (2012) 29-35.

18. Z. Zhang, W. Sigle, and M. Ruhle, Physical Review B 66, 094108 (2002).

19. Z. Zhang, W. Sigle, and W. Kurtz, Physical Review B 69, 144103 (2004).

20. W. G. Waddington, P. Rez, I. P. Grant, C. J. Humphreys, Physical Review B, Vol. 34, (3) 1986, 1467-1474.

21. S. A. Wolf, D. D. Awschalom, R. A. Buhrman, J. M. Daughton, S. von Molnar, M. L. Roukes, A. Y. Chtchelkanova, and D. M. Treger, Science 294, 1488 (2001).

22. G. Schmidt, D. Ferrand, L. W. Molenkamp, A. T. Filip, and B. J. van Wees, Phys. Rev. B 62, R4790 (2000).

23. A. H. MacDonald, P. Schiffer, and N. Samarth, Nature Materials 4, 195 (2005).

24. Y. Matsumoto, M. Murakami, T. Shono, T. Hasegawa, T. Fukumura, M. Kawasaki, P. Ahmet, T. Chikyow, S. Koshihara, and H. Koinuma, Science 291, 854 (2001).

25. C. Song, K. W. Geng, F. Zeng, X. B. Wang, Y. X. Shen, F. Pan, Y. N. Xie, T. Liu, H. T. Zhou, and Z. Fan, Phys. Rev. B 73, 024405 (2006).

26. S. B. Ogale, R. J. Choudhary, J. P. Buban, S. E. Lofland, S. R. Shinde, S. N. Kale, V. N. Kulkarni, J. Higgins, C. Lanci, J. R. Simpson, Phys. Rev. Lett. 91, 077205 (2003).

27. J. Philip, A. Punnoose, B. I. Kim, K. M. Reddy, S. Layne, J. O. Holmes, B. Satpati, P. R. Leclair, T. S. Santos, and J. Moodera, Nat. Mater. 5, 298 (2006).

28. R. A. McKee, F. J. Walker, and M. F. Chisholm, Phys. Rev. Lett. 81, 3014 (1998).

29. C. Pascanut, N. Dragoe, and P. Berthet, J. Magn. Magn. Mater. 305, 6 (2006).

30. S. X. Zhang, S. B. Ogale, D. C. Kundaliya, L. F. Fu, N. D. Browning, S. Dhar, W. Ramadan, J. S. Higgins, R. L. Greene et al., Appl. Phys. Lett. 89, 012501 (2006).

31. A. B. Posadas, C. Mitra, C. Lin, A. Dhamdhere, D. J. Smith, M. Tsoi, and A. A. Demkov, Physical Review B 87, 144422 (2013).

32. J. Q. He, C. L. Jia, V. Vaithnayathan, D. G. Schlom, J. Schubert, A. Gerber, H. H. Kohlstedt, and R. H. Wang, J. Appl. Phys. 97, 104921 (2005).

33. H. Yang, P. G. Kotula, Y. Sato, M. Chi, Y. Ikuhara and N. D. Browning, Mater. Res. Lett., 2014 Vol. 2, No. 1, 16–22.

CHAPTER 4

$Co_3O_4/MgAl_2O_4$ (110) SPINEL HETEROSTRUCTURES

4.1 Introduction

The spinels are a class of minerals of general formula $A^{2+}B^{3+}{}_2O^{2-}{}_4$ with space group symmetry Fd3m [1]. Spinels crystallize in the cubic crystal system, with the oxide anions arranged in a cubic-close-packed lattice and the cations A and B occupying some or all of the octahedral and tetrahedral sites in the lattice, with one octahedral and two tetrahedral sites per formula unit. The charges of cations A and B in the normal-spinel structure are generally +2 and +3, respectively, but other combinations incorporating divalent, trivalent, or tetravalent cations, including magnesium, zinc, iron, manganese, aluminum, chromium, titanium, and silicon, are also possible [1-2]. The anion is normally oxygen. A and B can also be the same metal with different valence, as is the case for Co_3O_4. The tetrahedral spaces are smaller than the octahedral spaces. B^{3+} ions occupy octahedral holes, while A^{2+} ions occupy tetrahedral holes. The mineral spinels $MgAl_2O_4$ and Co_3O_4 have a normal-spinel structure. Inverse-spinel structures have a different cation distribution in that all of the A cations and half of the B cations occupy octahedral sites, while the other half of the B cations occupy tetrahedral sites. An example of an inverse spinel is Fe_3O_4 [1-2]. In addition, there are intermediate cases where the cation distribution can be described as $(A_{1-x}B_x)[A_{x/2}B_{1-x/2}]_2O_4$, where parentheses () and brackets [] are used to denote tetrahedral and octahedral sites, respectively. The symbol x denotes the degree of inversion and x has values between 0

(normal) and 1 (inverse), and is equal to 2/3 for a completely random cation distribution. The spinel crystal structure is also determined by the anion or oxygen parameter u. When u=0.275, A and B site have exact tetrahedra and octahedra, respectively. Changes in u from this value represent distortions in the symmetry [1-3].

Magnesium aluminate spinel $MgAl_2O_4$, as shown in figure 4.1, is the parent compound of the spinel group. Its spinel structure is described as a distorted face-centered-cubic array of oxygen anions, with Mg^{2+} cations occupying 1/8 of the 64 tetrahedral interstices available in the unit cell and the Al^{3+} cations occupying half of the 32 octahedral interstices present. Spinel materials have a very high propensity for cation exchange between the two distinct sublattices. During cation exchange, the O^{2-} anions are correspondingly displaced from ideal sites in <111> directions away from the tetrahedral Mg^{2+} cations and towards the Al^{3+} cations [3].

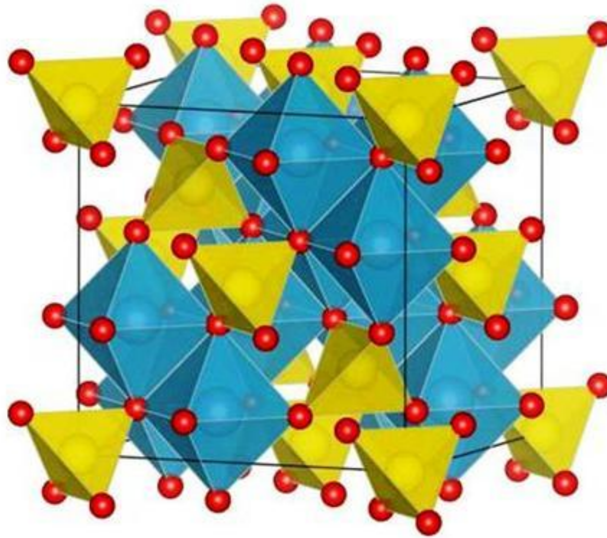

Figure 4.1 $MgAl_2O_4$ structure consisting of distorted face-centered-cubic array of oxygen anions (red spheres), with Mg^{2+} cations occupying 1/8 of the tetrahedral interstices (yellow tetrahedron) and the Al^{3+} cations occupying half of the octahedral interstices (blue octrahedra) [3].

At room temperature, the most stable form of cobalt oxide, Co_3O_4, has the normal spinel structure, as shown in figure 4.2. The spinel with space group Fd3m has the formula $[Co^{2+}]_A[Co^{3+}Co^{3+}]_BO_4$. The Co^{2+} ions, which carry a magnetic moment, are at the vertex-sharing tetrahedral (A) site and are in a high-spin state (S = 3/2). Nonmagnetic Co^{3+} ions are at edge-sharing octahedral (B) sites, and their spin state changes from low spin (S=0) to high spin with increasing temperature. Co_3O_4 undergoes an antiferromagnetic phase transition below the Neel temperature of 30 K [4].

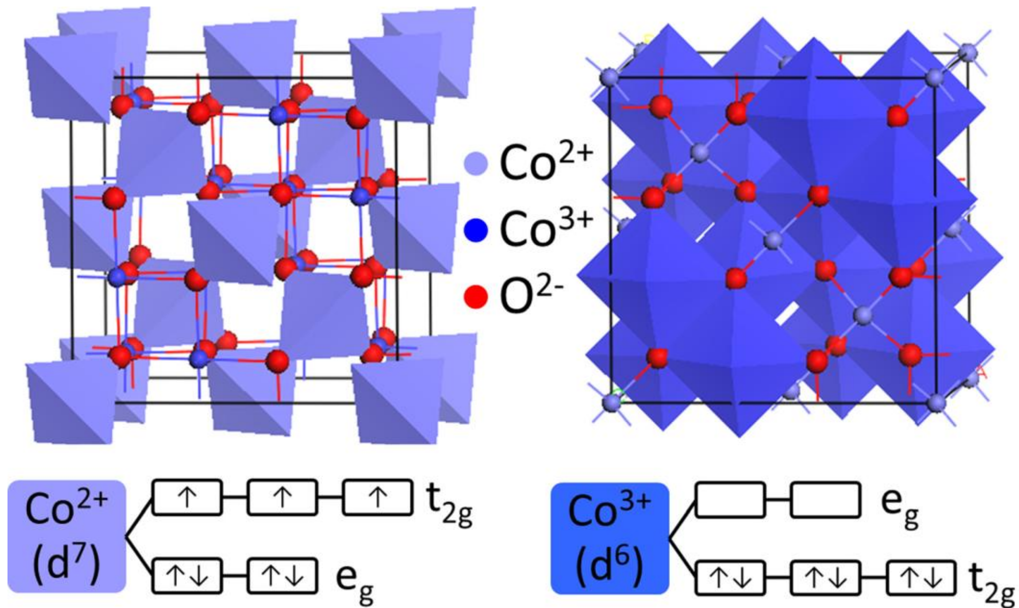

Figure 4.2 At room temperature, Co_3O_4 assumes the normal spinel structure. Due to the crystal field splitting, the Co^{2+} ions (tetrahedral, light blue) carry magnetic moment, while the Co^{3+} (octahedral, dark blue) ions are nonmagnetic [5].

Cobalt spinels have a history of use as gemstones, and their high stability makes them well-suited for the decoration of ceramics (cobalt-containing spinels, in particular, are responsible for the striking "cobalt blue" pigment). Complex oxides of cobalt find applications in gas-sensing, spintronics, batteries, and particularly in catalysis, notably for

oxidation of carbon monoxide. Since surfaces and interfaces play important roles in the field of catalysis, study of the surfaces and interfaces of Co_3O_4 spinel is essential to understand physical properties and catalytic behavior. Of particular interest is the (110) plane which exhibits significantly higher reaction rates due to the presence of active Co^{3+} species at the surface [5-7]. The (110) direction of Co_3O_4 contains two types of alternating planes: the most stable type-A plane is comprised of units of $Co^{2+}{}_2Co^{3+}{}_2O_4$ with a formal charge of +2, while the type-B planes include $Co^{3+}{}_2O_4$, resulting in a charge of -2 per surface unit cell. All of the low-index planes of Co_3O_4 are polar. This polarity further motivates study of polar Co_3O_4, since polar oxides are of prominent interest due to their increased surface reactivity as compared to the bulk, and as a possible mechanism for the formation of a two-dimensional electron gas (2DEG) [5-7].

4.2 Experimental Work

In this work, Co_3O_4 films were deposited on isostructural spinel $MgAl_2O_4$ (110) substrates [5]. $MgAl_2O_4$ (a=0.809 nm) is an ideal substrate choice not only due to its small lattice mismatch (~ 0.06%) with Co_3O_4 (a=0.8084 nm) but also due to the fact that it is the only substrate thus far on which Co_3O_4 preferentially grows (110)-oriented. The (110) plane of Co_3O_4 spinel exhibits significantly higher catalytic activity, such as carbon monoxide conversion, due to the presence of active Co^{3+} species at the surface. The Co_3O_4 thin films were grown by molecular-beam epitaxy (MBE) on $MgAl_2O_4$ substrates [5]. The structure of these as-grown highly crystalline (110)-oriented films was monitored by reflection-high-energy electron diffraction (RHEED) during growth. The RHEED patterns showed sharp diffraction maxima, as expected for a periodic surface

with negligible roughness. The spot spacings visible in RHEED patterns indicated that there was no change in the in-plane lattice constant of the film compared to the substrate. As the Co_3O_4 films grew, they followed the substrate termination to preserve charge neutrality, as is common in polar materials. Surface roughness on the order of 0.2 nm was measured using atomic-force microscopy (AFM). X-ray diffraction (XRD) measurements confirmed that the films were nearly lattice-matched to the substrate [5].

In this work, the structure of as-grown highly crystalline (110)-oriented films and the epitaxial interfaces were studied by high-resolution transmission electron microscopy (TEM) to determine the crystalline quality of thin films, film orientation, and film-substrate interface. Cross-sectional TEM samples were prepared with foil normals in [011] and [001] projections using conventional mechanical polishing and dimple grinding followed by precision ion milling at ~ 3.5 keV to achieve final thickness for electron transparency. The samples were studied using the JEOL JEM 4000EX electron microscope operated at 400 keV with C_s = 1.0 mm yielding structural resolution of ~ 1.7 Å. HRTEM images were obtained with imaging conditions of Scherzer defocus of -49 nm, spherical aberration coefficient of C_s= 1.0 mm, half-convergence angle of 0.6 mrad and defocus spread of 6 nm. All images were takes very close to the Scherzer defocus. HRTEM images and diffractograms obtained from experimental images were compared with simulated images and diffraction patterns to determine orientation.

Figure 4.3 (a) show a HRTEM micrograph of Co_3O_4 thin film deposited on $MgAl_2O_4$ (110). The micrograph is projected in <011> and the inset is the diffractogram obtained from image 4.3 (a). Figures 4.3 (b) and (c) are magnified views of cross-section

cuts made from 4.3 (a). The HRTEM micrographs show formation of high crystalline quality Co_3O_4 films and formation of an atomically flat and coherent interface between Co_3O_4 and $MgAl_2O_4$. This implies that any chemical changes on a local scale such as interdiffusion between the crystals were not significant.

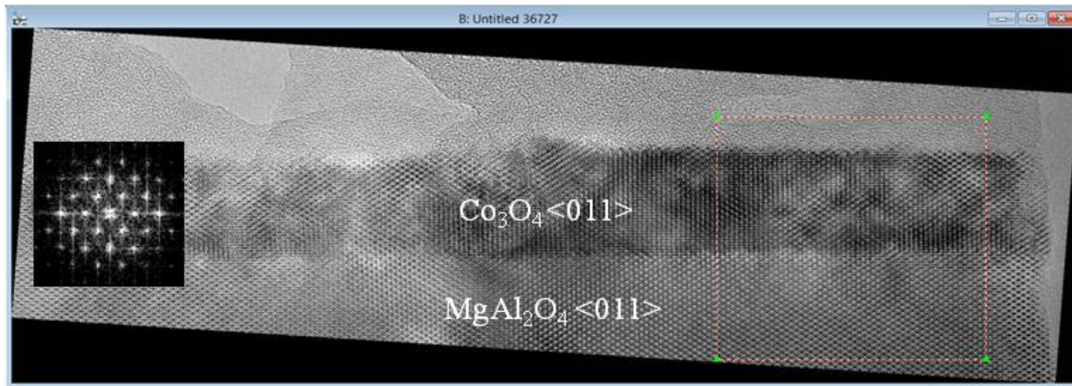

(a) Area of interest at higher magnification

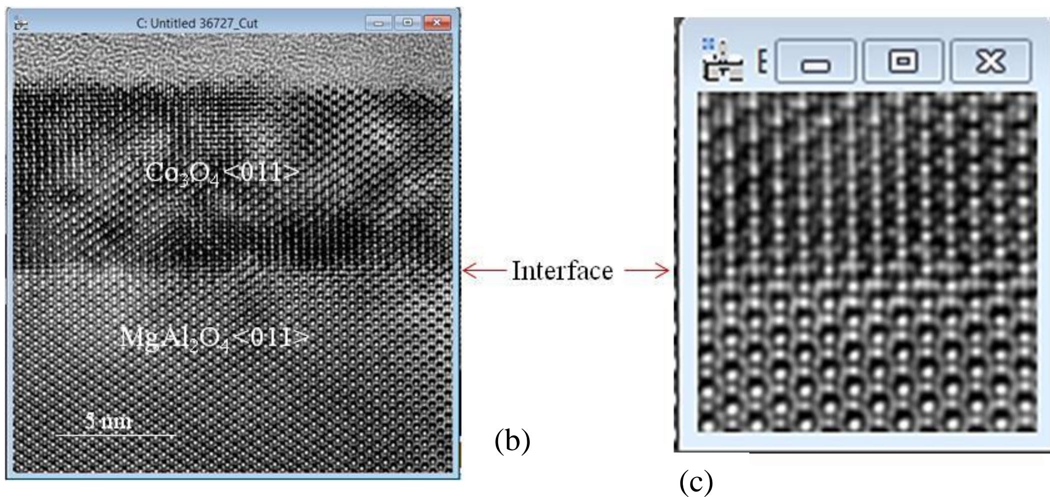

Figure 4.3 HRTEM micrographs. (a) Region of original cross-section micrograph of $Co_3O_4/MgAl_2O_4$ (110) heterostructure viewed in [011] projections. (b), (c) are enlarged interface images.

It is difficult to determine the exact interface plane from the HRTEM images. The intensity of peaks in the interface region on both sides is periodic as in the bulk. In addition, the image contrast along the interface is almost uniform. The $Co_3O_4/MgAl_2O_4$

interface structure was determined using the HRTEM image in figure 4.3 and HRTEM image simulations.

4.3 Determining Interface Structure

The importance of understanding the detailed atomistic structure and energetics of film/substrate interfaces in heteroepitaxial growth cannot be underestimated. Interface properties depend upon termination plane of the substrate. The exact termination plane within the (110) planes of the substrate $MgAl_2O_4$ was difficult to determine solely from analysis of the HRTEM images, as shown in figure 4.3. Hence $Co_3O_4/MgAl_2O_4$ HRTEM images were compared with image simulations. To construct models of the $Co_3O_4/MgAl_2O_4$ interface, normal spinel $MgAl_2O_4$ and Co_3O_4 with two different possible terminations of the substrate $MgAl_2O_4$ were considered. Since the lattice constants of Co_3O_4 and $MgAl_2O_4$ are very similar, the models should have coherent interfaces. In the case of $MgAl_2O_4$ in [110] direction, two types of terminations are possible: Type A having both Mg and Al cations with oxygen anions and type B having only Al and oxygen atoms. For both of these $MgAl_2O_4$ terminations, interface models were constructed with electro-neutrality conditions imposed upon the constituent ions. Only one structure was identified for each termination, as shown in figures 4.4(a) and 4.5(a). Two simple approximations were made. First, both models were coherent with very similar lattice constants. Second, the models were completely defect-free and stoichiometric. Since spinels have cations with a high propensity for migration, and hence vacancy formation with rigid anion lattice, this approximation is only of first order, especially near the interface region.

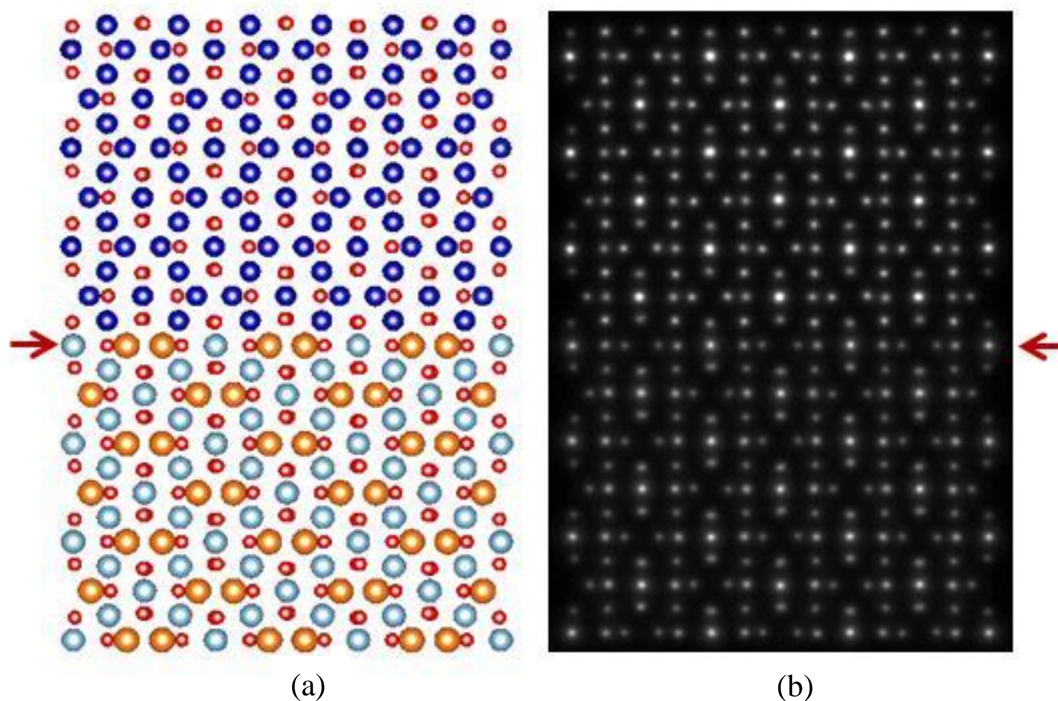

(a) (b)

Figure 4.4 (a) Model A with Mg (orange), Al (light blue) and O (red) in the top layer of $MgAl_2O_4$ shown by the arrow. (b) calculated projected potential based on model shown in (a).

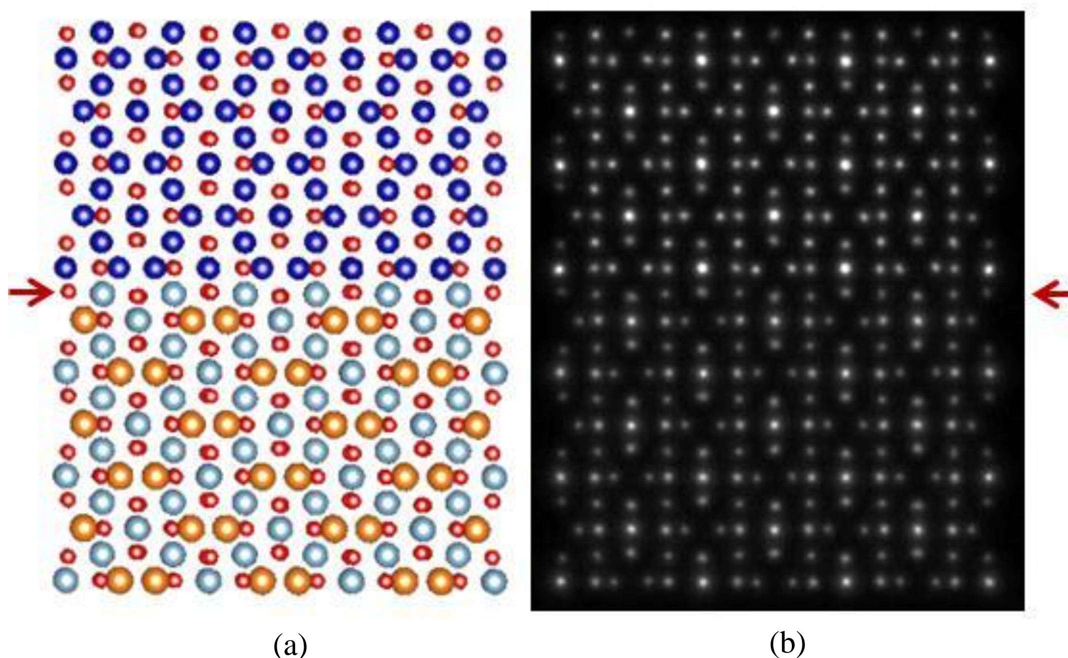

(a) (b)

Figure 4.5 (a) Model B with Al (light blue) and O (red) in the top layer of $MgAl_2O_4$ shown by the arrow. (b) calculated projected potential based on model B.

The crystal models were built using the commercial software Crystalmaker by altering individual crystals of Co_3O_4 and $MgAl_2O_4$ and cutting the models in proper orientation and planes. These altered individual models were then combined coherently to form the required interface model with symmetry across the interfaces maintained. The only differences between models A and B are the two different atomic planes at the interface. The projected potentials for models A and B were calculated and are shown in figures 4.4(b) and 4.5(b). Even slight differences between the two atomic models are revealed in projected potentials at the interface.

The models were imported into the image simulation software program JEMS, and HRTEM images were then simulated using the multislice module. The imaging conditions chosen were identical to those used for observation with the JEOL JEM 4000EX: operating voltage of 400 kV, Scherzer defocus of -49 nm, spherical aberration coefficient of C_s= 1.0 mm, half-convergence angle of 0.5 mrad and defocus spread of 6 nm. Although the experimental images were obtained close to the Scherzer defocus, the sample thickness and defocus values of the experimental images were not exactly known. Hence, thickness-defocus series were calculated to create an array of images with different defocus and thickness values. Every image was then matched with the experimental image to identify the best match. Near Scherzer defocus, the bright spots in the simulated and experimental images represent the positions of oxygen columns. A perfect oxygen lattice is observed from the images. The darker spots correspond to the positions of the Co or Mg or Al columns. Figures 4.6 and 4.7 show the best overall matches between simulated and experimental images for the two models.

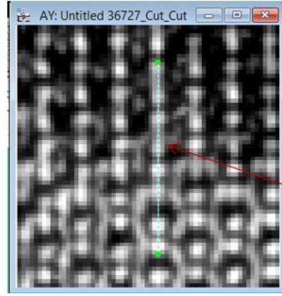

6a. Experimental Image of interface

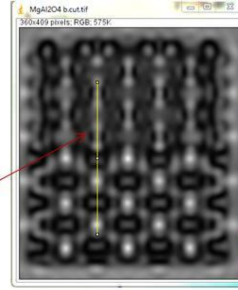

6b. Simulated image of Model A

Profile from top to bottom along the line

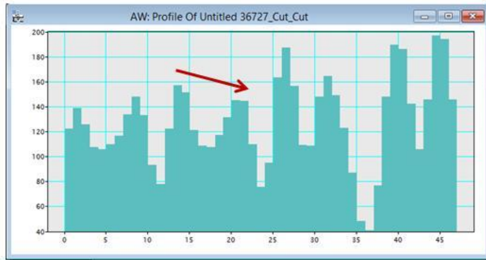

6aa. Line profile across cross-section of experimental image in 6a

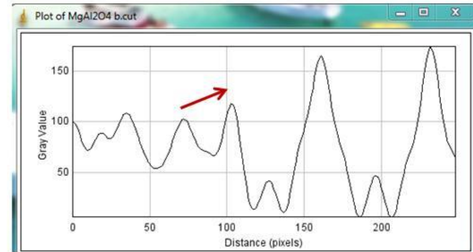

6bb. Line profile across cross-section of simulated image in 6b

Figure 4.6 Experimental and simulated images for interface model A. Line profiles across interface of experimental and simulated images. The arrows in 6aa and 6bb represents intensity profile along the profile line.

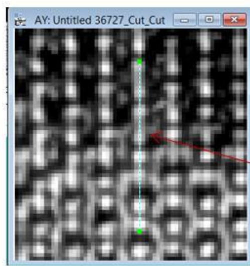

7a. Experimental Image of interface

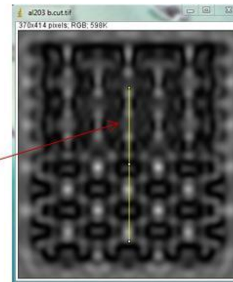

7b. Simulated image of Model B

Profile from top to bottom along the line

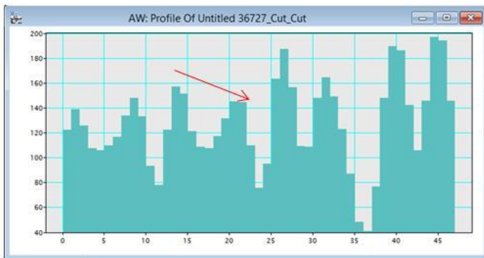

7aa. Line profile across cross-section of experimental image in 7a

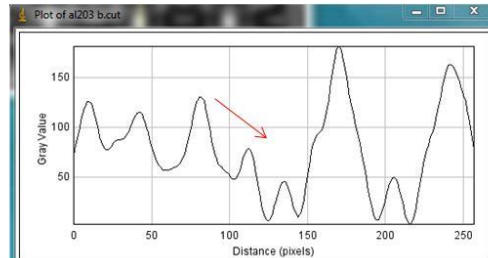

7bb. Line profile across cross-section of simulated image in 7b

Figure 4.7 Experimental and simulated images for interface model B. Line profiles across interface of experimental and simulated images. The arrows in 4.7aa and 4.7bb represents intensity profile along the profile line.

Figures 4.6 and 4.7 were then exported into Digital Micrograph to obtained line profiles along the positions of the atom columns. Profiles were obtained along multiple atomic columns across the interface and then compared. Examples are shown in figures 4.6 and 4.7. A comparison of experimental and simulated line profiles along the atomic columns across the interface for both models, reveals that model B with only Al and O atoms in the termination layer of substrate $MgAl_2O_4$ is the better fit, corresponding to the Co_3O_4 thin film grown on the Al-O-terminated $MgAl_2O_4$ substrate. The atomistic structure and energies for interfaces with the two types of termination plane, i.e., $MgAl_2O_4$ and Al_2O_3-termination of $MgAl_2O_4$ have been theoretically evaluated [3,8]. The Al_2O_3-termination shows lower interfacial energy than the $MgAl_2O_4$-termination under most chemical potential conditions [3, 8]. Quantum Density Functional Theory atomistic simulation techniques have been employed to investigate the defect chemistry accommodating non-stoichiometry at the interfaces. The incorporation of excess Al_2O_3 was found to be a lower energy process than the solution of excess MgO [3]. It has also been reported that type A termination of the substrate and the film after annealing, and the B termination for as-grown substrate and film yield stable films, suggesting a potential kinetic barrier to forming the apparently thermodynamically favorable lower energy A termination during growth [7].

4.4 Defects in $Co_3O_4/MgAl_2O_4$

In the previous section, it was pointed out that the $Co_3O_4/MgAl_2O_4$ heteroepitaxy was intimately related to interfacial structure and energy. Apart from the situation when a chemical reaction occurs at the film/substrate interface, interfacial structure depends on the stiffness of interfacial bonding and the elasticity of the two constituent crystals, as well as the lattice misfit. In general, lattice misfit causes strain fields across the interface, and the strain is manifest by the presence of dislocations. The high density of dislocations in spinels modifies the cationic stacking and the cationic environment [9].

It is expected that identical crystal structures and almost identical lattice constants of Co_3O_4 and $MgAl_2O_4$ would preclude the formation of antiphase boundaries (APBs) in $Co_3O_4/MgAl_2O_4$ heterostructures. Such APBs usually originate when lower symmetry structures are grown on higher symmetry surfaces, which is not the case for the $Co_3O_4/MgAl_2O_4$ system [6-7]. The chemical and thermal stability of $MgAl_2O_4$ should ensure no interdiffusion at high growth temperatures. The (110) surface is also characterized by having a four-repeat period, as opposed to the eight-period repeat of the (100) surface, and it should therefore be less susceptible to stacking faults and antiphase boundary formation, leading in principle to fewer defects [7]. The presence of APBs was not observed in the as-grown $Co_3O_4/MgAl_2O_4$ samples where the lattice misfit was of ~0.06%. However, localized misfit dislocations were observed in {002},{011}, {111} and {113} planes. This occasional presence of edge dislocations can be expected considering that spinel materials in general have a high propensity for dislocation formation, and these films were not annealed [5].

The long-range strain fields associated with defects in spinels are of considerable importance since these strain fields affect the cation distribution. The defects can directly affect the magnetic properties of the spinels, and the interaction of defects with charge carriers can occur far from defect cores thus also affecting transport properties. Geometric phase analysis (GPA) of HRTEM images is a powerful method of image analysis which can be directly related to any displacement fields associated with distortions in lattice fringes relative to the reference lattice [10]. The corresponding strain field can then be found by analyzing the derivative of the displacement field. A GPA program compatible with Digital Micrograph was thus employed for calculating strain maps in the $Co_3O_4/MgAl_2O_4$ heterostructure. Strain maps were obtained in x (plane parallel to the film/substrate interface), y (direction of growth of thin film) and x-y directions. HRTEM images in both {110} and {001} foil projections were used for GPA analysis. Simultaneously, the same HRTEM images were filtered by applying Bragg filtering in Fourier space. GPA analysis clearly showed the presence of strain fields associated with the presence of corresponding stacking faults.

Figures 4.8 and 4.9 show contrast transfer functions of the JEOL 4000EX at optimum defocus, and corresponding allowed reflections in {110} and {001} projections of the spinel heterostructure $Co_3O_4/MgAl_2O_4$. The number of reflections contributing to the image are limited by the envelope function. The spread of focus and beam divergence were adjusted to obtain the contrast transfer functions (black curve) shown in figures 4.8 and 4.9. Only allowed reflections were used for GPA analysis.

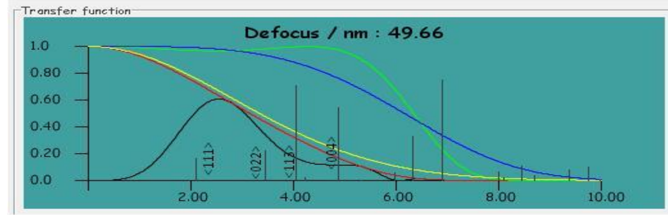

Figure 4.8 Contrast transfer function of JEOL-4000EX at optimal defocus of 49.7 nm. For {110} projected spinel, <111>, <022>, <113> and <004> reflections are allowed by CTF.

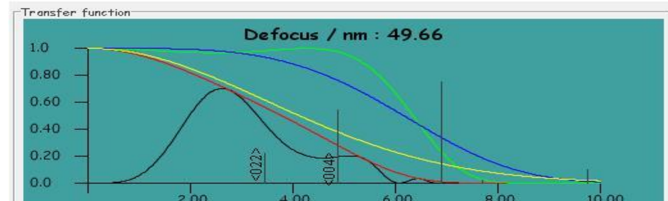

Figure 4.9 Contrast transfer function of JEOL-4000EX at optimal defocus of 49.7 nm. For {001} projected spinel, <022> and <004> reflections are allowed by CTF.

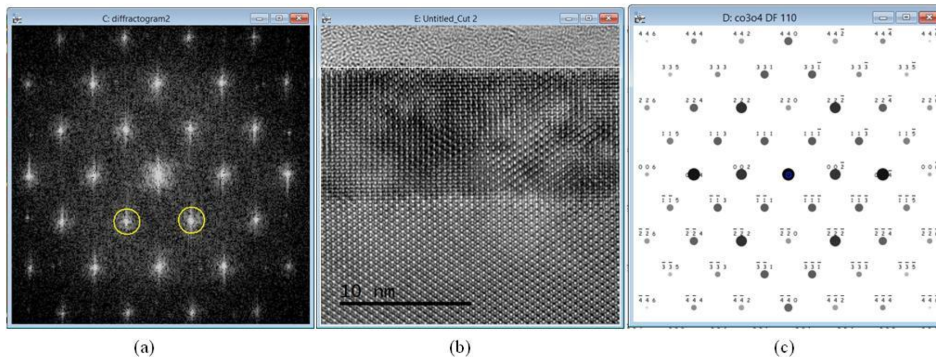

Figure 4.10 (b) Cross-section image in <110> projection used for defect analysis with GPA and Fourier Filtering. (a) and (c) Diffractogram and simulated diffraction pattern.

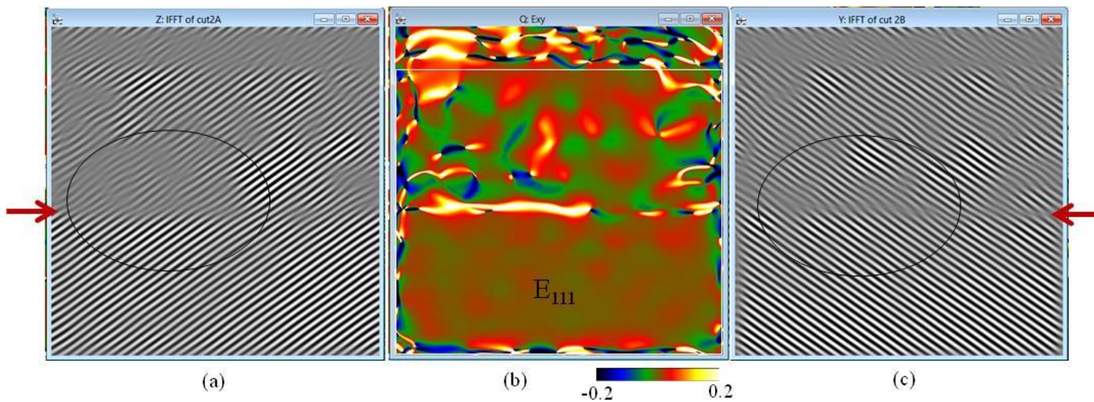

Figure 4.11 (b) x-y strain map using GPA. (a) and (c) Corresponding Fourier-filtered image using {111}Bragg spots. Arrows indicate interface.

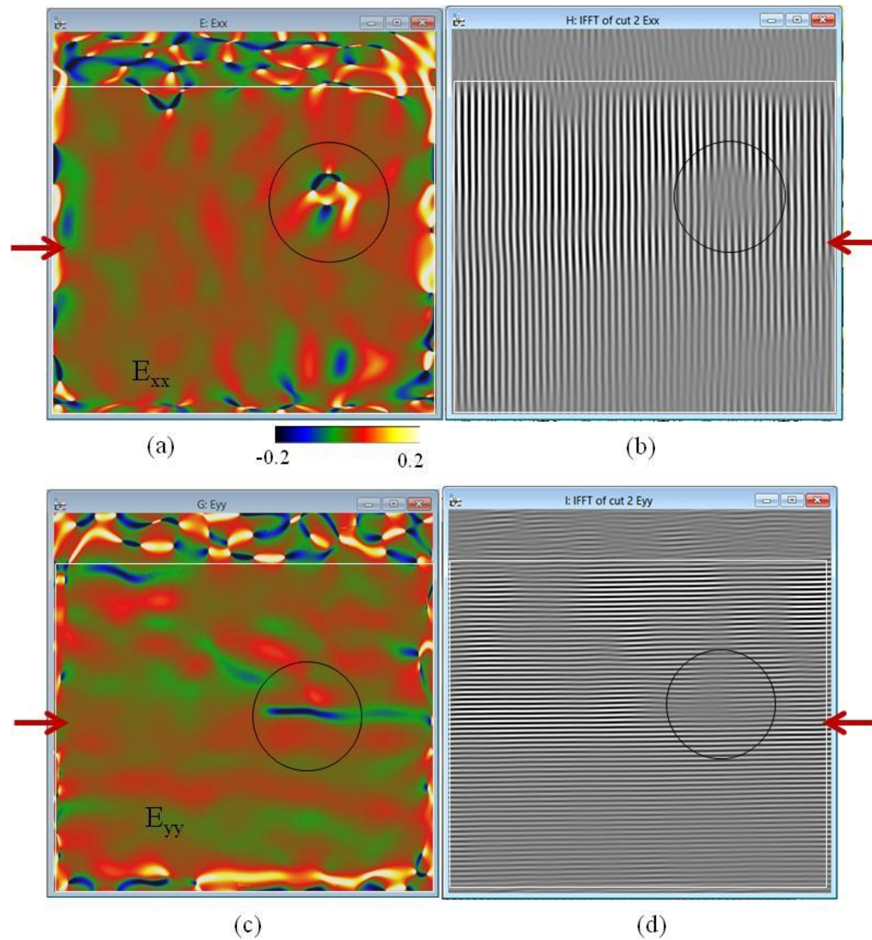

Figure 4.12 (a) and (b) Strain map in x direction (plane of the film) using GPA and corresponding Fourier-filtered image using (002) Bragg. (c) and (d) Strain map in y direction (growth direction) using GPA and corresponding Fourier-filtered image using (022) Bragg spot. Arrows indicate interface.

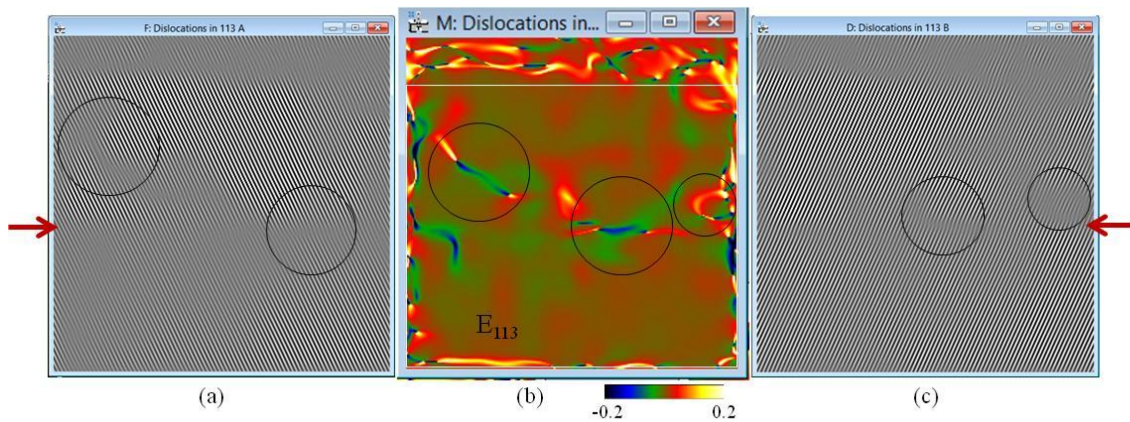

Figure 4.13 (b) Strain map in 113 direction. (a) and (c) Corresponding Fourier-filtered image using {113} Bragg spots. Arrows indicate interface.

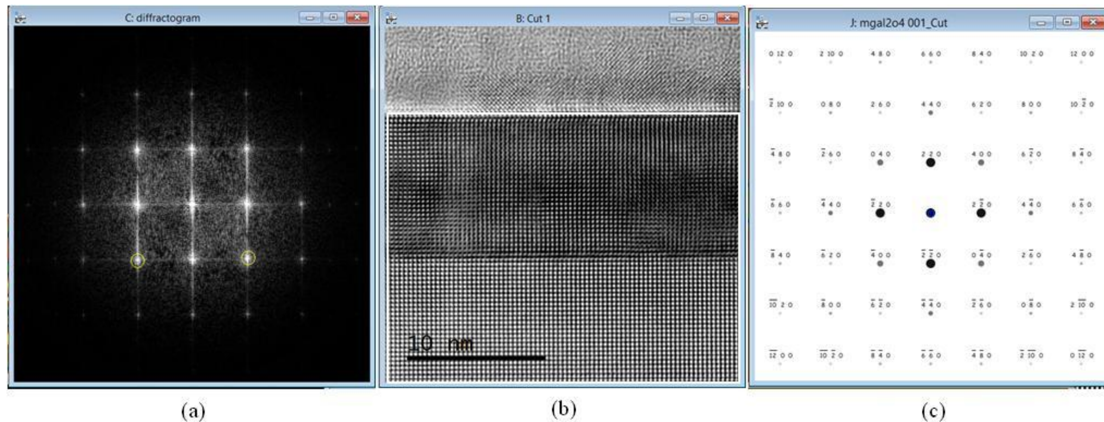

Figure 4.14 (b) is the cross-section in (001) projection used for defect analysis using GPA and Fourier Filtering. (a) and (c) are diffractogram and simulated diffraction pattern.

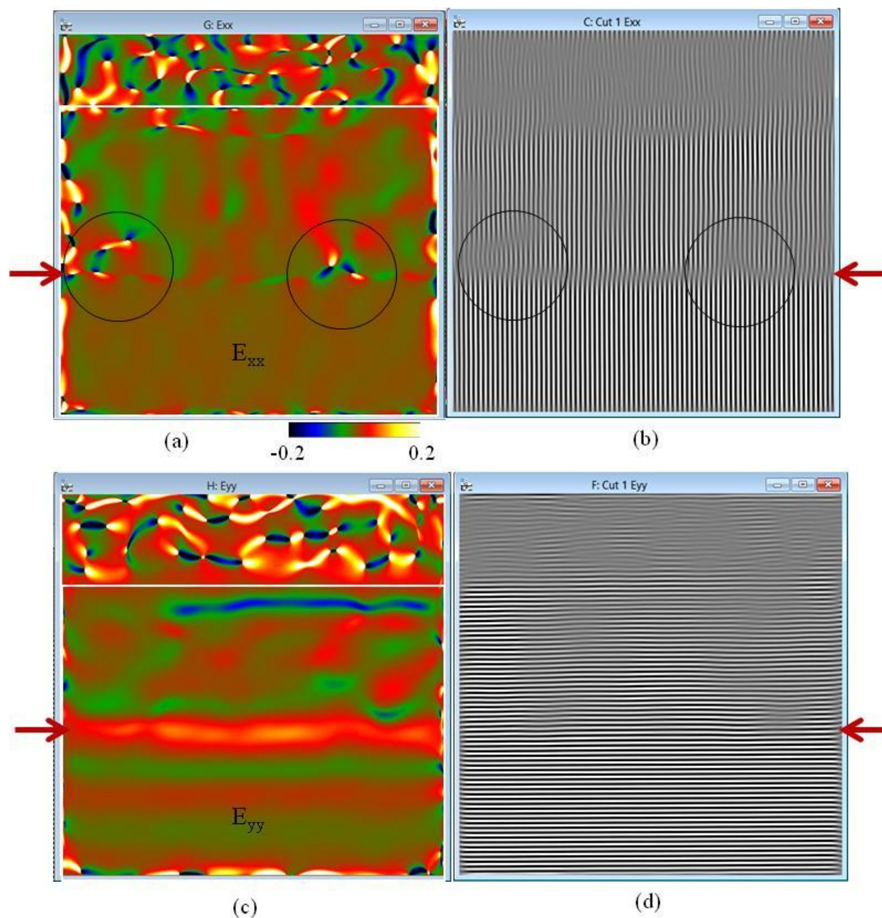

Figure 4.15 (a) and (b) Strain map in x direction (plane of film) using GPA and corresponding Fourier-filtered image using {022} Bragg spot. (c) and (d) Strain map in the y direction (growth direction) using GPA and corresponding Fourier filter image using {022} Bragg spot. Arrows indicate interface.

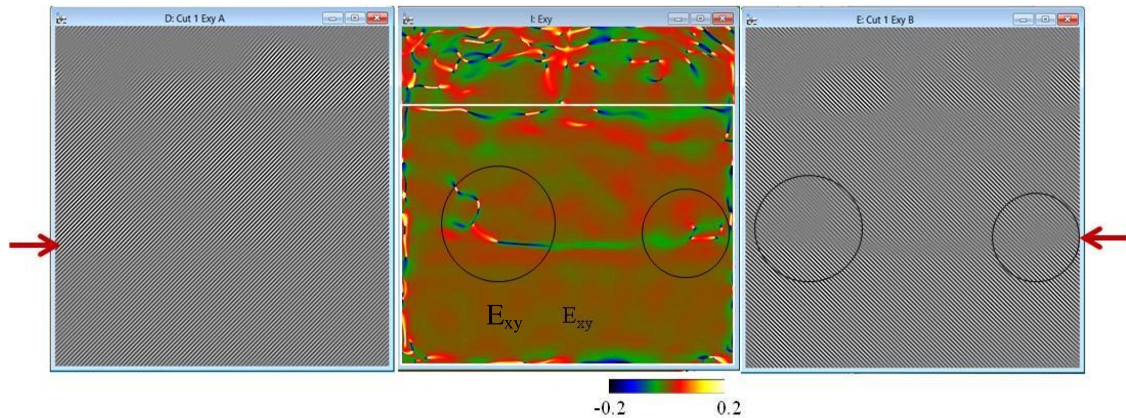

Figure 4.16 (b) Strain map in x-y direction using GPA. (a) and (b) Corresponding Fourier-filtered image using {004} Bragg spots. Arrows indicate interface.

It is clear from figures 4.11, 4.12, 4.13, 4.15 and 4.16, that strain fields are present around the stacking faults. For strain measurements in GPA, the x is in-plane parallel to the film-substrate interface and y direction is out of plane growth direction perpendicular to the substrate. For the {110}-projected sample, as in figure 4.11(a), and for the {100}-projected sample as in figure 4.15(a), strain in the x direction is almost absent at the Co3O4/MgAl2O4 interface. The x-direction in-plane lattice constant of the films is the same as the substrate. However, since the out-of-plane y components of lattice constants tetragonal distortion, strain is clearly present in y-direction, as evident in figures 4.11(c) and 4.15(c). The GPA analysis shows a finite strain field present at the interfaces in 4.11(c) and 4.15(c). Since the lattice constant of Co_3O_4 is slightly smaller than the substrate, a small amount of tensile strain is expected. In addition, figures 4.11 and 4.15 show the presence of dislocations in thin films and near the film/substrate interface.

Both Fourier filtering and GPA revealed that the substrate is almost defect-free and almost strain-free except for regions very close to the film/substrate interface. From

figures 4.11(a), 4.15(a) and 4.15(c) it is clear that the strain fields are quite high close to the stacking faults. The strain fields changed in magnitude over very small length scales suggesting the possibility of the presence of charge, which in spinels would correspond to the absence of electro-neutrality near or at the dislocations. This presence of charges localized near the strain fields could be due to imbalance of Co^{+2} and Co^{+3} and corresponding associated movement of oxygen vacancies [11-12]. The GPA analysis show that the strain components E_{xx} and E_{yy} change from negative to positive and *vice versa* when passing across dislocation cores. It appears that dislocation cores are sources of strain inversion, whereas stacking faults maintain the existing strain status until the next dislocation core is encountered. Since the spinel cation lattice is robust with the anions Co^{2+} and Co^{3+} mobile to accommodate any strain present in the lattice, the strain inversion must be related to charge segregation and /or oxygen deficiency.

It can be anticipated that the presence of tensile strain in the film, and oxygen vacancies in the Co_3O_4 thin films, especially near the film/substrate interface, should affect the Co_3O_4 magnetic properties [13-14]. Magnetization of a Co_3O_4 (110) film was measured as a function of temperature under zero-field-cooled conditions at a constant magnetic field of 1 T oriented in-plane [5]. The field-cooled measurements were in good agreement with the zero-field-cooled values. The data consisted of relatively small signal from the sample and relatively large diamagnetic signal from substrate and sample mounts [5]. Despite the strong diamagnetic background contribution, a local maximum in the magnetization was clearly visible at 49 K, as shown in figure 4.17 [5]. This value is higher than the paramagnetic-antiferromagnetic Neel temperature (T_N) of 30K for Co_3O_4.

The T_N enhancement might possibly be attributed to the tensile strain field created by the slight lattice mismatch between Co_3O_4 and $MgAl_2O_4$. It has been reported that the T_N in antiferromagnetic oxides increases under high pressure [13]. The presence of tensile strain field and presence of non-stoichiometry such as oxygen vacancies at the $Co_3O_4/MgAl_2O_4$ interface, could be responsible here for the higher T_N.

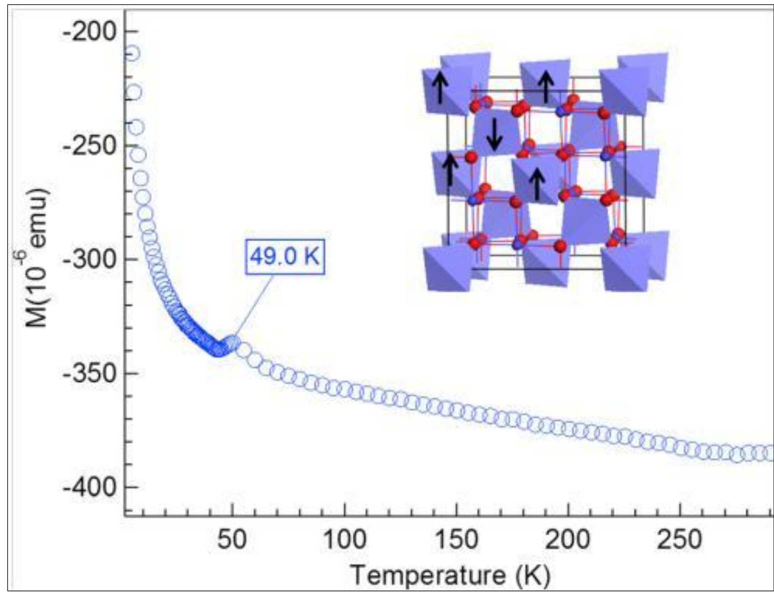

Figure 4.17 Magnetization of a Co_3O_4 (110) film measured as a function of temperature under zero-field-cooled conditions (blue circles) with constant in-plane magnetic field of 1 T. Field-cooled data show similar characteristics. The onset of antiferromagnetism is labeled at 49 K. Inset image shows antiferromagnetic ordering in the spinel structure. The overall negative magnetization is because of the diamagnetic contribution from the substrate [5].

Dislocations are generally associated with cation disorder and vacancies in spinel materials. The presence of cation disorder was observed in the ellipsometry study [5]. The experimental ellipsometric curves for $Co_3O_4/MgAl_2O_4$ did not fit well with the theoretical models especially at low phonon energies below 400 cm^{-1}. Broadening of the experimental curves has been reported [15]. The broadening of TO peaks and lack of

their agreement with theoretical models has been attributed to cation disorder in spinel materials and surface/interface damage of spinel thin films [15].

Hornstra et al (1960) predicted that dislocation glide on (111) spinel planes are rarely observed for non-stoichiometric crystals at low temperatures [13]. {1 1 1} glide in non-stoichiometric crystals requires higher resolved shear stress than (110) glide. The main arguments in favor of (111) glide are based on the reduction in strain energy of a dislocation by its possible dissociation into partials only when parallel to close-packed (111) planes and deviation from electrical neutrality for dislocations gliding on {110}. Spinels contain cations of differing valence in (110) planes, and any dislocation gliding along this direction, would give rise to electrical charges. Kronberg et al (1957) suggested that (111) glide of partial dislocations involves the synchronous movement of cations, in interstices at the dislocation core, in directions at 60° to the anion motion. This model is applicable to systems such as spinels where very large numbers of interstitials are available for cations involved in the dislocation glide to move into normally vacant interstices during glide [11].

The electroneutrality criterion is not predominant for non-stoichiometric spinel, but the high energy for an oxygen ion fault precludes dissociation into partials necessary for glide along (111) [16]. Additional evidence lies in the frequent cross-glide of dislocations on (111) planes. Deformation in non-stoichiometric spinel crystals occurs predominantly by the glide of coupled partial dislocations with collinear Burgers vectors in (110) planes. The cation stacking fault separating the two partial dislocations is characterized by cations in tetrahedra and octahedra with a common face, which

represents a deviation from the unfaulted lattice in which occupied tetrahedral and octahedral sites share only two common oxygen ions (the tetrahedra and octahedra have a common edge). The stacking fault energy arises from such a deviation in which cations are in closer proximity than for the unfaulted lattice. It appears that the presence of an increasing number of +3 ions and charge-compensating vacancies reduces the fault energy to such an extent that an observable change of stacking-fault ribbon width occurs with deviation from stoichiometry. The marked increase in strain for crystals near the stoichiometric composition may be attributed to decreasing mobility of partial dislocations on {110} planes resulting from an increasing difficulty in maintaining charge neutrality at the dislocation core, when the cation vacancy concentration decreases, and a modification in the strain field of adjacent partial dislocations with decreasing separation. It is possible that dislocation motion along {111} planes is predominant for stoichiometric crystals, which have comparatively high stresses [17]. Hence, it is clear that for non-stoichiometric spinels at low temperatures, the dislocation mobility on (111) or (100) systems is low in comparison with (110), and the flexibility of glide is further limited by the difficulty of glide band intersections for oblique systems (interacting (111) planes) [16-19].

In addition to interfaces which preserve the cation molarity ratio, it has been shown that interfaces occur which do not intrinsically preserve composition and which probably involve local cation rearrangement during their formation. Such observations thus emphasize the role of cation rearrangement at an internal interface in a oxide material and suggest that such rearrangements permit formation of otherwise unstable

configurations [20-23]. This explains our conclusion about the observation of thermodynamically unfavorable type B- Al_2O_4 terminated interface.

No signs of a metallic response were observed [5], which would lead to discrepancies between our lattice dynamical model and the data at low frequencies. Thus, we were unable to investigate a two-dimensional electron gas, which might be present at the interface between Co_3O_4 and $MgAl_2O_4$. No signs of free carriers due to doping in the Co_3O_4 layer were found [5].

4.5 Conclusions

In conclusion, the structure of the $Co_3O_4/MgAl_2O_4$ (110) interface has been identified. The interface is of type B, in which the $MgAl_2O_4$ substrate is terminated with Al and oxygen when sample projection is [011]. Stacking faults were found along [111], [001] and [113] with glide planes in {110} and {111}. GPA analysis agreed very well with the presence of strain fields associated with dislocations. The $Co_3O_4/MgAl_2O_4$ interface was under obvious strain very close to the interface. The presence of dislocations indicated cation disorder and associated oxygen vacancies. These results provide motivation for future study of this material system, including HRSTEM/EELS study to determine atomic positions at the interface and surface. Further studies of different combinations of thin film/substrate spinel are needed to understand the effects of interface structure on the magnetic properties of spinel heterostructures.

References

1. H. St. C. O'Neill and A. Navrotasky, American Mineralogist, (1983) Volume 6, pp. 181-194.

2. K. E. Sickafus, J. M. Wills and N. W. Grimes, J. Am. Ceram. Soc., (1999) 82 [12] 3279–92.

3. S.T. Murphy, C.A. Gilbert, R. Smith, T.E. Mitchell, and R.W. Grimes, Philosophical Magazine, (2010) 90:10, 1297–1305.

4. S. C. Petitto and M. A. Langella, J. Vac. Sci. Tech. A 22 (4) Jul/Aug 2004, 1690-96.

5. K. J. Kormondy, A. B. Posadas, A. Slepko, A. Dhamdhere, D. J. Smith, K. N. Mitchell, T. I. Willett-Gies, S. Zollner, L. G. Marshall, J. Zhou, and A. A. Demkov, Journal of Applied Physics. (2014) 115, 243708.

6. C. A. F. Vaz, V. E. Henrich, C. H. Ahn, E. I. Altman, Journal of Crystal Growth (2009) 311, 2648–2654.

7. C. A. F. Vaz, H. Q. Wang, C. H. Ahn, V. E. Henrich, M. Z. Baykara, T. C. Schwendemann, N. Pilet, B. J. Albers, U. D. Schwarz, L. H. Zhang, Y. Zhu, J. Wang, E. I. Altman, Surface Science (2009) 603, 291–297.

8. H. Hayashi, R. Huang, F. Oba, T. Hirayama and I. Tanaka, J Mater Sci (2011) 46: 4169–4175.

9. M. H. Lewis, Philosophical Magazine, (1968) 17:147, 481-499.

10. M. Hytch, F. Snoeck, and R. Kilaas, Ultramicroscopy 74 (1998) 131-146.

11. J. Hornstra, J. Phys. Chem. Solids, (1960) 15, 311-323.

12. C. B. Carter, Z. Elgat and T. M. Shaw, Philosophical Magazine A, (1987) 55 (1) 1-19.

13. C. Gatel, B. Warot-Fonrose, S. Matzen, and J. B. Moussy, Applied Physics Letters, (2013) 103, 092405.

14. N. Li, S. Schäfer, R. Datta, T. Mewes, T. M. Klein, and A. Gupta, Applied Physics Letters, (2012) 101, 132409.

15. C. J. Zollner, T. I.Willett-Gies, S. Zollner, S. Choi, Thin Solid Films 571 (2014) 689–694.

16. T. Muschik and M. Ruhle, Philosophical Magazine, (1992) 65 (2) 363-388.

17. H. Sieber, P. Werner & D. Hesse, Philosophical Magazine A, (1997) 75 (4) 909-924.

18. F. Ernst, P. Pirouz & A. H. Heuer, Philosophical Magazine A, (1991) 63 (2) 259-277.

19. S. Matzen, J. B. Moussy, R. Mattana, K. Bouzehouane, C. Deranlot, F. Petroff, J. C. Cezar, M.-A. Arrio, Ph. Sainctavit, C. Gatel, B. Warot-Fonrose, and Y. Zheng, Physical Review, (2011) B 83, 184402.

20. N. J. van der Laag, C. M. Fang, and G. de With, G. A. de Wijs, H. H. Brongersma, J. Am. Ceram. Soc., (2005) 88 (6) 1544–1548.

21. R. Schweinfest, S. Köstlmeier, F. Ernst, C. Elsäser, T. Wagner & M. W. Finnis, Philosophical Magazine A, (2001) 81 (4) 927-955.

22. H. Sieber , D. Hess & P. Werner, Philosophical Magazine A, (1997) 75 (4) 889-908.

23. C. M. Fang, S. C. Parker and G. de With, J. Amer. Ceram. Soc., (2000) 83 [8] 2082–84.

CHAPTER 5

HETEROEPITAXY ON OXIDE SUBSTRATES

5.1 Niobium Oxide Thin-Films on STO (111) and LSAT (111)

5.1.1 Introduction

Many tetragonal oxide materials undergo metal-to-insulator transitions (MIT) as a function of temperature, pressure, and electric field. MIT is in general associated with a structural phase transition [1-5]. Applications for MIT materials include gas sensors, resistive random access memory devices, and electronic switches. For many electronic applications, it is desirable that the transition temperature be close to but above room temperature to isolate field and temperature switching. A oxide VO_2 undergoes a phase transition from rutile to a distorted rutile phase at ~ 340 K [4-5]. However, utilizing this MIT transition in VO_2 in devices for practical applications faces two potential challenges: first, the VO_2 transition temperature of 340K is too low for reliable device operation, and second, the insulating phase has a relatively narrow band gap of 0.67 eV [4-5].

A structurally close material, niobium dioxide NbO_2, also exhibits MIT accompanied by a structural transition to a distorted rutile phase at 1081 K [1-3, 6-10]. This high MIT transition temperature is beneficial for extending the possible temperature range of applications. The application of NbO_2 to electrical switching and memory devices has been reported [1]. Electronic properties of 4d transition metal Nb and Nb oxides are quite intriguing and are strongly dependent on the oxidation state of Nb. For

example NbO is metallic and become a superconductor at transition temperature ~ 9.2 K, NbO_2 is semiconducting, and Nb_2O_5 is insulator with excellent dielectric properties [11].

Using electric-controlled MIT in actual devices require oxides in thin film media form [4-5]. Epitaxial films are particularly interesting because of their high crystal quality and the possibility of utilizing the crystal anisotropy of their physical properties. For isostructural epitaxial growth of tetragonal rutile phase such as NbO_2, the only commercially available oxide substrate is rutile TiO_2, limiting the number of possible heterostructure combinations. On the other hand, nonisostructural film-substrate combinations offer vastly more options and functionalities. In this case of the surface symmetry and lattice matching at the heterointerface are quite complicated [4-5].

For electronic devices utilizing NbO_2 as a channel material in transistors, the dimerization direction (001) should be in the plane of the film [1]. Hence better in-plane electrical transport properties can be achieved with epitaxial NbO_2 thin-films. BCT-rutile NbO_2 (100) plane contains the face of the distorted Nb-O octahedron, which is approximately three-fold symmetric. Hence, it is possible to grow epitaxial NbO_2 with the rutile *c*-axis in-plane by growing on substrates with hexagonal/ trigonal symmetry [4-5]. Earlier reports of MBE-grown epitaxial NbO_2 on *c*-plane sapphire and $LiNbO_3$ showed growth of NbO phase with some presence of NbO_2 [1]. Additional oxygen pressure during growth leads to Nb_2O_5. Hence, oxygen control during film growth is very critical in order to obtain phase-pure material, especially for the intermediate oxidation state NbO_2. Various Nb oxides can be easily transformed into each other by oxygen/vacuum annealing [1, 11].

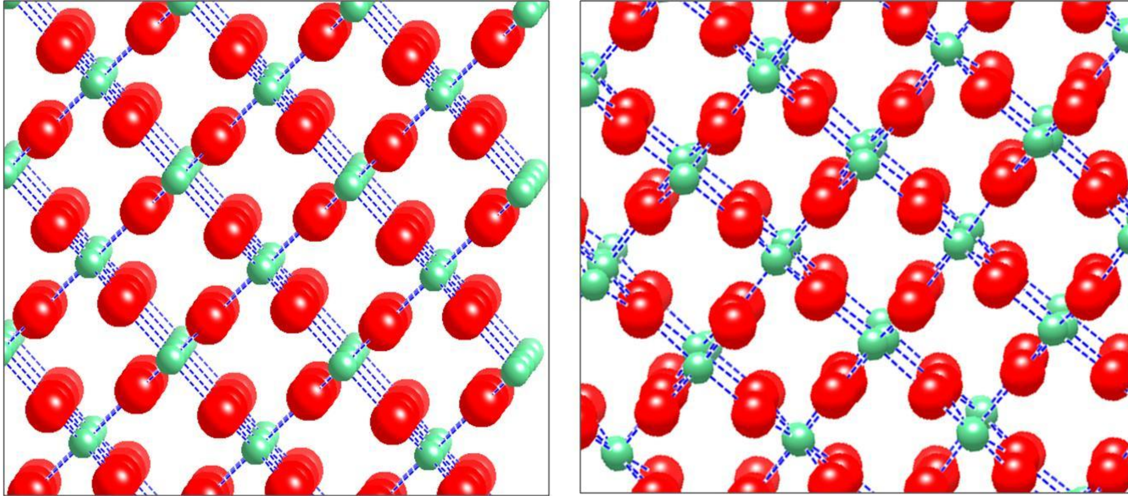

Figure 5.1 (a) NbO2 tetragonal Rutile structure at high temperatures and (b) BCT tetragonal distorted Rutile structure with neighboring Nb atoms forming dimers along the c-axis. Both crystal structures are in [001] projection.

At temperature above 1081 K, NbO_2 has a true tetragonal rutile-phase structure (P42/mnm) with lattice constants of *a*=*b*=4.846 Å and *c*=3.035 Å [7-9]. This is depicted in figure 5.1 (a). Below 1081 K, the NbO_2 crystal structure becomes a distorted rutile structure (I41/a) described as body-centered tetragonal (BCT) having lattice constants *a*=13.702 Å and *c*= 5.985 Å. This structural transformation is associated with corresponding MIT in NbO_2. The metallic phase of BCT NbO_2 is due to temperature-driven dimerization of Nb atoms forming a bonding state between the Nb d_{xy} orbitals as shown in figure 5.1 (b). The strong conductivity change occurs along the dimerization direction (rutile c-axis 001) [6-10].

5.1.2 Experimental Work

In this work, the epitaxial thin films of phase-pure NbO_2 films were grown on $SrTiO_3$ (STO) (111) and $(La,Sr)_2(Al,Ta)_2O_6$ (LSAT) (111) substrates using molecular beam epitaxy (MBE). NbO_2 MBE consisted of electron beam evaporator for the niobium metal source and molecular oxygen as the oxidant at 610 Torr with substrate temperature of 750°C. Substrate temperature was ramped up and down and kept at 750°C continuously under steady oxygen flow. Substrates were pre-heated to 600°C to remove possible substrate out-gassing. Once the oxygen flow and substrate temperature reached steady state values, Nb shutter was opened to get desired thin film thickness. Films were also grown on STO (111) and LSAT (111) substrates using the same growth conditions.

The Reflection High Energy Electron Diffraction (RHEED) analysis indicated that the NbO_2 film grown on STO is highly crystalline, with 60° azimuthal rotation pseudo-six-fold symmetry of the film and lattice spacing of c~6.0 Å, very close value to that of the distorted rutile phase. The x-ray diffraction (XRD) confirmed that the NbO_2 films have a single out-of-plane orientation with a d-spacing of 2.44 Å, which is slightly larger than one-half of the (100) interplanar spacing of the pseudo-rutile phase. Hence RHEED and XRD proved that the NbO_2 films grow with pseudo-rutile (100) orientation out-of-plane and with three symmetry-equivalent rotational domains in-plane. The x-ray photoelectron spectroscopy (XPS) revealed that the NbO_2 films were slightly oxygen-deficient as-grown and showed the presence of both NbO and NbO_2. Samples annealed under higher oxygen pressure resulted in the formation of Nb_2O_5 phase.

In this work, NbO_2 thin films deposited on STO (111) and LSAT (111) were studied using transmission electron microscopy to determine the thin film phase, the crystalline quality, film orientation and lattice parameters, and film-substrate interface. Cross-sectional TEM samples were prepared using conventional mechanical polishing and dimple grinding followed by precision ion milling at ~ 3.5 keV to achieve final thickness for electron transparency. The samples were studied using the JEOL JEM 4000EX electron microscope operated at 400 keV with C_s = 1.0 mm yielding structural resolution of ~ 1.7 Å. HRTEM images were obtained with imaging conditions as Scherzer defocus, spherical aberration coefficient of C_s= 1.0 mm, half-convergence angle of 0.6 mrad and defocus spread of 6 nm. All images were taken very close to the Scherzer defocus. HRTEM images and diffractograms obtained from experimental images were compared with simulated images and diffraction patterns to obtain crystal structure. The simulations were made using the commercial image simulation program JEMS. Same imaging parameters were used in simulations.

5.1.3 Determining Crystal Structure of NbO_2/STO (111)

Figure 5.2 (a) show HRTEM micrograph of NbO_2 deposited on STO (111). Figure 5.2 (b) and (c) are magnified view of a cross-section cut made from 5.2 (a), and diffractogram obtained from image 5.2 (b), respectively. The HRTEM micrographs show formation of high crystalline quality NbO_2 films. Presence of grain boundaries was also observed. Diffractogram clearly has diffraction spots from substrate and thin film. By selectively applying mask to diffraction spots of the substrate STO, the substrate contribution to the diffractogram was removed, as shown in figure 5.2 (d).

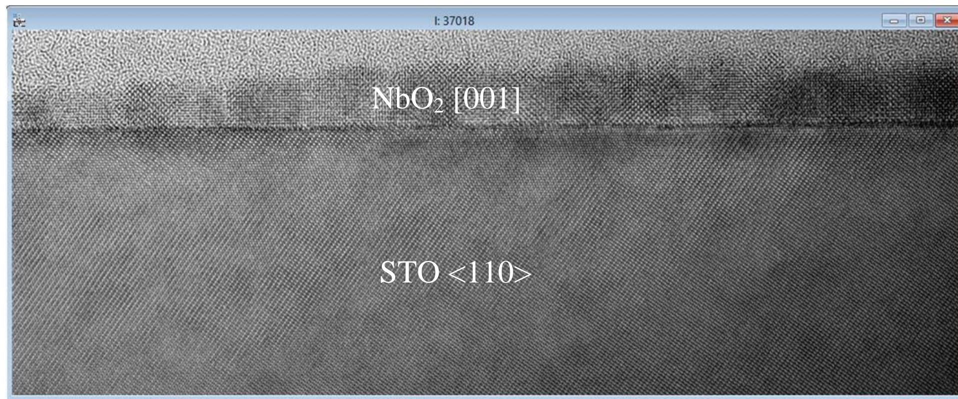

(a)

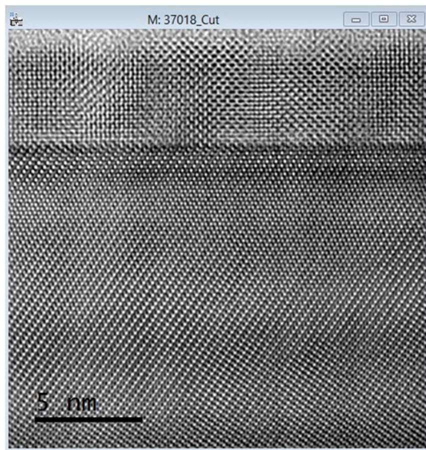

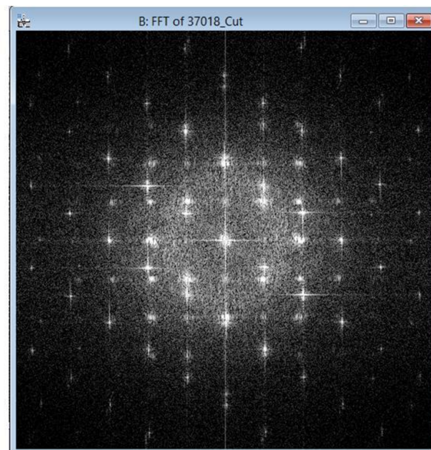

(b) (c)

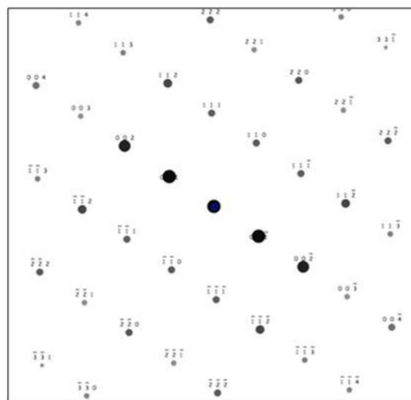

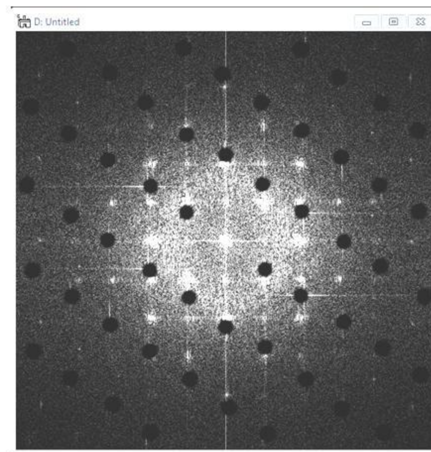

(d) (e)

Figure 5.2 (a) is a HRTEM micrograph of NbO2/STO (b) is a cross-section of sample (c) is a diffractogram of HRTEM image in (b), (d) is a simulated diffraction pattern of substrate STO in <110>, (e) is diffractogram in (d) with STO mask applied

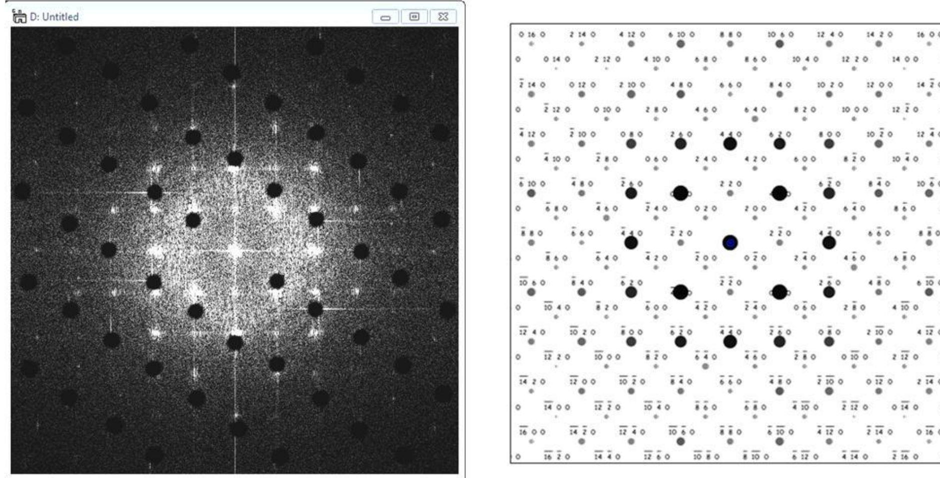

Figure 5.3 Diffractogram from film after subtracting diffraction pattern of substrate matches exactly with simulated diffraction pattern of BCT NbO_2 [001]

Earlier RHEED analysis suggested growth of *a*-axis oriented NbO_2 on STO (111). Hence assuming that the NbO_2 films in our sample were a-axis [100] oriented grown on STO (111), in the cross-section shown in figure 5.2, the substrate is projected in <110> and NbO_2 films are [001] projected.

Orientation of thin films was confirmed by simulating the diffraction pattern of NbO_2 in [001], [010], [100] and <110> projections and matching the simulated patterns with experimental diffractograms. As evident in figure 5.2 (e), the diffraction pattern from film matches almost exactly with the simulated diffraction pattern of BCT NbO_2 in [001] projection. This means that the in-plane [001] direction of NbO_2 is aligned to the in-plane <110> direction of the STO substrate. By comparing the experimental diffraction pattern with simulated diffraction pattern in figure 5.2, the lattice parameter was determined. Scaling in the diffractograms was done using substrate STO (a=3.905) 001 spots. The 220 and 2-20 spots of NbO_2 yields a= 13.81 Å and using 040 and 400

spots of NbO_2 *a*=13.78 Å. These values are in good agreement with value of *a*= 13.71 Å obtained by Neutron Diffraction experiments for BCT NbO_2 (space group I41/a) [6-7].

The crystal models for NbO_2 and STO were imported into the image simulation software program JEMS and HRTEM images were then simulated using the multislice module. The imaging conditions chosen were very close to those used for experimental observation with the JEOL JEM 4000EX: operating voltage of 400 kV, Scherzer defocus of -49 nm, spherical aberration coefficient of C_s= 1.0 mm, half-convergence angle of 0.5 mrad and defocus spread of 6 nm. Although the experimental images were obtained close to Scherzer defocus of -49 nm, the exact sample thickness and defocus values of the experimental images were not exactly known. Hence, thickness-defocus series were calculated (not shown here) to create an array of images with different defocus and thickness values. Every image was then matched with the experimental image to identify the best match. Near Scherzer defocus, the bright spots in the simulated and experimental images represent the positions of oxygen columns. The darker spots correspond to the positions of the Nb or Sr or Ti columns.

Figure 5.4 is an experimental cross-section placed next to simulated images from crystal models. The thin film-substrate interface appears rather complicated and needs careful consideration of bonding. Based on image simulations the proposed interface model is shown in figure 5.5.

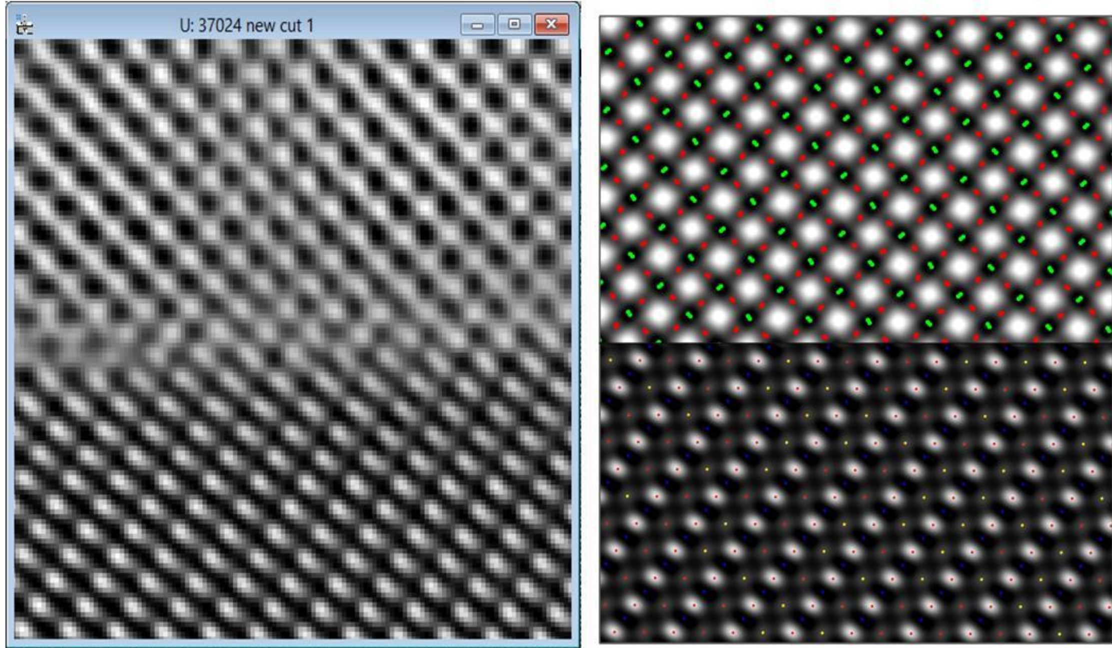

Figure 5.4 Experimental image of NbO2-STO interface placed next to simulated images of NbO2 [001] and STO <110> projected crystals models. Atom columns are shown in simulated images.

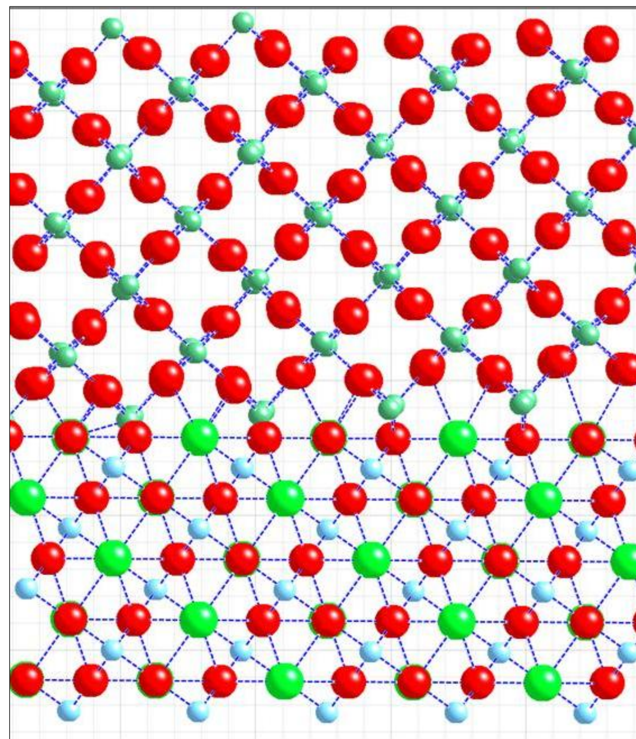

Figure 5.5 NbO_2 [001]-STO <110> Interface proposed model

5.1.4 Determining Crystal Structure of NbO/LSAT (111)

Similar to NbO_2/STO (111) system, growth of distorted rutile BCT NbO_2 [100] is expected on LSAT (111). However, the observed NbO_x phase was not of BCT type but rather of the cubic rocksalt (Pm-3m) structure type. Figure 5.6 (a) is HRTEM micrograph of NbO_x on LSAT (111) obtained by electron microscope JEM 4000EX operated at same operating conditions. Figure 5.6 (b) and (c) are magnified views of a cross-section cut made from 5.6 (a) and diffractogram obtained from image 5.6 (b) respectively. The HRTEM micrographs show formation of high crystalline quality NbO_x films. Presence of grain boundaries was also observed along with probable occurrence of grain rotations. Diffractogram clearly has diffraction spots from substrate and thin film. Earlier RHEED analysis suggested growth of *a*-axis oriented NbO_2 on LSAT (111). But contrary to this observation, it was observed that the NbO_x film was of rocksalt structure and possibly [111] axis grown following the (111) surface symmetry of the substrate.

In the figure 5.6 (b), film projection is <110> same as substrate. This orientation was obtained by simulating the diffraction pattern of BCT NbO_2 in [001], [010], [100], <110> projections, high temperature rutile NbO_2 phase in [001], [010], [110], <110> projections and finally rocksalt NbO phase in [001], [010], [110], <110> projections and then matching all the simulated diffraction patterns with experimental diffractogram. By selectively applying mask to diffraction spots of the substrate LSAT, the substrate contribution to the diffractogram was removed, as shown in figure 5.6 (d).

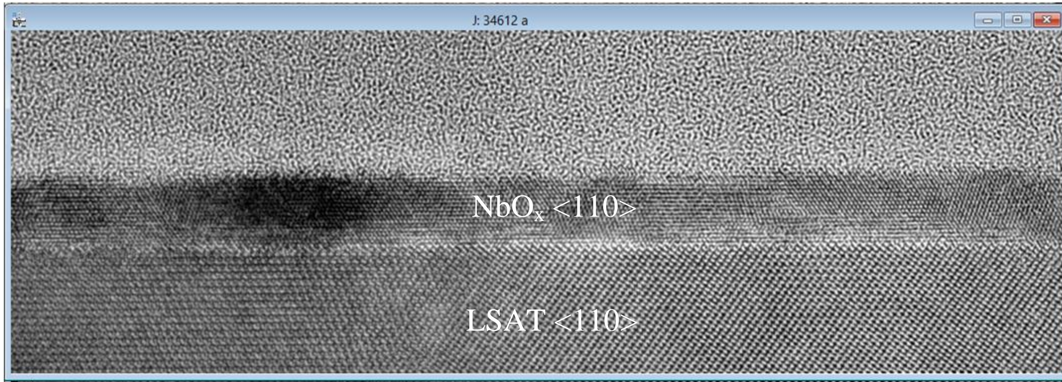

(a)

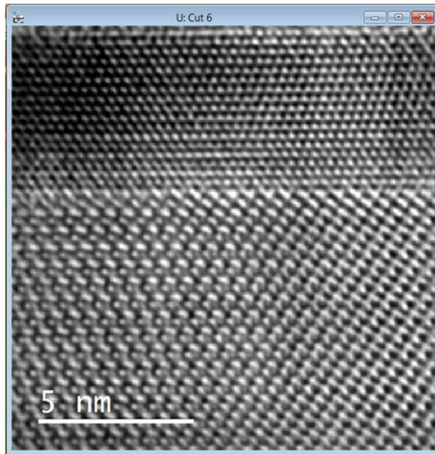

(b)

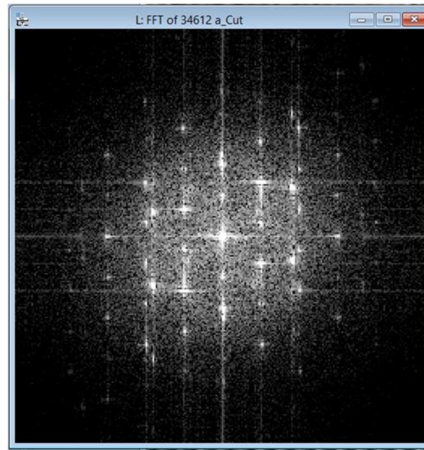

(c)

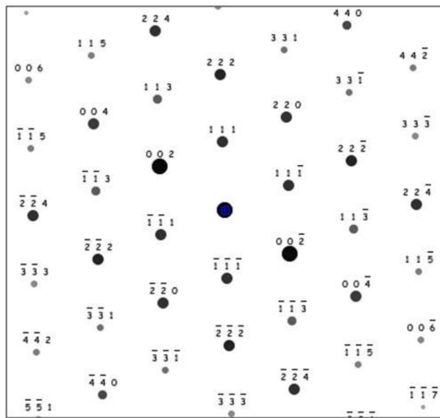

(d)

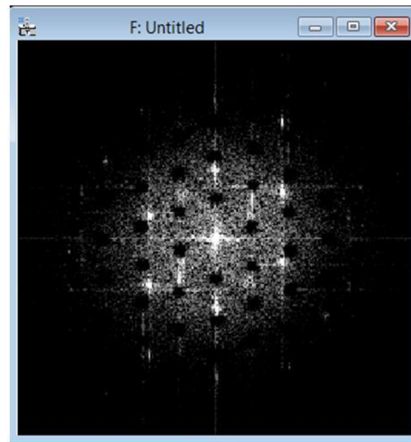

(e)

Figure 5.6 (a) is a HRTEM micrograph of NbOx/LSAT system (b) is a cross-section of sample (c) is a diffractogram of HRTEM image in (b), (d) is a simulated diffraction pattern of substrate LSAT in <110>, (e) is diffractogram in (d) with STO mask applied

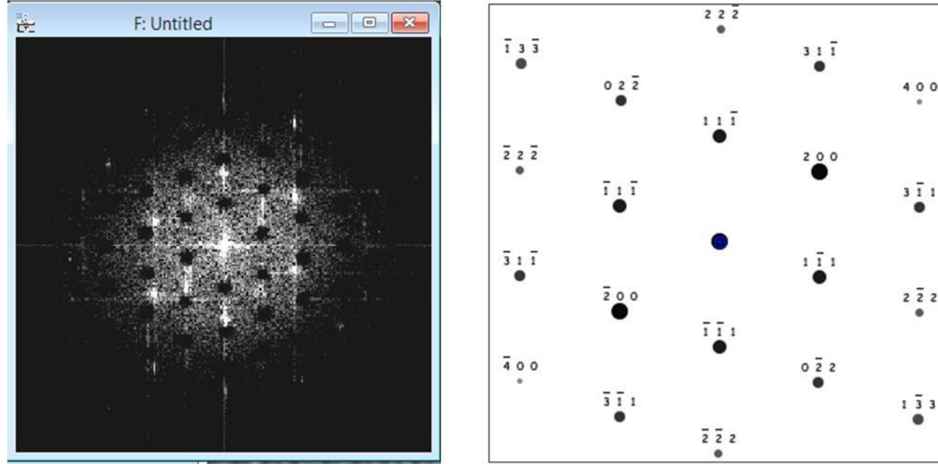

Figure 5.7 Diffractogram from film after subtracting diffraction pattern of LSAT substrate matches exactly with simulated diffraction pattern of cubic NbO <110>

As evident in figure 5.6 (e), the diffraction pattern from the film matches almost exactly with the simulated diffraction pattern of cubic rocksalt NbO in <110> projection. This means that the in-plane <110> direction of NbO is aligned to the in-plane <110> direction of the STO substrate. Oxygen deficiency and presence of NbO and with NbO_2 was reported for this samples. High substrate temperature of 750 ^{o}C during growth could be contributing factor for cubic NbO growth [1, 11].

By comparing the experimental diffraction pattern with simulated diffraction pattern in figure 5.7, the lattice parameter of the thin film was determined. In the diffractogram, scaling was done using LSAT substrate (assuming pseudo-cubic structure with *a*=7.735Å) 002, 111 and 202 spots. The 200 spots of NbO yielded *a*= 4.22 Å, using the 111 spots of NbO *a*= 4.26 Å was obtained, and using 311 spots of NbO *a*=4.31 Å was obtained. Hence the average value of *a*= 4.26 Å was observed to be in good agreement with value of *a*= 4.25Å reported in literature [11].

In order to ensure that the cubic NbO phase is present in this sample, the crystal models for NbO and LSAT were imported into the image simulation software program JEMS. HRTEM images were then simulated using the multislice module of JEMS. The imaging conditions chosen were very close to those used for experimental observation with the JEOL JEM 4000EX: operating voltage of 400 kV, Scherzer defocus of -49 nm, spherical aberration coefficient of C_s= 1.0 mm, half-convergence angle of 0.5 mrad and defocus spread of 6 nm. Although the experimental images were obtained close to Scherzer defocus, the exact sample thickness and defocus values of the experimental images are not exactly known. Hence, thickness-defocus series were calculated (not shown here) to create an array of images with different defocus and thickness values. Every image was then matched with the experimental image to identify the best match.

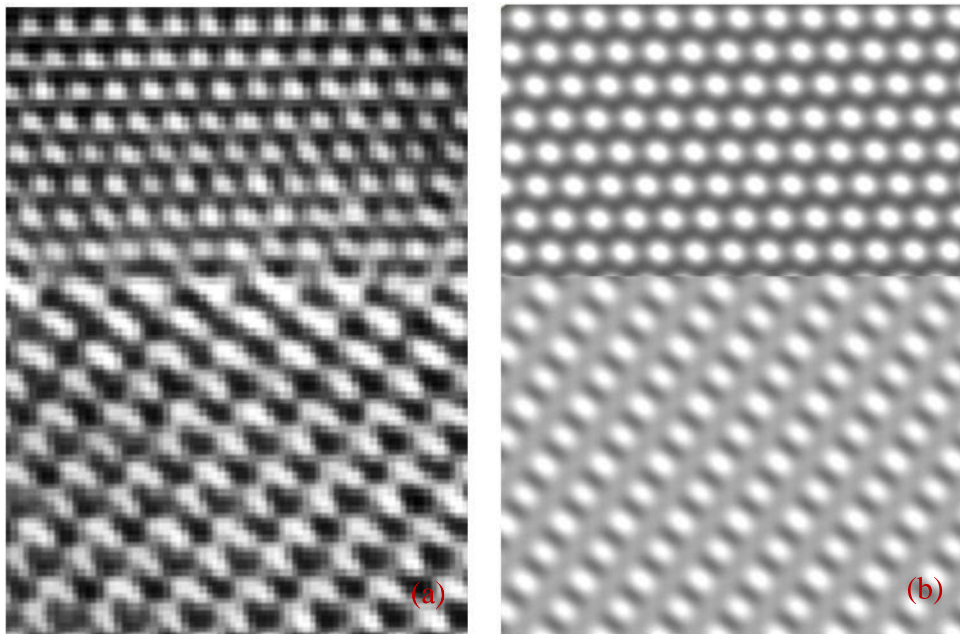

Figure 5.8 Experimental image of NbO-LSAT interface (a) placed next to simulated images (b) of NbO <110> and LSAT <110> projected crystals models.

Near the Scherzer defocus, the bright spots in the simulated and experimental images represent the positions of oxygen columns. The darker spots correspond to the positions of the Nb or Sr or La or Ta columns. Figure 5.8 is an experimental cross-section placed next to simulated images from crystal models. The thin film-substrate interface is rather complicated and again needs careful consideration of bonding. Based on image simulations, the proposed interface model propose is shown in figure 5.9. Since the cubic rock-salt structure thin films of NbO were deposited on perovskite substrate LSAT(111), we can expect to observe nano-size grains rotated relative to each other. Figure 5.10 shows two grains with different orientations in projected direction. The grain boundary walls are not straight possibly due to lack of columnar growth.

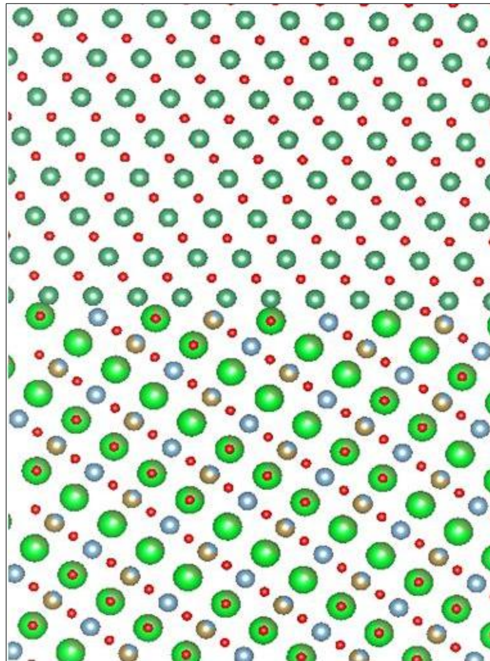

Figure 5.9 Based on image simulations the interface model for NbO/LSAT system we propose is shown.

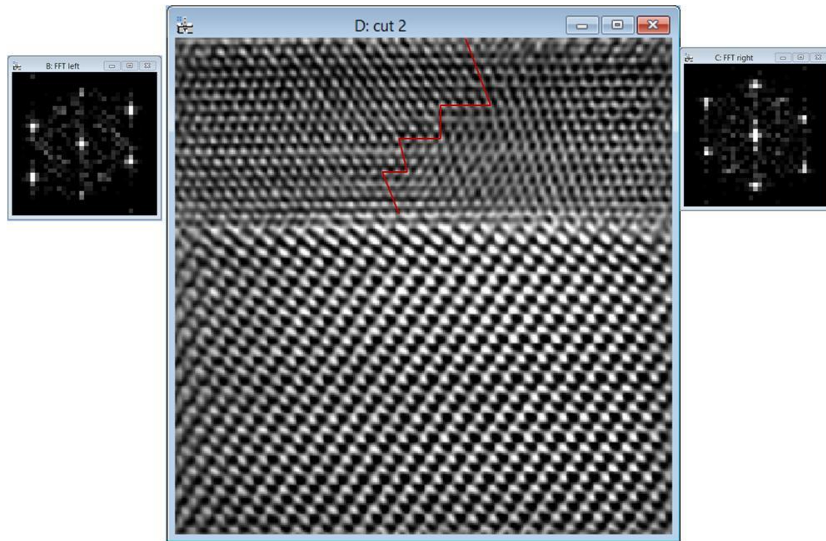

Figure 5.10 Show adjacent grains with different orientations as shown in diffractograms from two regions of NbO thin film.

5.2 Intermetallic Zintl Aluminide Thin-Films on LAO (100)

5.2.1 Introduction

Zintl phases are a class of intermetallic materials that posses simultaneous ionic and covalent bonding resulting from charge transfer between two different atomic species. Zintl materials in general are represented by the form $A_aX_x = (A^{n+})_a[X^{(an/x)-}]_x$, where A is an alkali/alkaline earth metal of group 1 or 2 of periodic table and X is an electronegative metal or semimetal of group 13-15 [12]. The Zintl-Klemm concept describes chemical bonding in semimetallic and semiconducting valence compounds. According to the concept, the electro-positive active metal A donates valence electrons to the electronegative metal X, which in turn forms a sublattice with covalent character typical for the isovalent element. The charge transfer gives ionic character to Zintl phases hence effectively combining both bonding mechanisms in one material [12].

The Zintl phase studied in this work, $SrAl_4$, has a tetragonal structure with space group I4/mmm with lattice constants $a = b = 4.46Å$ and $c = 11.21Å$. A unit cell consists of two Sr atoms and eight Al atoms [13]. The structure of $SrAl_4$ is shown in figure 5.11. Two types of Al atoms one with tetragonal symmetry with four nearest neighbors and other with five nearest neighbors exist in $SrAl_4$. The type 1 aluminum with the tetrahedral symmetry is very similar to sp^3 hybridized silicon with four valence electrons. According to Zintl-Klemm concept, aluminum with three valence electrons receives one electron transferred from strontium and can bond in sp^3 hybridized orbitals [12].

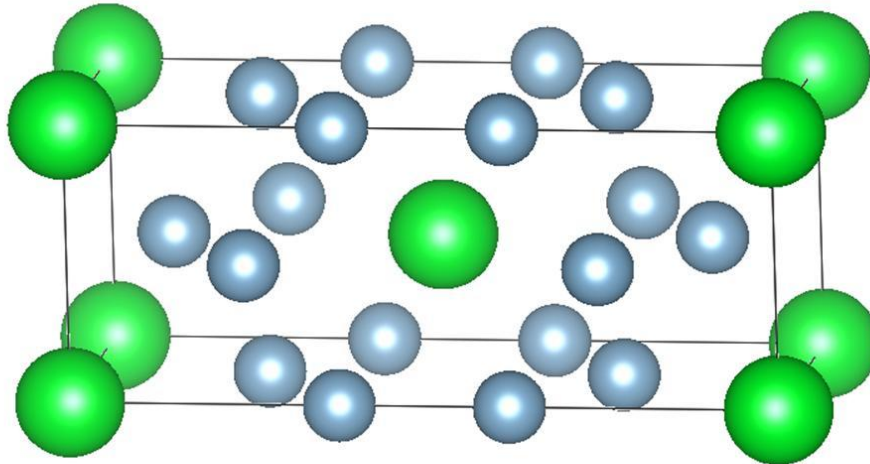

Figure 5.11 A unit cell of $SrAl_4$ with Sr (green) and Al (blue)

Presences of covalent and ionic bonding have made the Zintl phases very interesting with potential applications in thermoelectrics [14], topological insulators [15], and heteroepitaxial buffer layers for dissimilar materials [16-18]. The most challenging aspect of the epitaxial integration of functional oxides with semiconductors is the abrupt change of the nature of the chemical bonding across the interface, which often disrupts epitaxy. The interface between covalently bonded semiconductors and polar covalent

with strong ionic nature of perovskite oxides has high interfacial energy. This high interfacial energy makes substrate wetting less likely and often prevents the desired layer-by-layer growth. One of the most significant developments in the growth of oxides on semiconductor substrates was the use of Zintl phase $SrSi_2$ of thickness of one-half monolayer to grow epitaxial $SrTiO_3$ on silicon substrates. The Zintl-Klemm phases in between interface of oxides and semiconductors enhance wetting and hence minimize the interfacial energy [16-18].

5.2.2 Experimental Work

In this work, the thin films of Zintl-phase material $SrAl_4$ were deposited on perovskite oxide $LaAlO_3$ (LAO) (100) substrates using molecular beam epitaxy (MBE) [19]. Al and Sr K-cells to generate required metal fluxes were controlled using K-cell temperature and calibrated using a quartz crystal microbalance. Thin film growth was controlled by adjusting chamber pressure, flux using shutters and substrate temperature at 400 ^{o}C and growth was constantly monitored in-situ using RHEED. $SrAl_4$ thin films were capped with a coating of ~4 nm amorphous Ge to prevent interaction of film with air. RHEED indicated three-dimensional growth for $SrAl_4$ and excellent crystal quality with sharp spots. XRD study revealed high crystalline quality pure [001] oriented film with c=11.21 Å. AFM analysis confirmed 3-D growth mode [19].

In this work, $SrAl_4$ thin-films deposited on LAO were studied using transmission electron microscopy to determine the crystalline quality of thin films, film orientation and film-substrate interface structure. Cross-sectional TEM samples were prepared using conventional mechanical polishing and dimple grinding followed by precision ion milling

at ~ 3.0 keV to achieve final thickness for electron transparency. The samples were studied using the JEOL JEM 4000EX electron microscope operated at 400 keV with C_s = 1.0 mm yielding structural resolution of ~ 1.7 Å and JEOL JEM-2010F electron microscope operated at 200 keV with C_s = 0.5 mm, yielding the structural resolution of ~1.9 Å. For TEM JEM 4000EX, the HRTEM images were obtained with imaging conditions as Scherzer defocus of -49 nm, spherical aberration coefficient of C_s= 1.0 mm, half-convergence angle of 0.6 mrad and defocus spread of 10 nm. For TEM JEM 2010F, the HRTEM images were obtained with imaging conditions as Scherzer defocus of -43 nm, spherical aberration coefficient of C_s= 0.5 mm, half-convergence angle of 0.8 mrad and defocus spread of 13 nm. All images were takes very close to the Scherzer defocus. HRTEM images and diffractograms obtained from experimental images were compared with simulated images and diffraction patterns to obtain thin film orientation. The simulations were made using the commercial image simulation program JEMS. Same imaging parameters were used in simulations [19].

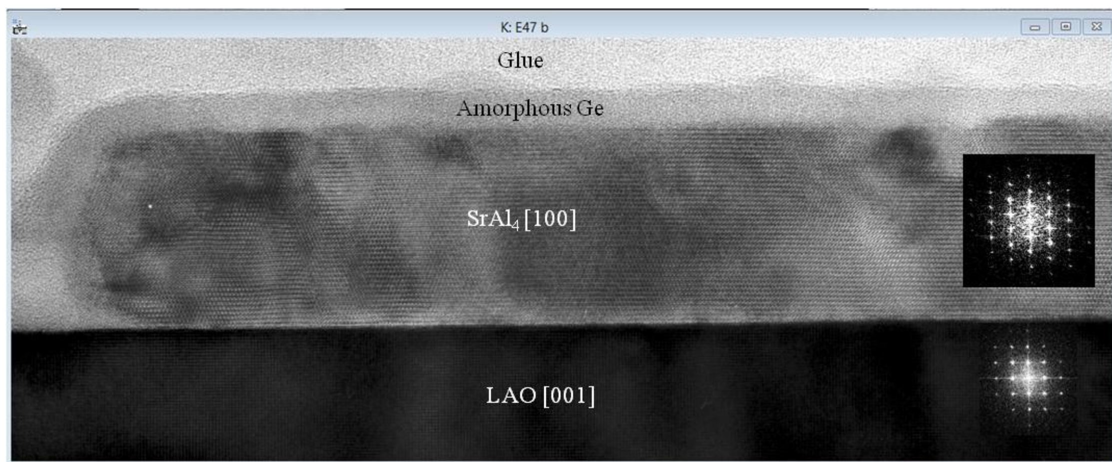

Figure 5.12 Cross-sectional HRTEM micrograph of $SrAl_4$/LAO. Diffractograms revealed projections of thin film and substrate. 3-D island growth is clearly visible.

Figure 5.12 is a cross-sectional HRTEM micrograph of ~16 nm $SrAl_4$ deposited on LAO (100) confirming 3-D island growth mode of $SrAl_4$ as suggested by AFM and RHEED. 3-D islands of ~0.2-0.3 µm were observed in cross-sectional TEM. The $SrAl_4$ island shows epitaxial registry with the substrate and a high degree of crystallinity. The 4-nm amorphous layer of Ge wraps nicely around the topology of the $SrAl_4$ island forming a protective coating. XRD showed (001) growth on $SrAl_4$ on (001) LAO. In the HRTEM cross-section, the diffractograms revealed projections [100] of $SrAl_4$ and [100] of LAO. Figure 5.13 is the same cross-section imaged using TEM JEM 2010F and a small section of this was used for interface analysis [19].

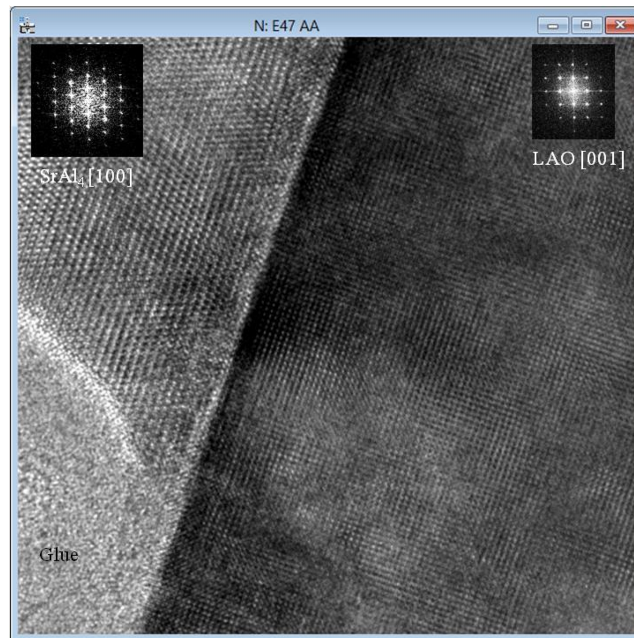

Figure 5.13 Cross-sectional HRTEM micrograph of $SrAl_4$/LAO. Diffractograms revealed projections of thin film and substrate.

The 3-D island growth of $SrAl_4$ is likely due to the nature of surface termination of LAO substrate. Since the surface termination of LAO is highly-temperature dependent, being exclusively AlO_2-terminated below ~ 150^oC and purely La-O terminated at

temperatures above 727°C [20]. Since growth temperature for $SrAl_4$ thin films was 400°C along with very brief annealing at 700°C, it is highly likely that LAO substrate actually has mixed terminations at growth temperature [20].

The DFT calculations of our collaborators at the University of Texas, Austin predicted that $SrAl_4$ thin films on AlO_2-terminated LAO are preferred energetically. Hence, the observed island growth mode probably arises from growth on a mixed termination LAO surface, with the $SrAl_4$ islands growing preferentially over patches of AlO_2-terminated LAO, as predicted by DFT calculations. Further theoretical work by our collaborators at the University of Texas, Austin revealed that the Sr-terminated $SrAl_4$ had the lowest energy as opposed to Al-terminated one. They also found that the measured valence band offset was in excellent agreement with the theoretical value for the model structure with the Sr layer at the interface [19].

5.2.3 Interface Structure Determination

Understanding the detailed atomistic structure and energetics of film/substrate interfaces in heteroepitaxial growth is of great importance Interface properties depend on the substrate termination plane. The exact termination plane of $SrAl_4$ (001) planes was difficult to determine solely from analysis of the HRTEM images in figures 5.12 and 5.13. Hence, $SrAl_4$/LAO HRTEM images were compared with HRTEM multislice simulations made using the commercial Image simulation program JEMS. HRTEM image used for this purpose is shown in figure 5.13. was obtained using TEM JEM 2010F, with imaging conditions as Scherzer defocus of -43 nm, spherical aberration

coefficient of C_s= 0.5 mm, half-convergence angle of 0.8 mrad and defocus spread of 13 nm. All images were taken close to the Scherzer defocus.

Considering theoretical studies as discussed in earlier section on LAO and $SrAl_4$ terminations, we considered two $SrAl_4$ (100)-LAO (001) interface models as shown in figure 5.14. The LAO substrate has energetically preferred AlO_2 termination in both models while the first layer of $SrAl_4$ facing LAO is Sr in model 1 and Al in model 2. The interface models were built using the commercial software Crystalmaker by editing individual crystals of $SrAl_4$ and LAO and then combining individual crystals to get the required interface model. The models were imported into the image simulation software program JEMS and HRTEM images were then simulated using the multislice module.

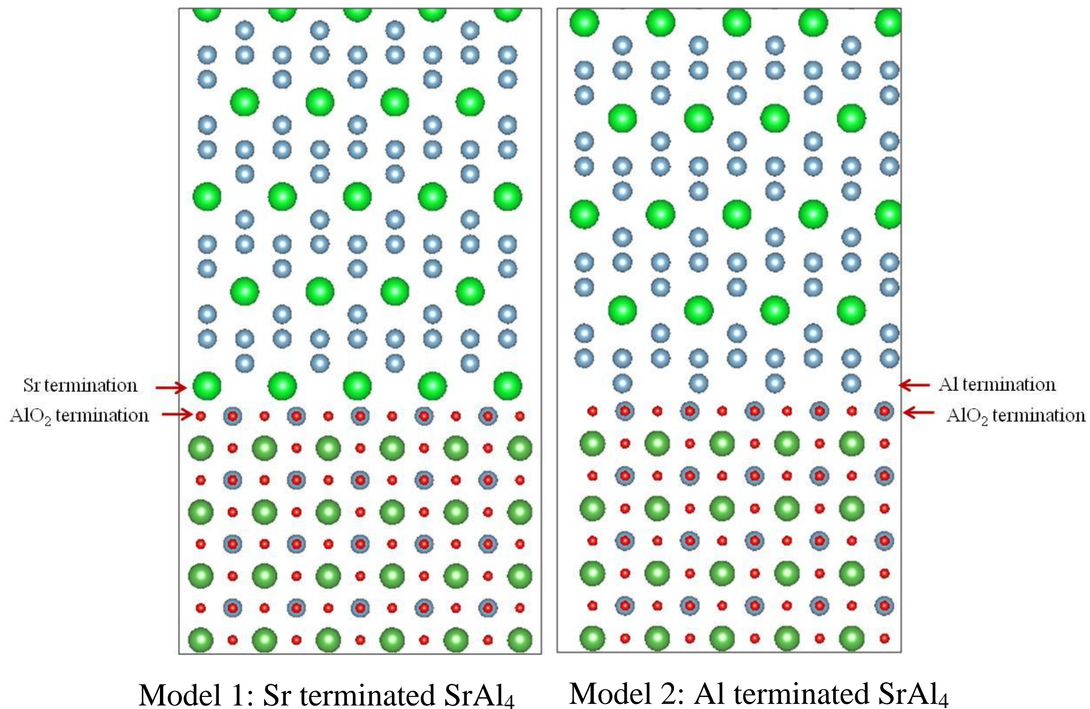

Figure 5.14 Model 1: Sr terminated SrAl4 (100) on AlO_2 terminated LAO (001) and model 2 of Al terminated SrAl4 (100) on AlO_2 terminated LAO. (001).

The imaging conditions chosen were identical to those used for observation with the JEOL JEM 2010F as mentioned above. Although the experimental images were obtained close to Scherzer defocus of -43 nm, the exact sample thickness and defocus values of the experimental images were not known. Hence, thickness-defocus series were calculated (not shown here) to create an array of images with different defocus and thickness values. Every image was then matched with the experimental image to identify the best match. Near Scherzer defocus, the bright spots in the simulated and experimental images represent the positions of oxygen and aluminum columns. The darker spots correspond to the positions of the Sr or La columns. Atom column view feature of JEMS makes it possible to see atom column positions along with simulated images. Matching interface model with experimental images is quite tedious (as compared to matching individual crystals at nearly same imaging condition). Imaging at various defocus away from the Scherzer defocus and increasing thickness adds dynamical effects to imaging. In this case simple assumption of having bright spots in HRTEM images at oxygen columns and dark spots at heavier elements no longer apply. Image simulation becomes necessary.

Figure 5.15 show simulated images of interface model 1 of Sr terminated $SrAl_4$ (100) on AlO_2 terminated LAO (001) and interface model 2 of Al terminated $SrAl_4$ (100) on AlO_2 terminated LAO (001) along with experimental image cross-section. From the experimental image it is clear that the very top AlO_2 layer of substrate LAO is slightly displaced. The charge rearrangement at the termination layer, especially in presence of highly electropositive Sr is expected. With coherent electron source of TEM 2010F, slight delocalization of image contrast especially near interfaces is expected.

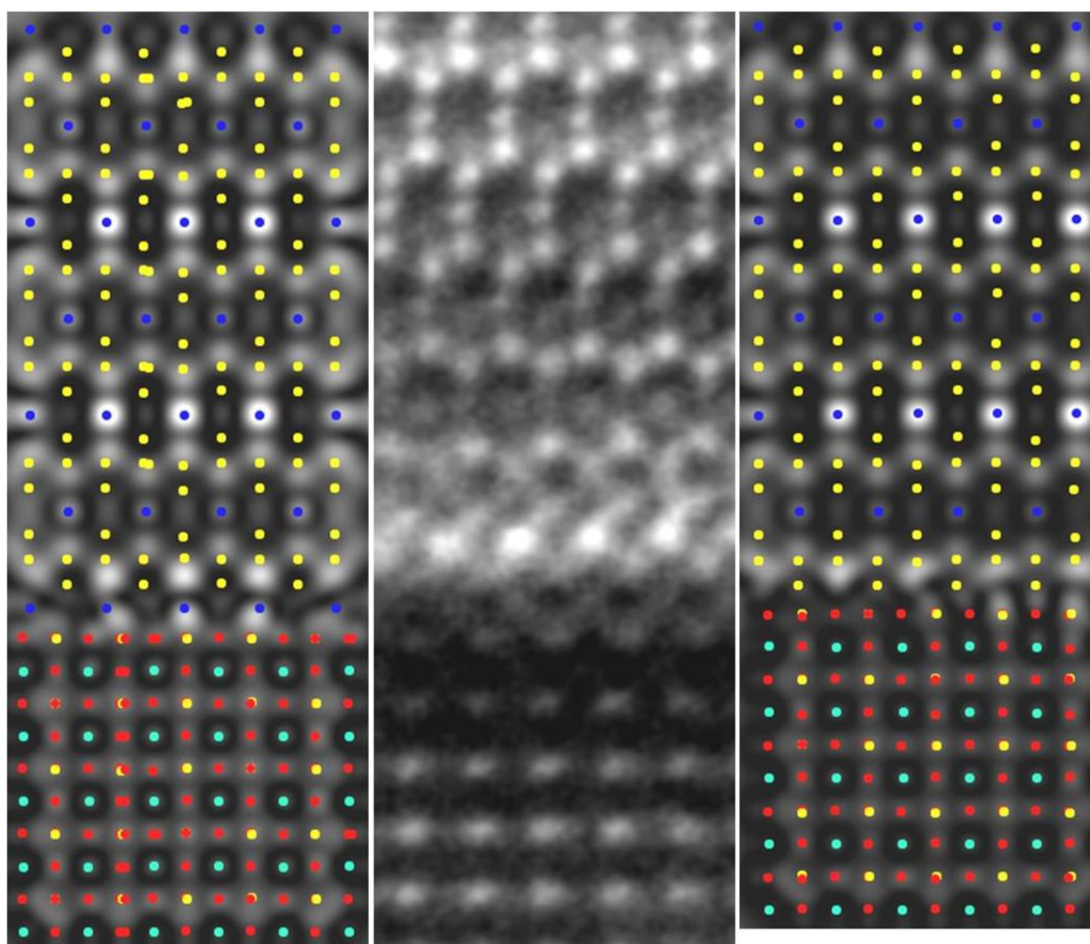

Figure 5.15 Simulated images of interface model 1 and interface model 2 along with atom columns compared with a cross-section of experimental image. The color code for atom columns: Red: O, Dark Blue: Sr, Yellow: Al, Green: La.

The essential difference between model 1 and model 2 is the interface layer of Sr. Interface model 1 clearly fits very well with the experimental image and model 1 is the preferred one. One layer of Sr atoms columns generated sufficient contrast in the simulated HRTEM images to differentiate it from the case without Sr column. Our results agree with the DFT calculations made by our collaborators at the University of Texas at Austin on the same two models. Hence, it is assumed that the Sr-terminated $SrAl_4$ (001) layer better satisfies the wetting condition for AlO_2-terminated LAO substrate (001).

Hence, with Sr termination of $SrAl_4$, the $SrAl_4$-LAO interface has lower energy. Figure 5.16 is a experimental image embedded with model 1 sums up this work.

5.3 Conclusions

HRTEM study of NbO_x films grown on STO(111) and LSAT(111) showed the formation of high quality NbO_2 films with highly coherent interfaces. Comparison of the experimental electron diffraction pattern with simulated diffraction pattern, the lattice parameter of NbO_2 was determined and found to be ~13.8 Å. These value is in good agreement with the value of a= 13.71 Å measured using Neutron Diffraction experiments for BCT NbO_2. For the NbO_x/LSAT heterostructure, the NbO_x phase was found to be of the cubic rocksalt (Pm-3m) structure type. Comparing the experimental diffraction pattern with simulated diffraction pattern, the lattice parameter of NbO was determined to be $a \approx 4.26$ Å, which was in good agreement with the value of a= 4.25Å reported in the literature. Using HRTEM image and multislice image simulations, possible models for the NbO_2/STO and NbO/LSAT interfaces were proposed.

$SrAl_4$ deposited on LAO (001) confirmed the 3-D island growth mode of $SrAl_4$ on LAO, with the $SrAl_4$ islands growing preferentially over patches of AlO_2-terminated LAO. The $SrAl_4$ islands shows epitaxial registry with the substrate and a high degree of crystallinity. Assuming AlO_2 termination for LAO substrate, the exact termination plane of $SrAl_4$ (001) planes was determined by comparing HRTEM images for $SrAl_4$/LAO heterostructure with HRTEM multislice simulations. The model with Sr-terminated $SrAl_4$ (001) layer fitted better with the experimental HRTEM images. Hence, it was deduced that the $SrAl_4$ (001)-LAO (100) interface has lower energy with Sr termination of $SrAl_4$.

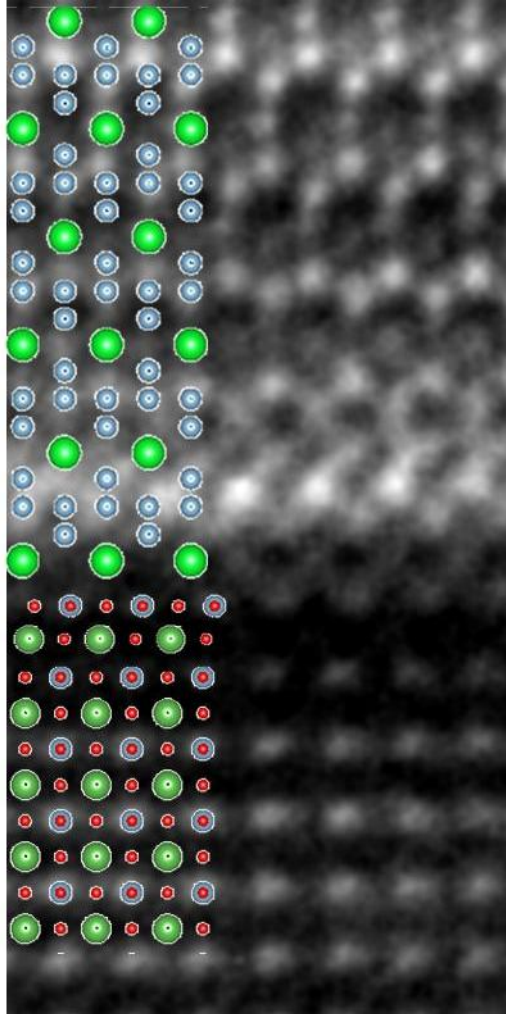

Figure 5.16 Experimental HRTEM cross-section embedded with interface model 1.

References

1. A. B. Posadas, A. O'Hara, S. Rangan, R. A. Bartynski, and A. A. Demkov, Applied Physics Letters (2014) 104, 092901.

2. V. Eyert, Europhysics Letters (2002) 58, No. 6, 851.

3. A. O'Hara, T. N. Nunley, A. B. Posadas, S. Zollner, and A. A. Demkov, Journal of Applied Physics (2014) 116, 213705.

4. F. J. Wong and S. Ramanathan, J. Mater. Res., (2013) Vol. 28, No. 18, 2555-2563.

5. F. J. Wong and S. Ramanathan, Journal of Vacuum Science & Technology, (2014) A 32, 040801.

6. Y. Zhao, Z. Zhang and Y. Lin, J. Phys. D: Appl. Phys., (2004) 37, 3392–3395.

7. A. Cheetham and C. N. R. Rao, Acta Cryst. B (1976) 32, 1579.

8. A. Bolzan, C. Fu, B. Kennedy, and C. Howard, J. Solid State Chem., (1994) 113, 9-14.

9. J. R. Gannon and R. J. D. Tilley, J. Solid State Chem., (1977) 20, 331-344.

10. R. Huang, H. Hayashi, F. Oba, and I. Tanakaa, Journal of Applied Physics, (2007) 101, 063526.

11. R. Tao, R. Todorovic, J. Liu, R. J. Meyer, A. Arnold, W. Walkosz, P. Zapol, A. Romanenko, L. D. Cooley, and R. F. Klie, Journal of Applied Physics (2011) 110, 124313.

12. J. H. Westbrook and R. L. Fleischer, Intermetallic Compounds-Principles and Practice: Progress, John Wiley and Sons, Volume 3, Aug 2002.

13. S. Gobel, M. Somer, W. Carrillo-Cabrera, E. M. Peters, K. Peters, and H. G. von Schnering, Z. Kristallogr. 211, 189 (1996).

14. J. Snyder and E. S. Toberer, Nat. Mater. 7, 105 (2008).

15. J. Cava, H. Ji, M. K. Fuccillo, Q. D. Gibson, and Y. S. Hor, J. Mater. Chem. C, 2013, 1, 3176-3189.

16. A. A. Demkov, H. Seo, X. Zhang, and J. Ramdani, Appl. Phys. Lett. 100, 71602 (2012).

17. R. A. McKee, F. J. Walker, and M. F. Chisholm, Phys. Rev. Lett. 81, 3014 (1998).

18. H. Seo, M. Choi, A. B. Posadas, R. C. Hatch, and A. A. Demkov, Journal of Vacuum Science & Technology B 31, 04D107 (2013).

19. L. Schlipf, A. Slepko, A. B. Posadas, H. Seinige, A. Dhamdhere, M. Tsoi, D. J. Smith, and A. A. Demkov, Physical Review B 88, 045314 (2013).

20. J. P. Jacobs, M. A. San Miguel, and L. J. Alvarez, J. Mol. Struct. 390, 193 (1997).

CHAPTER 6

SUMMARY AND FUTURE WORK

6.1 Summary

Metal oxides exhibit a broad spectrum of electronic, optical, and magnetic properties, such as ferroelectricity, ferromagnetism, and superconductivity, primarily due to the mixed ionic and covalent nature of the bonding and the strong electron correlations of *d* and *f* orbital electrons. Creating thin films of multifunctional oxides in thin-film form provides additional parameters, such as strain, finite thickness, and electric tunability, for controlling and manipulating the various interactions that produce the oxide collective phenomena, especially at the oxide-oxide interfaces. The esoteric physical properties of oxide thin films originate from the microstructure, chemical composition, electronic structure, and interface structure. High quality oxide thin films and multilayers can be grown using MBE and ALD deposition techniques, in which atomic-level layer-by-layer control is possible. The integration of oxide thin films with silicon is a major technological advance since multifunctionalities of oxides are combined with existing mature semiconductor technology. Transmission electron microscopy is a very powerful technique to explore oxide thin-film structure at sub-nanometer resolution.

The perovskite $SrTiO_3$ (STO) is a highly promising material for technological applications in the microelectronics industry because of its high charge-storage capacity, good insulating properties with high dielectric constant, excellent optical transparency in the visible region with a wide band gap of ~3.2 eV, and excellent chemical stability. The

physical properties of STO, for example, its conductivity, can be effectively modified by changing the oxygen partial pressure or by acceptor/donor doping at the cation positions. When a foreign cation/dopant is introduced into the STO lattice, a distortion from cubic to some lower symmetry will occur. Distortions to the STO lattice are assigned to three main effects, namely size effects, deviations from ideal composition, and crystal-field effects, also known as the Jahn-Teller effects.

One serious limitation of STO is the absence of a conduction-band offset between Si and STO, making STO unsuitable for use as a gate dielectric. It is possible to modify the band structure of STO by systematically doping the Ti with different dopants. For example, an Al dopant effectively substitutes Ti and creates associated oxygen vacancies, and its main effect on the electronic structure is to block Ti-Ti hopping, which reduces the conduction band width and therefore increases the band gap by 0.3 eV. The HRTEM and HAADF images presented in this thesis show the excellent crystallinity of the Al-doped STO throughout the thin films, even at the 20% doping levels. The EDX and EELS elemental mapping show that the Al profiles, in general, roughly follow the desired doping distribution. The relative Ti/O ratio, shows an increase of Al doping levels that corresponds to a decrease in Ti % and a rise in O vacancies to reach charge neutrality.

EELS spectra provide very useful chemical and electronic information based on the O-K and Ti-L core-edge structure. The shape of the EELS O-K and Ti-L edges, which reflects the underlying electronic structure, changed as function of Al substitution. The Crystal field in STO was measured using ELNES and it was found that the Crystal-field strength decreased by ~1.0 eV as Ti^{4+} was substituted by Al^{3+}. The decreased

Crystal-field strength suggested decreased crystalline symmetry owing to changed bond-angles and bond-lengths. Shift of Ti-L towards lower energy and slight rise in the L_3/L_2 ratio as a function of Al substitution confirmed the increased oxygen vacancy levels. The damping of peaks in the O-K ELNES data confirmed the rise in oxygen vacancies. Doping Ti^{4+} with Al^{3+} created associated oxygen vacancies that possibly blocked the Ti-Ti hopping conduction mechanism, and could be a possible method for the enlarged band gap of Al-doped STO.

Cobalt-substituted STO films grown on Si were found to be good single crystal quality. EDS and EELS line scans across the samples revealed that the Co doping was quite random. By substituting Ti^{4+} with Co^{3+} or Co^{2+} created associated oxygen vacancies for charge balance. The presence of oxygen vacancies was confirmed by the shift of Ti-L_2 and Ti-L_3 peaks towards lower energy by ~0.4 eV. Crystal field in Co-doped STO was measured directly using ELNES and it was found that the Crystal-field strength decreased by ~0.6 eV as Ti^{4+} was substituted by Co^{3+} or Co^{2+}. The decreased Crystal-field strength suggested loss of crystalline symmetry. L_3/L_2 ratio was observed to be same as undoped STO. These results suggests that Co^{3+} or Co^{2+} partially substituting Ti with some finite possibility of Co-O vacancy complexes substituting for Sr or occupying interstitial sites. This also explains high resistivity and ferromagnetism in Co-doped STO.

Complex cobalt oxides find applications in gas-sensing, spintronics, batteries, and in catalysis, particularly for oxidation of carbon monoxide. The HRTEM micrographs of as-grown (110)-oriented Co_3O_4 films grown on $MgAl_2O_4$ substrates show films of high crystallinity and the formation of an atomically flat and coherent interface between Co_3O_4

and $MgAl_2O_4$. The detailed atomistic structure of film/substrate interfaces in heteroepitaxial growth is very important since the interface properties depend on the termination plane of the substrate. The exact termination plane within the (110) planes of the substrate $MgAl_2O_4$ was difficult to determine solely from analysis of the HRTEM images, so $Co_3O_4/MgAl_2O_4$ images were analyzed using simulations. A comparison of experimental and simulated line profiles along atomic columns across the interface for both models, revealed that model B with only Al and O atoms in the termination layer of substrate $MgAl_2O_4$ was the better fit, correspondingly Co_3O_4 thin film were grown on the Al-O-terminated $MgAl_2O_4$ substrate. These results agreed with the theoretical results which predict that the AlO-terminated $MgAl_2O_4$ has lower interface energy.

The long-range strain fields associated with defects in spinels are of considerable importance since these strain fields affect the cation distribution. The defects can directly affect the magnetic properties, and the interaction of defects with charge carriers can occur far from defect cores thus also affecting transport properties. Geometric phase analysis (GPA) of HRTEM images was employed to find displacement fields associated with distortions in lattice fringes. The corresponding strain fields can then be found by analyzing the derivative of the displacement field. GPA analysis of the $Co_3O_4/MgAl_2O_4$ heterostructure revealed that strain fields are present around the stacking faults. The strain fields changed in magnitude over very small length scales revealing the possibility of the presence of charge, which in spinels corresponds to the absence of electro-neutrality near or at the dislocations. This presence of charges quite localized near the strain fields could be due to an imbalance of Co^{+2} and Co^{+3} and corresponding associated

movement of oxygen vacancies. The GPA analysis shows that the strain components E_{xx} and E_{yy} change from negative to positive and *vice-versa* in short length scales. Since it is well known that the dislocation cores are the source of strain inversion, the strain inversion could be related to charge segregation and /or oxygen deficiency.

The MIT in NbO_2 is associated with a structural transformation from a true tetragonal Rutile structure into a distorted Rutile body-centered tetragonal (BCT) structure below 1081 K. The MIT can be effectively used in electronic devices if materials are made in thin film form. HRTEM study of NbO_x films grown on STO (111) and LSAT (111) show the formation of high quality NbO_2 films with coherent interfaces. By comparing the experimental electron diffraction pattern with the simulated diffraction pattern, the lattice parameter of NbO_2 was determined and found to be ~13.8 Å. These value is in good agreement with the value of a= 13.71 Å measured using Neutron Diffraction experiments for BCT NbO_2. For the NbO_x/LSAT heterostructure, the NbO_x phase was found to be of the cubic rocksalt (Pm-3m) structure type. Comparing the experimental diffraction pattern with simulated diffraction pattern, the lattice parameter of NbO was determined to be $a \approx 4.26$ Å, which was in good agreement with the value of a= 4.25Å reported in the literature. Using HRTEM images and image simulations, possible models for the NbO_2/STO and NbO/LSAT interfaces were proposed.

The presence of covalent and ionic bonding make Zintl phases such as $SrAl_4$ very interesting choices as intermediate layers between the interfaces of covalently bonded semiconductors and polar perovskite oxides. Zintl phases enhance wetting and hence minimize interfacial energy. $SrAl_4$ deposited on LAO (100) showed 3-D island growth

mode, with $SrAl_4$ islands growing most likely over patches of AlO_2-terminated LAO. The $SrAl_4$ island showed epitaxial registry with the substrate and a high degree of crystallinity. Assuming AlO_2 termination for the LAO substrate, the exact termination plane of $SrAl_4$ (001) planes was determined by comparing the HRTEM images of $SrAl_4$/LAO interface with the multislice image simulations. The structural model with an Sr-terminated $SrAl_4$ (001) layer fitted better with the experimental HRTEM images. Thus, we can deduce that the $SrAl_4$ (001)-LAO (100) interface has lower energy with the Sr termination of $SrAl_4$.

6.2 Remarks on Future Work

Our results on Al- and Co-doped STO provide further motivation for studying various doped-perovskites with different dopants and with variable doping levels. The effect of substitution on the Ti^{4+} has been clearly understood. However, many questions still remain such as the possibility of partial substitution at Sr^{2+} along with Ti^{4+} and, more importantly, the role of oxygen vacancies and the tendency for formation of cation-oxide complexes in perovskite materials. DFT calculations predict the idea of such complexes. Cation exchanges, diffusion and oxide vacancies play prime roles in exhibiting the exotic properties of oxide thin films and interfaces. A comprehensive study of various perovskites doped with various substitutions could yield a matrix of parameters affecting doping in perovskites. There is a possibility of better understanding or even novel phenomena that will enhance our knowledge of oxide physics. Aberration-corrected HRSTEM-EELS, HAADF and ABF imaging, and DFT calculations, could be a way to

get this matrix on perovskites. Furthermore, understanding about doped-perovskites could be applied to understanding doping mechanisms in other oxides phases.

Understanding the electrical, magnetic and optical properties of interfaces is a crucial step towards our destination of next generation of oxide-based electronics. We saw in earlier chapters that HRTEM imaging along with modeling-simulation yields a good understanding of various interfaces. Delocalization of contrast especially at the interfaces, which is an effect of finite Cs could be minimized by using aberration-corrected HRTEM with negative C_s. The aberration- corrected HRTEM along with DFT calculations could be the best way to move forward with the modeling-simulation approach. DFT results input into models and then output of modeling-simulation results becomes input for further DFT calculations with improved models, forming a feedback mechanism with multiple iterations. These calculations could then be compared with HRTEM images. This would be the best way for some oxide-oxide interfaces to determine substrate termination and interface structure at atomic resolution wherein beam-induced damage is visible as beam is being scanned on the sample in STEM mode.

Spinel-spinel interfaces are interesting possible candidates for realizing spin-polarized 2-D electron gas at the interface. Spinel materials show high propensity for cation vacancies and their migration which is associated with the presence of stacking faults and dislocations. Behavior of cation defects and associated oxygen deficiencies near the spinel-spinel interface are of great interest since this form of modulation doping at interfaces gives rise to charge accumulation. Dynamics of charge in strong polarizing fields decides the presence or absence of charge carrier gas. Study of combinations of

normal and inverse spinel thin films-substrates grown using MBE could give comprehensive understanding about the possible presence of 2-D electron/hole gas. TEM techniques including HRSTEM-EELS, HAADF, and BF imaging along with DFT calculations would be very useful in understanding spinel interfaces in detail.

The metal-to-insulator transitions (MIT) in tetragonal NbO_2 and VO_2 could be the future technology of choice for next generation of electronic devices and sensors. Achieving electrically-controlled MIT in actual devices require oxides in thin film media form. The nonisostructural film-substrate combinations offer vastly more options and functionalities. Strain can be an additional parameter in controlling MIT as well as acting as control variable to bring down (or move up) MIT towards room temperature. HRTEM, HRSTEM-EELS along with DFT calculations can play a crucial role in analysis of different combinations of tetragonal thin films/substrates and understanding physical and chemical structure of the interface. The oxidation state of these oxides is crucial as physical properties dramatically change with change in oxidation state. Detailed analysis of near-edge EELS peaks structure would reveal information about oxidation state, and the effect of strain on oxidation state can be studied.

COMPREHENSIVE LIST OF REFERENCES

1. J. Mannhart and D. G. Schlom, Science 327, 1607 (2010).

2. J. M. Rondinelli and N. A. Spaldin, Adv. Mater. 2011, 23, 3363–3381

3. C. H. Ahn, K. M. Rabe, J.-M. Triscone, Science 303, 488 (2004).

4. L.W. Martin, Y.-H. Chu , R. Ramesh, Materials Science and Engineering R 68 (2010) 89–133.

5. S. Stemmer and S. J. Allen, Annu. Rev. Mater. Res. 2014. 44:151–71.

6. J. Mannhart, D.H.A. Blank, H.Y. Hwang, A.J. Millis, and J.-M. Triscone, MRS Bulletin, Volume 33, November 2008, 1027-1034.

7. H. Y.Hwang, MRS Bulletin, Volume 31, January 2006, 28-35.

8. H. Y. Hwang, Y. Iwasa, M. Kawasaki, B. Keimer, N. Nagaos and Y. Tokura, Nature Materials, Vol. 11, FEB. 2012, 103-113.

9. F. M. Granozio , G. Koster , and G. Rijnders , MRS Bulletin, Volume 38, December 2013, 1017-1023.

10. L Bjaalie1, B Himmetoglu, L Weston, A Janotti and C G Van de Walle, New Journal of Physics 16 (2014) 025005.

11. Koida, M. Lippmaa, T. Fukumura, K. Itaka, Y. Matsumoto,M. Kawasaki, and H. Koinuma, Phys. Rev. B, 66 [14] 144418 (2002).

12. Yamada, M. Kawasaki, T. Lottermoser, T. Arima, and Y. Tokura, Appl. Phys. Lett., 89 [5] 052506 (2006).

13. Bhattacharya, X. Zhai, M. Warusawithana, J. N. Eckstein, and S. D. Bader, Appl. Phys. Lett., 90 [22] 222503 (2007).

14. J. May, A. B. Shah, S. G. E. te Velthuis, M. R. Fitzsimmons, J. M. Zuo, X. Zhai, J. N. Eckstein, S. D. Bader, and A. Bhattacharya, Phys. Rev. B, 77 [17] 174409 (2008).

15. Bhattacharya, S. J. May, S. G. E. te Velthuis, M. Warusawithana, X. Zhai, B. Jiang, J.-M. Zuo, M. R. Fitzsimmons, S. D. Bader, and J. N. Eckstein, Phys. Rev. Lett., 100 [25] 257203 (2008).

16. Ohtomo and H. Y. Hwang, Nature, 427 [6973] 423–6 (2004).

17. Brinkman,M. Huijben,M. vanZalk, J. Huijben,U. Zeitler, J.C.Maan,W.G. van der Wiel, G.Rijnders, D. H. A. Blank, andH. Hilgenkamp, Nat. Mater., 6 [7] 493–6 (2007).

18. Reyren, S. Thiel, A. D. Caviglia, L. Fitting Kourkoutis, G. Hammerl, C. Richter, C. W. Schneider, T. Kopp, A.-S. Ruetschi, D. Jaccard, M. Gabay, D. A. Muller, J.-M. Triscone, and J. Mannhart, Science, 317 [5842] 1196–9 (2007).

19. S. N. Ruddlesden and P. Popper, Acta Cryst., 11 [1] 54–5 (1958).

20. G. Rijnders, Nature Materials Vol. 13, 844-845 (2014).

21. J. H. Lee, G. Luo, I. C. Tung, S. H. Chang, Z. Luo, M. Malshe, M. Gadre, A. Bhattacharya, S. M. Nakhmanson, J. A. Eastman, H. Hong, J. Jellinek, D. Morgan, D. D. Fong and J. W. Freeland, Nature Materials 13, 879–883 (2014).

22. A. A. Demkov and A. B. Posadas, Integration of Functional Oxides with Semiconductors, Springer 2014.

23. D. G. Schlom, L. Q. Chen, X. Pan, A. Schmehl, and M. A. Zurbuchen, J. Amer. Ceram. Soc., 91; [8] 2429–2454 (2008).

24. R. Ramesh, K. Luther, B. Wilkens, D. L. Hart, E. Wang, J. M. Tarascon, A. Inam, X. D. Wu, and T. Venkatesan, Appl. Phys. Lett., 57 [15] 1505–7 (1990).

25. B. Chrisey, and G. K. Hubler (ed), Pulsed Laser Deposition of Thin Films. Wiley, New York, 1994.

26. D. G. Schlom, J. N. Eckstein, E. S. Hellman, S. K. Streiffer, J. S. Harris Jr., M. R. Beasley, J. C. Bravman, T. H. Geballe, C. Webb, K. E. von Dessonneck, and F. Turner, Appl. Phys. Lett 53 [17] 1660–2 (1988).

27. J. Eckstein and I. Bozovic, Annu. Rev. Mater. Sci., 25, 679–709 (1995).

28. M. de Keijser and G. J. M. Dormans, MRS Bull., 21 [6] 37–43 (1996).

29. A.C. Jones, M. Hitchman (eds.), Chemical Vapor Deposition: Precursors, Processes and Applications (RSC Publishing, Cambridge, 2009) Chap. 4.

30. S. B. S. Heil, J. L. van Hemmen, M. C. M. van de Sanden, and W. M. M. Kessels, J. Appl. Phys., 103, 103302 (2008)

31. R. Ramesh and D. G. Schlom, Science, 296 [5575] 1975–6 (2002).

32. J. M. Phillips, J. Appl. Phys., 79 [4] 1829–48 (1996).

33. A. G. Schrott, J. A. Misewich, M. Copel, D. W. Abraham, and Y. Zhang, Appl. Phys. Lett., 79 [12] 1786–8 (2001).

34. J. Lettieri, J. H. Haeni, and D. G. Schlom, J. Vac. Sci. Technol. A, 20 [4] 1332–40 (2002).

35. S. Matsubara, T. Sakuma, S. Yamamichi, H. Yamaguchi, and Y. Miyasaka, pp. 243–53 in Ferroelectric Thin Films, Materials Research Society Proceedings, Vol. 200, Materials Research Society, Pittsburgh, PA, 1990.

36. M. Suzuki, J. Ceram. Soc. Jpn. Int. Ed., 103 [11] 1088–99 (1995).

37. K. J. Hubbard and D. G. Schlom, J. Mater. Res., 11 [11] 2757–76 (1996).

38. D. G. Schlom, L. Q. Chen, C. B. Eom, K.M. Rabe, S. K. Streiffer, and J.-M. Triscone, Annu. Rev.Mater. Res., 37, 589–626 (2007).

39. T. R. Taylor, P. J. Hansen, B. Acikel, N. Pervez, R. A. York, S. K. Streiffer, and J. S. Speck, Appl. Phys. Lett., 80 [11] 1978–80 (2002).

40. M.-W. Chu, I. Szafraniak, R. Scholz, C. Harnagea, D. Hesse, M. Alexe, and U. Gosele, Nat. Mater., 3 [2] 87–90 (2004).

41. S. P. Alpay, I. B. Misirlioglu, V. Nagarajan, and R. Ramesh, Appl. Phys. Lett., 85 [11] 2044–6 (2004).

42. V. Nagarajan, C. L. Jia, H. Kohlstedt, R. Waser, I. B. Misirlioglu, S. P. Alpay, and R. Ramesh, Appl. Phys. Lett., 86 [19] 192910 (2005).

43. A. Vasudevarao, A. Kumar, L. Tian, J. H. Haeni, Y. L. Li, C.-J. Eklund, Q. X. Jia, R. Uecker, P. Reiche, K. M. Rabe, L. Q. Chen, D. G. Schlom, and V. Gopalan, Phys. Rev. Lett., 97 [25] 257602 (2006).

44. R. J. Cava, Science, 247 [4943] 656–62 (1990).

45. A. K. Gutakovskii, L. I. Fedina, and A. L. Aseev, Phys. Status Solidi A, 150 [1] 127–40 (1995).

46. S. M. Nakhmanson, K. M. Rabe, and D. Vanderbilt, Phys. Rev. B, 73 [6] 060101 (2006).

47. L. Kim, D. Jung, J. Kim, J. S. Kim, and J. Lee, Appl. Phys. Lett., 82 [13] 2118–20 (2003).

48. Y. L. Li, S. Y. Hu, D. Tenne, A. Soukiassian, D. G. Schlom, L. Q. Chen, X. X. Xi, K. J. Choi, C. B. Eom, A. Saxena, T. Lookman, and Q. X. Jia, Appl. Phys. Lett., 91 [25] 252904 (2007).

49. A. Soukiassian, W. Tian, V. Vaithyanathan, J. H. Haeni, L. Q. Chen, X. X. Xi, D. G. Schlom, D. A. Tenne, H. P. Sun, X. Q. Pan, K. J. Choi, C. B. Eom, Y. L. Li, Q. X. Jia, C. Constantin, R. M. Feenstra, M. Bernhagen, P. Reiche, and R. Uecker, J. Mater. Res., 23 [5] 1417–1432 (2008).

50. A. A. Demkov, P. Ponath, K. Fredrickson, A. B. Posadas, M. D. McDaniel, T. Q. Ngo, and J. G. Ekerdt, Microelectronic Engineering Volume 147 (2015) 285-289.

51. Schlom, D., L. Q. Chen, C. Fennie, V. Gopalan, D. Muller, X. Q. Pan, R. Ramesh, R. Uecker. MRS Bulletin (2014) 39 118-130.

52. C. Ederer and N. A. Spaldin, Phys. Rev. Lett., 95 [25] 257601 (2005).

53. D. W. Williams & C. B. Carter, Transmission Electron Microscopy. New York: Springer(1996).

54. A. I Kirkland and J. L Hutchison, Nanocharacterisation, RSC Publishing 2007, Chapter 1, 1-27.

55. D. J Smith, Rep. Prog. Phys. 60 (1997) 1513–1580.

56. D.J. Smith, Adv. Opt. Electron Microsc., 1988, 11, 1.

57. M.A. O’Keefe, Ultramicroscopy, 1992, 47, 282.

58. W. Coene, G. Janssen, M. Op de Beeck and D. van Dyck, Phys. Rev. Lett., 1992, 69, 3743.

59. A. Thust and K. Urban, Ultramicroscopy, 1992, 45, 23.

60. D. J. Smith, Ultramicroscopy 108 (2008) 159–166.

61. M.A. O’Keefe, U. Dahmen and C.J.D. Hetherington, Mater. Res. Soc. Symp. Proc., 1990, 159, 453.

62. J. M. Cowley, Diffraction Physics, Elsevier Science B.V., Amsterdam, 1995.

63. E. Kirkland, Advanced Computing in Electron Microscopy, Second Edition, Springer 2010.

64. S. Thoma and H. Cerva, Ultramicroscopy 38 (1991) 265-289.

65. R. W. Glaisher and A. E. C. Spargo, Ultramicroscopy 27 (1989) 131-150.

66. L. Reimer, Transmission Electron Microscopy, Springer 4th Edition, (1997).

67. J. M. Cowley and A. F. Moodie, Acta. Cryst. (1957) 10, 609–619.

68. P. Goodman and A. F. Moodie, Acta. Cryst. A (1974) 30, 280–290.

69. K. Ishizuka and N. Uyeda, Acta Cryst. A33 (1977) 740-748.

70. D. Knauss and W. Mader, Ultramicroscopy 37 (1991) 247-262.

71. P.A. Stadelmann, Ultramicroscopy, 1987, 21, 131.

72. M. Hytch, F. Snoeck, and R. Kilaas, Ultramicroscopy 74 (1998) 131-146.

73. F. Hue, M. Hytch, H. Bender, F. Houdellier, and A. Claverie, Phys. Rev. Lett. 100, 156602 (2008).

74. C.T. Koch, V.B. Ozdol and P.A. van Aken, Appl. Phys. Lett. 96 (2010) 091901.

75. V. B. Ozdol, D. Tyutyunnikov, P. A. van Aken and C. T. Koch, Cryst. Res. Technol. 49 (2014) 38-42

76. M.J. Hytch, F. Houdellier, Microelectronic Engineering 84 (2007) 460–463.

77. E.M. James, N.D. Browning, Ultramicroscopy 78 (1999) 125-139.

78. P. D. Nellist and S. J. Pennycook, Advances in Imaging and Electron Physics, Vol 113 (2000) 147-202.

79. D. O. Klenov and S. Stemmer, Ultramicroscopy 106 (2006) 889–901.

80. S. J. Pennycook, M. Varela, A. R. Lupini, M. P. Oxley and M. F. Chisholm, J. Electron Microsc 58(3): 87–97 (2009).

81. S. J. Pennycook and C. Colliex, MRS Bulletin, Vol. 37, JAN 2012, 13-18.

82. W. Sigle, Annu. Rev. Mater. Res., (2005) 35, 239-314.

83. J.C. Bravman and R. Sinclair, J. Electron. Microsc. Technol. (1984) 1, 53.

84. S.B. Newcomb, C.B. Boothroyd and W.M. Stobbs, J. Microsc. (1985) 140, 195.

85. L. A. Giannuzzi, and F.A. Stevie, Micron (1999) 30, 197.

86. H. Y.Hwang, MRS Bulletin, Vol 31 (2006) 28-35.

87. D. G. Schlom and J. Mannhart, Nature Materials, 10 (2011) 168-169.

88. W. Luo, W. Duan, S. G. Louie and M. L. Cohen, Physical Review B, 70 214109 (2004).

89. Y.L. Zhu, X.L. Ma, D.X. Li, H.B. Lu, Z.H. Chen, G.Z. Yang, Acta Materialia, Vol. 53, Issue 5, March 2005, Pages 1277–1284.

90. S.Y. Dai, H.B. Lu, F. Chen, Z.H. Chen, Z.Y. Ren, D.H. Ng, Appl Phys Lett, 80 (2002), 3545-3548.

91. H. Guo, L. Liu, Y. Fei, W. Xiang, H. Lu, S. Dai, Y. Zhou and Z. Chen, J. Appl. Phys. 94, 4558 (2003).

92. A. Leitner, C.T. Rogers, J.C. Price, D.A. Rudman, D.R. Herman, Appl Phys Lett, 72 (1998), 3065-3069.

93. Wakiya, N., Kimura, Y., Sakamoto, N., Fu, DS, Hara, T., Ishiguro, T., Kiguchi, T., Shinozaki, K., Suzuki, H., JOURNAL OF THE CERAMIC SOCIETY OF JAPAN, Volume: 117 Issue: 1369 Pages: 1004-1008.

94. Muenstermann, R., Menke, T., Dittmann, R ., Waser, R., Advanced Materials, Volume: 22 Issue: 43 Pages: 4819-4824.

95. Phan, B.T., Choi, T., Lee, J ., Integrated Ferroelectrics, Volume: 96 Pages: 146-152.

96. Kawasaki, S., Nakatsuji, K., Yoshinobu, J., Komori, F., Takahashi, R., Lippmaa, M., Mase, K., Kudo, A., Applied Physics Letters, Volume: 101 Issue: 3, 033910.

97. Huan-hua W., Da-fu C., Sou-yu D., Hui-bin L., Yue-liang Z., Zheng-hao C. and Guo-zhen Y. J. Appl. Phys. 90, (2001) 4664-4667.

98. A. B. Posadas, C. Lin, A. A. Demkov, S. Zollner, Applied Physics Letters, 103, 142906 (2013).

99. M. D. McDaniel, A. Posadas, T. Q. Ngo, A. Dhamdhere, D. J. Smith, A. A. Demkov, and J. G. Ekerdt, Journal of Vacuum Science & Technology B 30, 04E111 (2012).

100. R.F. Klie, I. Arslan, and N.D. Browning, Journal of Electron Spectroscopy and Related Phenomena 143 (2005) 105–115.

101. D. A. Muller, N. Nakagawa, A. Ohtomo, J. L. Grazu, H. Y. Hwang, Nature, Vol 430, 5 Aug. 2004, 657-661.

102. M. Varela, J. Gazquez, S. J. Pennycook, MRS Bulletin Vol. 37 (2012) 29-35.

103. Z. Zhang, W. Sigle, and M. Ruhle, Physical Review B 66, 094108 (2002).

104. Z. Zhang, W. Sigle, and W. Kurtz, Physical Review B 69, 144103 (2004).

105. W. G. Waddington, P. Rez, I. P. Grant, C. J. Humphreys, Physical Review B, Vol. 34, (3) 1986, 1467-1474.

106. S. A. Wolf, D. D. Awschalom, R. A. Buhrman, J. M. Daughton, S. von Molnar, M. L. Roukes, A. Y. Chtchelkanova, and D. M. Treger, Science 294, 1488 (2001).

107. G. Schmidt, D. Ferrand, L. W. Molenkamp, A. T. Filip, and B. J. van Wees, Phys. Rev. B 62, R4790 (2000).

108. A. H. MacDonald, P. Schiffer, and N. Samarth, Nature Materials 4, 195 (2005).

109. Y. Matsumoto, M. Murakami, T. Shono, T. Hasegawa, T. Fukumura, M. Kawasaki, P. Ahmet, T. Chikyow, S. Koshihara, and H. Koinuma, Science 291, 854 (2001).

110. C. Song, K. W. Geng, F. Zeng, X. B. Wang, Y. X. Shen, F. Pan, Y. N. Xie, T. Liu, H. T. Zhou, and Z. Fan, Phys. Rev. B 73, 024405 (2006).

111. S. B. Ogale, R. J. Choudhary, J. P. Buban, S. E. Lofland, S. R. Shinde, S. N. Kale, V. N. Kulkarni, J. Higgins, C. Lanci, J. R. Simpson et al., Phys. Rev. Lett. 91, 077205 (2003).

112. J. Philip, A. Punnoose, B. I. Kim, K. M. Reddy, S. Layne, J. O. Holmes, B. Satpati, P. R. Leclair, T. S. Santos, and J. Moodera, Nat. Mater. 5, 298 (2006).

113. R. A. McKee, F. J. Walker, and M. F. Chisholm, Phys. Rev. Lett. 81, 3014 (1998).

114. C. Pascanut, N. Dragoe, and P. Berthet, J. Magn. Magn. Mater. 305, 6 (2006).

115. S. X. Zhang, S. B. Ogale, D. C. Kundaliya, L. F. Fu, N. D. Browning, S. Dhar, W. Ramadan, J. S. Higgins, R. L. Greene et al., Appl. Phys. Lett. 89, 012501 (2006).

116. A. B. Posadas, C. Mitra, C. Lin, A. Dhamdhere, D. J. Smith, M. Tsoi, and A. A. Demkov, Physical Review B 87, 144422 (2013).

117. J. Q. He, C. L. Jia, V. Vaithnayathan, D. G. Schlom, J. Schubert, A. Gerber, H. H. Kohlstedt, and R. H. Wang, J. Appl. Phys. 97, 104921 (2005).

118. H. Yang, P. G. Kotula, Y. Sato, M. Chi, Y. Ikuhara and N. D. Browning, Mater. Res. Lett., 2014 Vol. 2, No. 1, 16–22.

119. H. St. C. O'Neill and A. Navrotasky, American Mineralogist, (1983) Volume 6, pp. 181-194.

120. K. E. Sickafus, J. M. Wills and N. W. Grimes, J. Am. Ceram. Soc., (1999) 82 [12] 3279–92.

121. S.T. Murphy, C.A. Gilbert, R. Smith, T.E. Mitchell, and R.W. Grimes, Philosophical Magazine, (2010) 90:10, 1297–1305.

122. S. C. Petitto and M. A. Langella, J. Vac. Sci. Tech. A 22 (4) Jul/Aug 2004, 1690-96.

123. K. J. Kormondy, A. B. Posadas, A. Slepko, A. Dhamdhere, D. J. Smith, K. N. Mitchell, T. I. Willett-Gies, S. Zollner, L. G. Marshall, J. Zhou, and A. A. Demkov, Journal of Applied Physics. (2014) 115, 243708.

124. C. A. F. Vaz, V. E. Henrich, C. H. Ahn, E. I. Altman, Journal of Crystal Growth (2009) 311, 2648–2654.

125. C. A. F. Vaz, H. Q. Wang, C. H. Ahn, V. E. Henrich, M. Z. Baykara, T. C. Schwendemann, N. Pilet, B. J. Albers, U. D. Schwarz, L. H. Zhang, Y. Zhu, J. Wang, E. I. Altman, Surface Science (2009) 603, 291–297.

126. H. Hayashi, R. Huang, F. Oba, T. Hirayama and I. Tanaka, J Mater Sci (2011) 46: 4169–4175.

127. M. H. Lewis, Philosophical Magazine, (1968) 17:147, 481-499.

128. M. Hytch, F. Snoeck, and R. Kilaas, Ultramicroscopy 74 (1998) 131-146.

129. J. Hornstra, J. Phys. Chem. Solids, (1960) 15, 311-323.

130. C. B. Carter, Z. Elgat and T. M. Shaw, Philosophical Magazine, (1987) 55 (1) 1-19.

131. C. Gatel, B. Warot-Fonrose, S. Matzen, and J. B. Moussy, Applied Physics Letters, (2013) 103, 092405.

132. N. Li, S. Schäfer, R. Datta, T. Mewes, T. M. Klein, and A. Gupta, Applied Physics Letters, (2012) 101, 132409.

133. C. J. Zollner, T. I.Willett-Gies, S. Zollner, S. Choi, Thin Solid Films 571 (2014) 689–694.

134. T. Muschik and M. Ruhle, Philosophical Magazine, (1992) 65 (2) 363-388.

135. H. Sieber, P. Werner & D. Hesse, Philosophical Magazine A, (1997) 75 (4) 909-924.

136. F. Ernst, P. Pirouz & A. H. Heuer, Philosophical Magazine A, (1991) 63 (2) 259-277.

137. S. Matzen, J. B. Moussy, R. Mattana, K. Bouzehouane, C. Deranlot, F. Petroff, J. C. Cezar, M.-A. Arrio, Ph. Sainctavit, C. Gatel, B. Warot-Fonrose, and Y. Zheng, Physical Review, (2011) B 83, 184402.

138. N. J. van der Laag, C. M. Fang, and G. de With, G. A. de Wijs, H. H. Brongersma, J. Am. Ceram. Soc., (2005) 88 (6) 1544–1548.

139. R. Schweinfest, S. Köstlmeier, F. Ernst, C. Elsäser, T. Wagner & M. W. Finnis, Philosophical Magazine A, (2001) 81 (4) 927-955.

140. H. Sieber , D. Hess & P. Werner, Philosophical Magazine A, (1997) 75 (4) 889-908.

141. C. Fang, S. C. Parker and G. de With, J. Amer. Ceram. Soc., (2000) 83 [8] 2082–84.

142. A. B. Posadas, A. O'Hara, S. Rangan, R. A. Bartynski, and A. A. Demkov, Applied Physics Letters (2014) 104, 092901.

143. V. Eyert, Europhysics Letters (2002) 58, No. 6, 851.

144. A. O'Hara, T. N. Nunley, A. B. Posadas, S. Zollner, and A. A. Demkov, Journal of Applied Physics (2014) 116, 213705.

145. F. J. Wong and S. Ramanathan, J. Mater. Res., (2013) Vol. 28, No. 18, 2555-2563.

146. F. J. Wong and S. Ramanathan, Journal of Vacuum Science & Technology, (2014) A 32, 040801.

147. Y. Zhao, Z. Zhang and Y. Lin, J. Phys. D: Appl. Phys., (2004) 37, 3392–3395.

148. A. Cheetham and C. N. R. Rao, Acta Cryst. B (1976) 32, 1579.
149. A. Bolzan, C. Fong, B. Kennedy, and C. Howard, J. Solid State Chem., (1994) 113, 9-14.

150. J. R. Gannon and R. J. D. Tilley, J. Solid State Chem., (1977) 20, 331-344.

151. R. Huang, H. Hayashi, F. Oba, and I. Tanakaa, Journal of Applied Physics, (2007) 101, 063526.

152. R. Tao, R. Todorovic, J. Liu, R. J. Meyer, A. Arnold, W. Walkosz, P. Zapol, A. Romanenko, L. D. Cooley, and R. F. Klie, Journal of Applied Physics (2011) 110, 124313.

153. J. H. Westbrook and R. L. Fleischer, Intermetallic Compounds-Principles and Practice: Progress, John Wiley and Sons, Volume 3, Aug 2002.

154. S. Gobel, M. Somer, W. Carrillo-Cabrera, E. M. Peters, K. Peters, and H. G. von Schnering, Z. Kristallogr. 211, 189 (1996).

155. J. Snyder and E. S. Toberer, Nat. Mater. 7, 105 (2008).

156. J. Cava, H. Ji, M. K. Fuccillo, Q. D. Gibson, and Y. S. Hor, J. Mater. Chem. C, 2013, 1, 3176-3189.

157. A. A. Demkov, H. Seo, X. Zhang, and J. Ramdani, Appl. Phys. Lett. 100, 71602 (2012).

158. R. A. McKee, F. J. Walker, and M. F. Chisholm, Phys. Rev. Lett. 81, 3014 (1998).

159. H. Seo, M. Choi, A. B. Posadas, R. C. Hatch, and A. A. Demkov, Journal of Vacuum Science & Technology B 31, 04D107 (2013).

160. L. Schlipf, A. Slepko, A. B. Posadas, H. Seinige, A. Dhamdhere, M. Tsoi, D. J. Smith, and A. A. Demkov, Physical Review B 88, 045314 (2013).

161. J. P. Jacobs, M. A. San Miguel, and L. J. Alvarez, J. Mol. Struct. 390, 193 (1997).